OTTIMIZZAZIONE MULTIOBIETTIVO DI UNA SCHIERA PALARE DI UN COMPRESSORE TRANSONICO

Dipartimento di Ingegneria Industriale

Laurea Magistrale in Ingegneria Aerospaziale

Relatori:

Prof. Ernesto Benini, Università degli Studi di Padova

Prof. Tom Vertstraete, The Von Karman Institute for Fluid Dynamics

PhD candidate Mohamed Hassanine Aissa, The Von Karman Institute for Fluid Dynamics

Laureando:

Francesco Comin

Università degli Studi di Padova
Dicembre 2015

Dedicata alle mie nipoti,

Sofia e Giorgia

Nulla dies sine linea

(Plinio, Storia nat., 35)

Abstract

Questa tesi ha il duplice obiettivo di testare un processo automatico di ottimizzazione di una schiera palare di un compressore transonico, giustificando d'apprima i risultati ottenuti e dettando poi le linee guida per la riduzione delle perdite e quindi per il miglioramento delle prestazioni. In particolare, la simulazione prevede l'utilizzo di un software di ottimizzazione basato su un algoritmo DE, di un software per la creazione del campo di moto e della relativa mesh, e di un software per l'analisi CFD; questa combinazione consente di ottenere un processo completamente automatico che, partendo da una pala del tipo "precompressione blade" ne migliora le prestazioni in termini di riduzione delle perdite aerodinamiche. La pala così ottenuta mostra un configurazione delle onde d'urto all'interno e all'esterno del canale palare tipica di questa famiglia di profili, ma evidenziando una sostanziale riduzione delle perdite di circa il 20% rispetto alla configurazione di partenza. Inoltre, variando le condizioni iniziali del flusso e ottimizzando la pala per tre diversi angoli di ingresso, si possono dedurre l'angolo d'attacco e il numero di Mach ottimali che definiscono così le condizioni nominali della nuova geometria.

Contents

1 Introduction

In modern turbomachinery design, the requirements for increased efficiency and low losses led to use optimization techniques to gain further improvements in compressor and turbine performance. For this reason several optimization software were developed, matching different algorithms and configurations in order to reached the feasibility of the obtained designs. Furthermore, CFD and/or CSM softwares are required, to complete the optimization process with a further and more severe check of the feasible designs. In addition, flow field setup and meshing must be done carefully since, for an automated process, they are set only once, at the iteration beginning, and must fit in all the different designs. Finally, all the optimization scheme must be validated locally and globally, for ensuring a successful outcome.
As regards the cascade configuration and possible optimization parameter, the blade shape plays an important role in loss generation and a well-conditioned shock-loss model has to be established for each blade type. In particular, several supersonic airfoils were developed as such controlled diffusion airfoils and precompression blades, respectively DCA and ARL-2DPC 1 in figure 1. Modern compressor cascades use precompression blades since they allow to reach higher inlet Mach number and compression ratio at nominal condition (i.e. low loss condition); very thin leading edge and negative cambered pressure side at leading edge make the related shock and loss model different from the other blade shape flow pattern, reducing the total pressure loss and providing more safe and stable operations.

Figure 1: Several supersonic cascade blade shapes with their design Mach number [13]

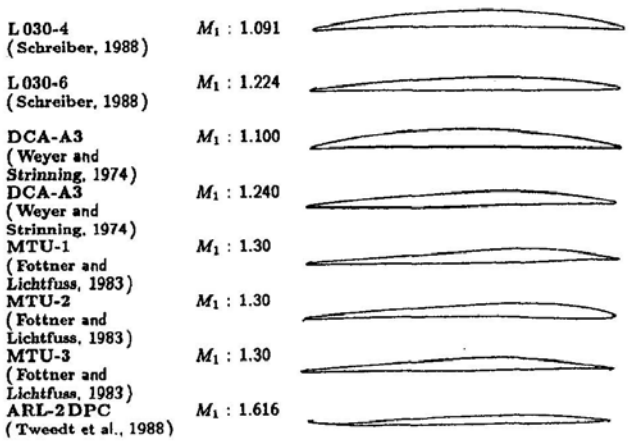

For these reasons, the optimization of a precompression blade becomes an interesting practice to test several softwares configurations as well as to develop a even more performant blade shape.

2 Compressors Performance Analysis

The evaluation of the performance of a turbomachinery is required in order to find the best setup of every part of the machine. For this purpose, we use pressure changes as performance evaluation and introduce an investigation about causes of this loss. Note that all below refers mainly to compressor, while, in some cases, extensions to turbines will be made.

2.1 General information

This brief description will report useful formulas in order to understand the aim and the subject of this work; for more details see [1],[9].
First the stagnation (i.e. total) pressure for perfect gas compressible flow is:

$$p_0 = p\Big(1 + \frac{k-1}{2}M^2\Big)^{\frac{\gamma}{k-1}} \tag{1}$$

where $k = c_p/c_v$ is the heat capacity ratio (considered constant and equal to 1.4) and p is the static pressure. Note that equation 1 is true only for calorically perfect gas and that p_0 value will be constant only during isentropic transformations, i.e. it will change through shocks or due to friction. Therefore its change could be used as loss quantifier.
Likewise, from equation 1 is possible to evaluate the isentropic Mach number at wall:

$$M_{iso} = \sqrt{\left(\left(\frac{p_0}{p}\right)^{\frac{k-1}{k}}\right)\frac{2}{k-1}} \tag{2}$$

where friction and in general boundary layer presence is neglected assuming not valid the no-slip condition at wall. Another fundamental equation for a fluidodynamics process of a perfect gas is the change in entropy; from the second law of thermodynamics, for an incremental isentropic process of a perfect gas, that increase is equal to $Tds = dQ = dh + v\,dp$ with $dh = c_p\,dT$ and $p\,v = RT$. Moreover, integrating between two known states, it is possible to find the following relation:

$$\Delta s = s_2 - s_1 = c_p\,\ln\left(\frac{T_2}{T_1}\right) - R\,\ln\left(\frac{p_2}{p_1}\right) \tag{3}$$

where s_1 is an entropy reference value, T_2, p_2, T_1 and p_1 could be both static or total temperature and pressure values and the subscript 1 refers to reference values. This latter conclusion comes from the nature of static to total condition transition, an isentropic process too. Note that entropy can not be measured directly and its absolute value is always arbitrary.
Consider the performance coefficients for a compressor stage or the entire machine. First thing to consider in *total isentropic efficiency* in equation 4 is the total isentropic enthalpy $h^0_{2\,is}$ on denominator: obviously this term does not allow to take into account irreversible phenomena and leads to overestimate η.

$$\eta_{iso} = \frac{h^0_{2\,is} - h^0_1}{h^0_2 - h^0_1} = \frac{\pi_c^{\frac{k-1}{k}} - 1}{\frac{T^0_2}{T^0_1} - 1} \qquad \text{with} \qquad \pi_c = \frac{p^0_2}{p^0_1} \quad \text{compression ratio} \tag{4}$$

Moreover, the coefficient just above depends on pressure ratio (i.e. total pressure); so, as the final pressure p_2 increases the η_{iso} decreases. For that reason the polytropic efficiency is preferred. It is the isentropic efficiency of an adiabatic thermodynamic process in which the pressure does not change and it can be seen as ratio between reversible and real work between initial and final state. Hence, considering a thermodynamic process in which the difference between initial and final pressure approaches zero, its performance can be evaluated as:

$$\eta_{pol} = \frac{dh_i s}{dh} = \frac{v\,dp}{c_p\,dT} = \frac{k-1}{k}\frac{\ln\left(\frac{p^0_2}{p^0_1}\right)}{\ln\left(\frac{T^0_2}{T^0_1}\right)} \tag{5}$$

At the end, for practical reasons[1], it is better to find a correlation between isentropic and polytropic efficiency:

$$\eta_{iso} = \frac{\left(\frac{p_2}{p_1}\right)^{\frac{(k-1)}{k}} - 1}{\left(\frac{p_2}{p_1}\right)^{\frac{(k-1)}{\eta_{pol}\,k}} - 1} \tag{6}$$

The equation 6 trend depicted in figure 2, shows how, at fixed polytropic value as pressure ratio increases, isentropic efficiency decreases; in particular, its drop is inversely proportional to η_{pol}. On the other hand, when the polytropic efficiency decreases, isentropic performance will be reduced. Moreover, as suggested in [2], this correlation make more clear the η_{iso} dependence to total pressure through the polytropic efficiency, as shown in equation 5, and the η_{pol} response to pressure change.

Figure 2: Isentropic-politropic efficiency correlation for compressors for k=1.4 [1]

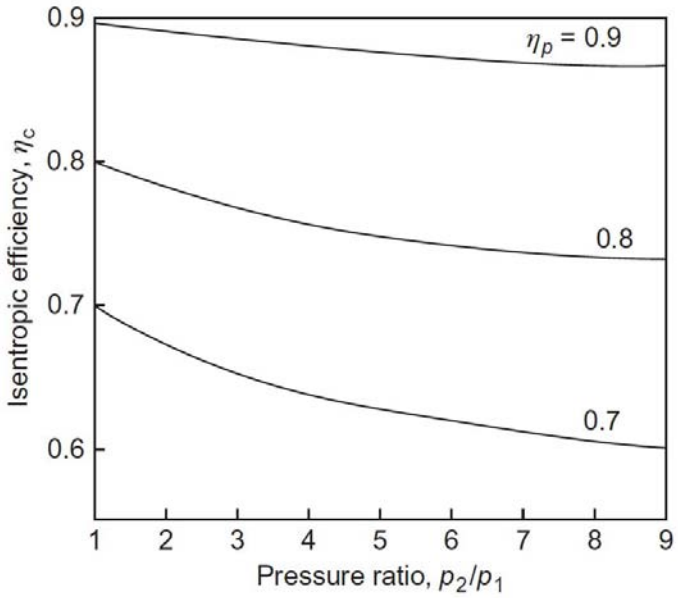

Considering only the total pressure change, another coefficient could be use, called *total pressure loss coefficient*[2]:

$$\omega = \frac{p_1^0 - p_2^0}{p_1^0 - p_1} \tag{7}$$

The latter one depicts the total pressure change trend through two known states. A more useful loss coefficient for compressors design purposes is the *energy* or *enthalpy loss coefficient*:

$$\zeta = \frac{h_2 - h_{2s}}{h_1^0 - h_1} \tag{8}$$

where h_{2s} is the isentropic final enthalpy value obtained in an isentropic compression again to state 2[3]. Note that, as reported in [15], this coefficient results independent from Mach number.
Later, in the next chapters, more details about efficiency coefficients and loss evaluation will be given. Finally, due to high speed flow (i.e. transonic) condition, only compressible case is taken into account.

[1] as mentioned above, the isentropic efficiency changes with pressure ratio and that behavior does not help the compressor design. Therefore, once fixed η_{pol}, equation 6 plot helps to choose the best compressor features in terms of losses reduction

[2] in literature some authors refers to it as Y, while others use the chosen ω symbol in order to better distinguish it from the mass-average coefficient in 22

[3] see figure 10

2.2 Geometry definition

First, consider one or more axial compressor stages, each made by a row of stator and a row of rotor blades (i.e. static and rotating blades), as depicted in picture 3. Then focus only on two stator blades, e.g. the ones inside the red box in figure. At this point, in order to leave the more complex 3D case and consider mainly 2D-dimensional flow, split the afore mentioned two blades in a plane: this is a *compressor cascade*, as shown in figure 4. The missing blades influence will be taken into account thanks to periodicity[4]. Note that, if the blades of a stage are experiencing great twist along their axis, 2D cascade analysis is not sufficient for accurate aerodynamics purposes.

Figure 3: 3D compressor stages.

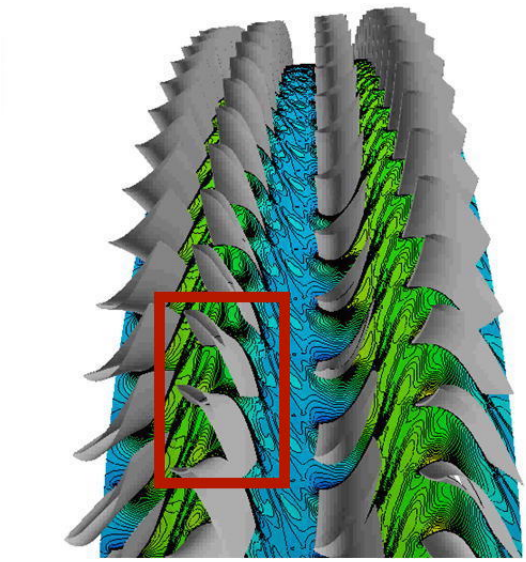

Figure 4: Focus on two blades of a compressor row.

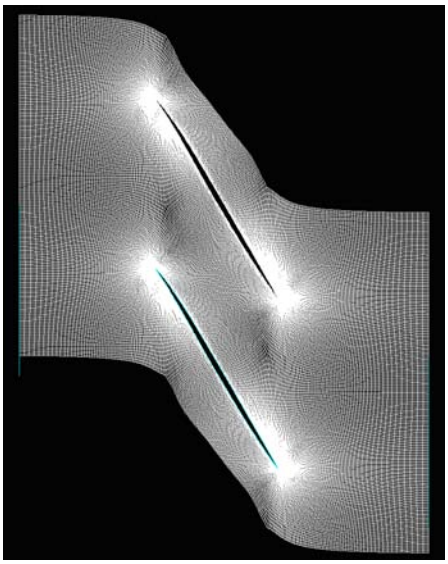

In particular, stator blade cascades become the core of the entire work, simplifying the analysis but introducing errors, omitting 3D losses and rotation influence. For these reasons in the following

Figure 5: Focus on two blades of a compressor row

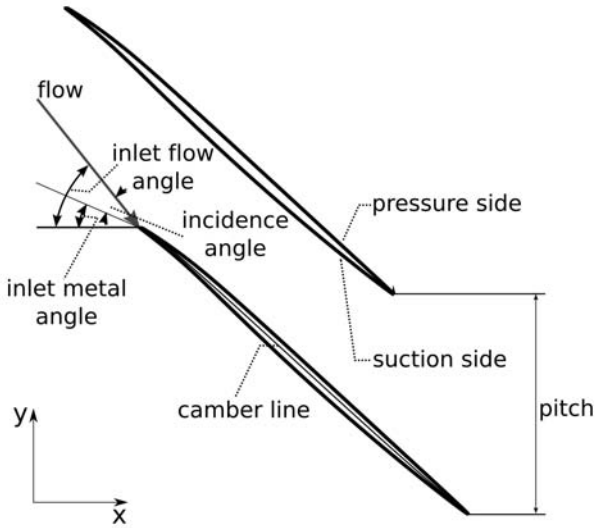

lines some hints to generic turbomachinery performance evaluation will be given. In figure 5 some important cascade components are shown: flow fields inlet and outlet, blade passage, blade pressure and suction side and inlet flow angle. The first one is affected by undisturbed flow conditions, while

[4] e.g. see flow behavior in picture 58

between the blades most of the fluidodynamics transformations take place. Obviously for periodicity, the flow exiting the domain in the upper side enters from the upper side.

Figure 6: 3D detail of a cascade blade with the shroud wall

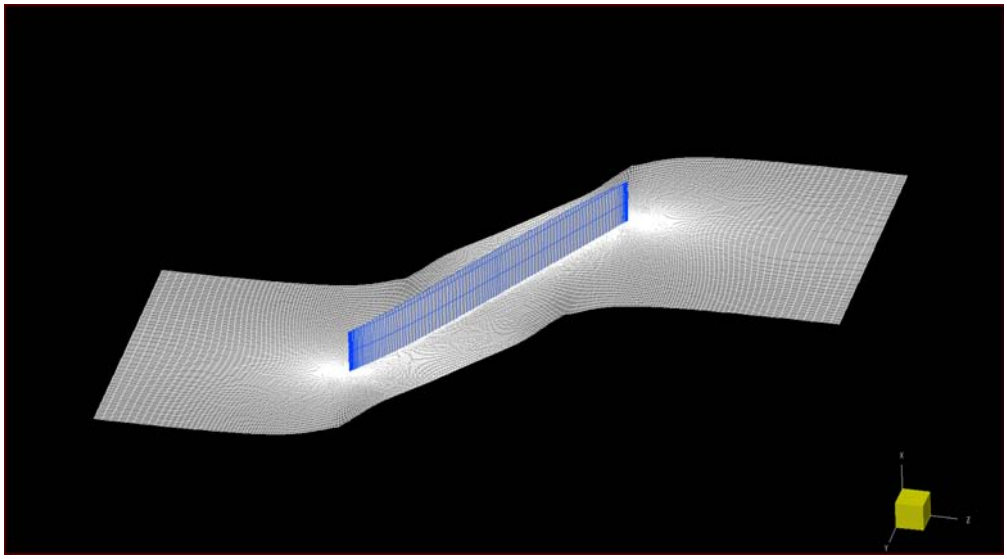

2.3 Losses evaluation

The term "loss" refers to any flow feature that reduces the efficiency of a turbomachinery, not showing how a single loss component affects the cycle efficiency. For these reasons an accurate classification of loss sources with the relative partition in single loss coefficient becomes useful and necessary. Unfortunately, in Aerodynamics the superposition principle is not completely valid, i.e. the sum of the effects do not coincide with the effect of the sum. So, despite evaluating the effects of each loss source introduces uncertainties and errors, this method is the only one possible for an accurate analysis of the performances of a turbomachinery. Therefore, consider the flow that passes through a compressors row, as shown in figures 5 and 4. However, it is possible to identify six different loss coefficients bound to six different sources:

a) *boundary layer loss*: it can be seen as the work lost due to viscous shear within the boundary layer; its magnitude depends on boundary layer development, on surface pressure distribution and on laminar-to-turbolent transition position. Moreover the flow acceleration can increase or decrease that term, making the boundary layer thicker or preventing separation

b) *trailing edge mixing loss* simply arises from the mixing of the suction surface and pressure surface boundary layers with the part of the flow just behind the trailing edge

c) *flow separation loss*: the detached boundary layer losses are included in this coefficient, but, for well ed blades, the flow should remain attached so its value will be neglected

d) *shock waves loss* occurs when the blade passage is choked and the inlet Mach number is above 0.9[5]. In general, in the passage between two blades, oblique shocks are preferred to normal one[6]; for this reason specific devices are used, as *precompression blade* or controlled diffusion airfoils

e) *secondary* or *end wall loss* is due to compressor hub and case annulus boundary layers growth[7] that increases the axial velocity distribution in a nonuniform way (see figure 7,13 [8]. Hence, the

[5] for a compressor, while in turbine $M_{outlet} \geq 0.9$

[6] normal shocks are stronger than the oblique one, losing more energy and leading to boundary layer separation. More details in chapter 3.2 and in [9]

[7] for a turbine, these boundary are thinner because of the less adverse pressure gradient they are exposed to

[8] note that, over the central region of the blade, in each stage, the axial velocity is higher than the mean value based on the through-flow

vorticity within the annulus boundary layer will be split at blade stagnation point, resulting in an highly rotational fluid on the suction surface near the hub and the casing endwalls. That behavior create a complex and extensive 3D flow field, called also *endwall flow*, which causes losses through viscous shear, mixing with the mainstream flow in the blade passage and through interaction with the boundary layers on the blade surface. Figure 8 shows the intricate flow structure.

Figure 7: Axial velocity profiles in a compressors [1]

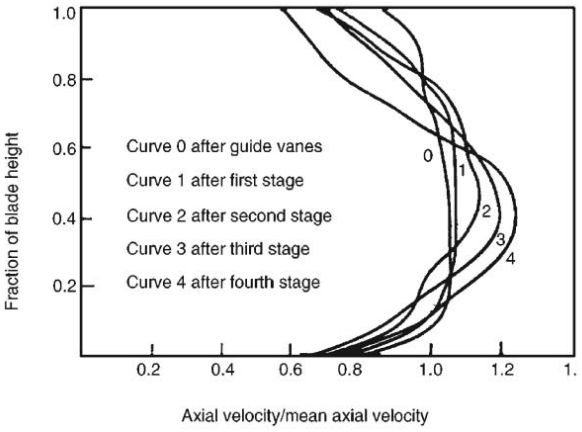

Figure 8: Secondary flow structure in a blade passage [1]

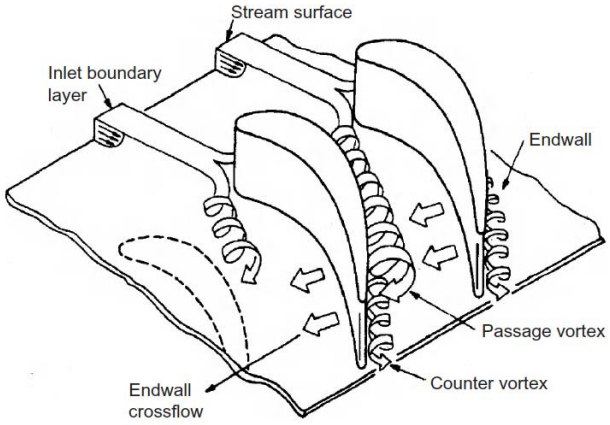

f) *tip leakage loss*: the flow through the clearance gap above the tip of a compressor rotor blades interacts with the end wall flow and the flow in the passage, creating new losses through mixing and shear[9], as depicted in figure 9. Moreover, it can cause a flow blockage, reducing the compressor stage overall flow capacity and decreasing the stable operating margin. That above said can be extend to stator blade and any gaps or seals, where in the first case the clearance gap is found at stator hub.

Figure 9: Tip leakage flow [1]

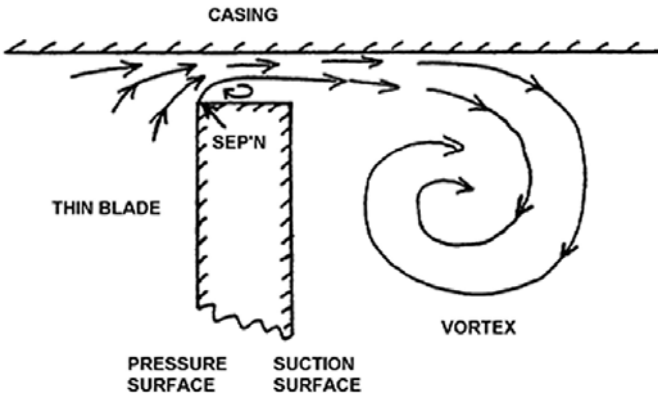

Note that the last and second last are 3D components, while the remaining are simply bi-dimensional.

2.3.1 Entropy coefficient

Considering the various loss coefficient formulations in equations $3 \div 8$, the entropy change Δs results immediately more interesting than the other ones. Indeed, in many cases, the flow is closely adiabatic, so only entropy creation by irreversibilities contributes significantly to the loss increase. In addition, any irreversible flow process creates entropy reducing at the same time the isentropic efficiency (see equation 4); therefore it is more accurate to evaluate the entropy production coefficients of each

[9] for these reasons sometimes it could be consider inside the secondary loss coefficient

blade row and summing them up to find the whole machine entropy increase. Moreover, entropy formulation does not change if the evaluated point is on a rotating or stationary blade, while total pressure and the relative total enthalpy could vary as a result of radius change. Finally, if another thermodynamic property of the flow at the outlet is known, the whole machine efficiency could be found.

Figure 10: H-S diagram for cascade flow

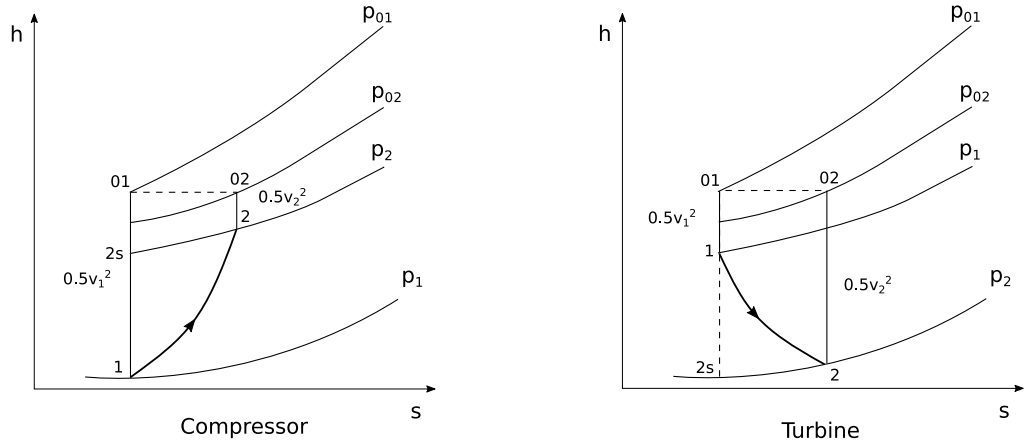

For the previous reasons the ΔS in equation 3 will be used in this work as an objective in the optimization of a compressor cascade. In particular, for adiabatic flow through a stationary blade row, the total temperature remains constant and so entropy changes depend only on stagnation pressure:

$$\Delta S = -R \ln\left(\frac{p_{02}}{p_{01}}\right) \tag{9}$$

For stator blades and cascade, where total pressure losses are directly bound to entropy increase and p_0 changes can be consider small, the equation 9 becomes:

$$\Delta S = -R \frac{\Delta p_0}{p_0} \tag{10}$$

Note that, sometimes, the total rate of entropy creation become more useful in the turbomachinery performance evaluation:

$$\dot{S} = m\,\dot{s} = -\int \frac{1}{T}\,\overline{\mathbf{V}} \cdot \overline{\mathbf{F}}_v\,dV \tag{11}$$

where $\overline{\mathbf{V}}$ is the local flow velocity vector, $\overline{\mathbf{F}}_v$ is the local viscous force per unit of volume and the integral is made over the volume. Moreover, as shown in figure 10, a relation between entropy change and isentropic efficiency exists:

$$\eta_{iso} \approx 1 - \frac{T_2(s_2 - s_1)}{h_2 - h_1} \tag{12}$$

where the approximation is possible only assuming the slope of h-s curve proportional to temperature, i.e. $\Delta S \propto \Delta h/T$ for constant values of loss coefficient. In other words, the static pressure is assumed constant along the line from 2 to $2s$ in figure 10. Note that, from the equation above, the loss efficiency is directly proportional to the specific entropy increase through the machine/cascade and also to its exit temperature. Moreover, since the overall[10] isentropic efficiency is proportional to the total entropy increase, an irreversible flow process at high temperatures creates lower loss of overall efficiency than does the same process at low temperature; this phenomena, called *reheat effect* and shown in the equation above, causes the polytropic efficiency to be different from the isentropic one; furthermore, in high pressure stages, the irreversibility effect on overall η_{iso} results less harmful than

[10] i.e. not local but referred to the entire machine/cascade

in low pressure stages. Finally, taking into account the whole machine, is possible to estimate the overall efficiency by summing stages entropy increases:

$$\frac{1-\eta_{overall}}{\eta_{overall}} = \frac{T_{exit}}{\Delta h_{overall}} \sum_{all\ stages} \frac{(1-\eta_{stage})\,\Delta h_{stage}}{\eta_{stage}\,T_{2stage}} \tag{13}$$

Now, at the end of this general discussion, more details will be given in order to evaluate the single loss sources contribution to overall entropy creation.

Boundary layer This loss is due to velocity change near walls, in particular its more severe in the inner part of the boundary layer where the velocity decrease more rapidly and the flow is not affected by the streamwise pressure gradient[11]. Considering a path along the blade in the x direction, the overall entropy change due to boundary layer from 0 to a specific point will be:

$$\dot{S} = \int_0^x \frac{\rho V_\delta^3 C_d}{T_\delta}\, dx \tag{14}$$

where V_δ is the velocity at the edge of the boundary layer, T_δ is the static temperature at the same point and C_d is the dissipation coefficient which trend depend on Reynolds number and flow turbulent/laminar behavior:

$$C_d = \begin{cases} 0.0056\, R_{e_\theta}^{-1/6} & \text{for turbolent b.l. with} \quad 10^3 < R_{e_\theta} < 10^5 \\ 0.002 & \text{for turbolent b.l. with} \quad R_{e_\theta} < 10^3 \\ \beta\, R_{e_\theta}^{-1} & \text{for laminar b.l.} \end{cases} \tag{15}$$

where R_{e_θ} is the Reynolds number based on momentum thickness, β is a constant which value depend on pressure gradient trend and, as suggested in [3], it could be chosen as 0.2 [12]. For completeness, it is possible to consider the stage overall increase in specific entropy due to the blade boundary layer; hence, evaluating the ΔS relative to the stage isentropic enthalpy change, the previous equation becomes:

$$\Delta S = \Delta h_{is}\, 2\, \frac{C_0}{V_x} \sum \frac{C_s}{p} \int_0^1 \frac{C_d}{T} \left(\frac{V_0}{C_0}\right)^3 d(x/C_s) \tag{16}$$

where $\Delta h_{is} = 0.5\, C_0^2$ is the stage isentropic enthalpy variation, C_0 defines the isentropic velocity bound to h_{is}, V_x is the speed along the x direction, V_0 is the blade surface velocity, the summation is over all the blade surfaces, C_s is the total length of the surface (i.e. pressure side or suction side), T_δ is the static temperature while the C_d is the dissipation coefficient in equation 15.
Moreover, as widely reported in [3], the minimum loss value in compressors case occurs when the boundary layer is separated, and, unlike in turbines, it becomes necessary to introduce a correction in the previous formulation in order to take into account the boundary layer separation and evaluate the right entropy increase. Focusing now on Mach number influence, its effects on entropy are generally considered small. Otherwise, a temperature increase near the blade plays a significant role, making necessary to use the surface temperature instead of T_δ. Also the blade surface roughness can affect the entropy creation, especially for high Reynolds number. Finally, considering 3D flow behavior too, results clear that surface streamline convergence-divergence may thicker the boundary layer; this does not affect the entropy unless a boundary layer separation occurs.

Trailing edge mixing In general, due to viscous shear, the mixing of two separate flows leads to entropy increase, i.e. losses generation. The flow processes here showed are extremely complex and often unsteady and the rate viscous dissipation is not confined in the boundary layer; for this reason it is seldom possible to evaluate local entropy variation, while the overall one can be found through

[11] as reported in [3], the 90% of the entropy growth occurs at $Y^+ < 250$ and the streamwise pressure gradient influence disappears at $Y^+ > 500$. More details about Y^+ will be found in section 5.3

[12] for an analytical and more general result, the Pohlhausen family of velocity profiles should be considered, with $\beta = (0.1746 + 0.0029\,\lambda + 0.000076\,\lambda^2)$ and λ as the Pohlhausen pressure gradient parameters which ranges from 12 for a highly accelerated boundary layer to -12 at separation. Since laminar boundary layer appears mostly on blades with favorable pressure gradients, i.e. $\lambda > 0$, the $\beta = 0.2$ assumption becomes realistic

the conservation of mass, energy and momentum applying a control volume analysis. The key feature, in the previous method, is the assumption that mixing will continue until the flow becomes uniform; this allow to evaluated the entropy increase without knowing where or how the mixing takes place. Considering two mixing flows, as

Figure 11: Mixing between an injected and mainstream flows

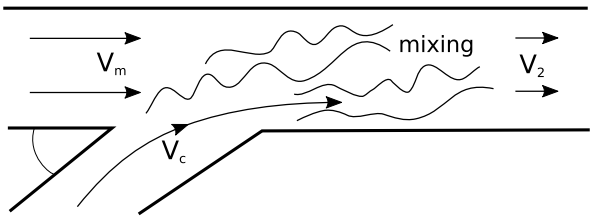

in figure 11, at the same total temperature and when one stream flow rate is small, the total entropy rate becomes:

$$\dot{S} = \begin{cases} T\, m_m\, \delta s = m_c \left(\frac{V_m^2 - V_m V_c\, cos\alpha}{T} \right) & \text{for costant area and pressure} \\ -(m_m + m_c)\, \frac{\Delta p_0}{p} = 0.5\, V_m^2\, m_c \left(\frac{2+3\,\frac{m_c}{m_m} + \left(\frac{m_c}{m_m}\right)^2}{T} \right) & \text{area and pressure dependant} \end{cases} \tag{17}$$

Note that the second expression in equation 17 refers to incompressible flows with the same stagnation temperature, same pressure and a relative angle of $\alpha = 90°$. Moreover, equation 17 again shows that most of the entropy creation takes place when $m_m/m_c = 5$ and within the injected flow, while the remaining mixing losses could be neglected.
What above mentioned could be deepen considering one of the most important turbomachinery mixing process, i.e. the mixing due to a wake behind the trailing edge. As explained in [3], the related entropy production coefficient could be split in three different part, respectively influence by:

- *base pressure coefficient* C_b, that shows the base pressure p_b trend on trailing edge and its difference with respect to the free stream pressure p_∞[13]. Its role in losses generation is ambivalent: it seems to cause dissipations in the wake but at the same time it could be seen as the results of wake dissipations
- *boundary layer momentum thickness* θ: it measures the entropy generated in the boundary layer upstream to the trailing edge and shows how the mixing losses are not due only to trailing edge thickness, i.e. to the relative p_b value[14]
- *boundary layer displacement thickness* δ^*: its influence in entropy generation becomes more important when boundary layer separates at trailing edge causing flow blockage, an harmful phenomenon that could lead to huge and fast loss increase.

Equation 18 show the correlation between the above mentioned terms:

$$\zeta = \frac{\Delta P_0}{0.5\, \rho\, V_{te}^2} = \frac{C_b\, t}{w} + \frac{2\,\theta}{w} + \left(\frac{\delta^* + t}{w} \right)^2 \tag{18}$$

with V_{te} the flow speed near trailing edge, w the passage width, ζ used as entropy generation indicator[15] and ΔP_0 the stagnation pressure difference between a reference value and the local pressure. This last term is streamwise-dependant:

$$\frac{d\, \Delta P_0}{dx} = \Delta P_0\, (1 - H)\, \frac{1}{V}\, \frac{dV}{dx} \tag{19}$$

[13] note that usually $p_b < p_\infty$, hence $C_b < 0$
[14] in a blade with zero trailing edge thickness, the entropy drop become independent from trailing edge p_b and its value depends on the difference between θ and δ_e
[15] this assumption is valid for incompressible flow only. Moreover, $\Delta S \propto \Delta h/T$

where x is the streamwise direction, H is the wake local shape factor (always greater than one) and V is the local speed. Hence, the pressure loss (i.e. the mixing loss) will increase with distance from the trailing edge and with flow deceleration. At the same time. as depicted in figure 12, wakes become wider with the increase of trailing edge and boundary layer mixing influence on the velocity profile (i.e. pressure). Therefore, in total pressure loss coefficient evaluation, the distance from trailing edge plays an important role allowing to consider wholly or partially the mixing losses.

Figure 12: Flow behaviour through a cascade [1]

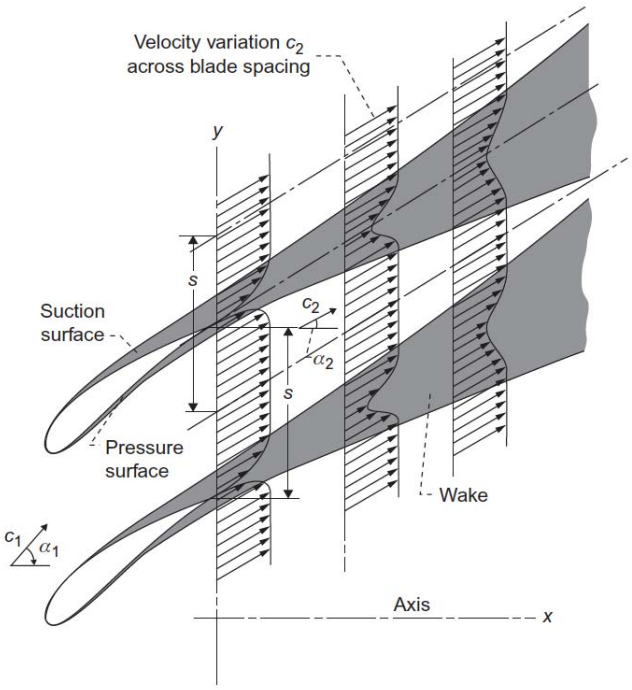

At this point is possible to note that in compressor blade the boundary layer is thicker and more often detached than in turbine, causing the δ^* to increase its importance in entropy generation, while the base pressure behavior loses its influence. Actually, in case of flow separation, a low pressure area appears within the separation, increasing the C_p value and obviously playing a much more severe role than expected in entropy generation (see figure 58). For this reason, despite its importance in compressors blade design[16], the trailing edge boundary layer separation influence is a major unknown in loss evaluation and base pressure prediction methods remain uncertain.

Shock waves In shock waves, heat conduction and high normal stresses are the main entropy creation reasons and its importance increases with mach number (so with pressure) and shock strength. Considering a plane normal or oblique shock, the pressure rise through it leads to entropy increase, as reported immediately below:

$$\Delta S \approx R\,\frac{k+1}{12\,k^2}\left(\frac{\Delta p}{p_1}\right)^3 + O\left(\frac{\Delta p}{p_1}\right)^4 \tag{20}$$

where R and k are constant related to perfect gas theory, p_1 is the static pressure just before the shock and Δp depicts its increase through the front. It is clear that, as the shock becomes weaker[17], the ΔS decrease in a non linear way and, following the approximation suggested in [3], it drops as a power of three. In order to better evaluate the total losses in a compressor row, the conservation of mass, energy and momentum between the cascade inlet and outlet flow could be used, in addiction

[16] indeed, as suggested in [3], trailing edge losses could be a big part of the total losses, until about 21%

[17] as explained in chapter 3.2, a weaker shock results in a less compressed flow, with a less relevant decrease in velocity with respect to a stronger shock. These purposes can be achieved splitting the process into two or more shocks or changing from normal to oblique front, maintaining the flow partially supersonic (more details in chapters ,)

to a control volume in the blade passage. This method allows to predict the overall changes with no needing to consider the detail of the flow inside the control volume. For this reasons, only losses due to leading edge shock will be taken into account, while the shock wave-boundary layer interaction effects needs extra notice. Indeed, at the shock foot, a boundary layer separation bubble will occur, causing more dissipation; if the shock waves is strong, this may lead to a complete separation, as usually happened when passage inlet Mach number is more than $M_1 = 1.4$. Thus, in transonic compressors, reducing M_1 through blade thinning and suction side reverse camber helps to decrease the shock wave entropy creation also splitting the pressure rise between two weaker shock.

Endwall loss "Endwall loss" terms all the losses arising on the annulus walls, within and outside the blade passage. Here, the flow patterns are bound to the thickness of the upstream boundary layer and to the turning in the blade row. Hence, for compressors, where the turning is less and the boundary layer is thicker, endwall loss becomes more difficult to discern from boundary layer loss and tip clearance loss. At the same time, due to boundary layer deceleration and its related vorticity[18], the endwall flow play a much more severe role in ΔS increasing than in turbines. So, in order to have a rough idea about its magnitude, the entropy production rate could be found with the following:

$$\dot{S} = 0.25 \int_0^{C_x} \frac{C_d}{T} \frac{(V_s^4 - V_p^4)}{(V_s - V_p)} \rho \, w \, dx \tag{21}$$

where C_x is the surface length along the axial x direction, C_d is the dissipation coefficient shown in equation 15, V_s and V_p are the velocity respectively on suction and pressure side and w is the local suction-to-pressure surface gap. Another topic of compressors endwall loss is the interaction between the endwall boundary layer and the blade row and the resulting pressure changes: indeed, that drop takes place in a more limited area and in a faster way than in a conventional boundary layer, leading to a high diffusion area beside the suction surface endwall with the resulting separation and flow blockage. This behavior, as depict in figure 14, is called *corner separation*. This highly three-dimensional separation causes huge flow mixing in the passage and even far downstream, with the relative large increase in mixing losses. Finally, an important clarification must be made: entropy is not increase directly by endwall loss, but by its interaction with other loss sources.

Figure 13: Annulus boundary layer and blade interaction [1]

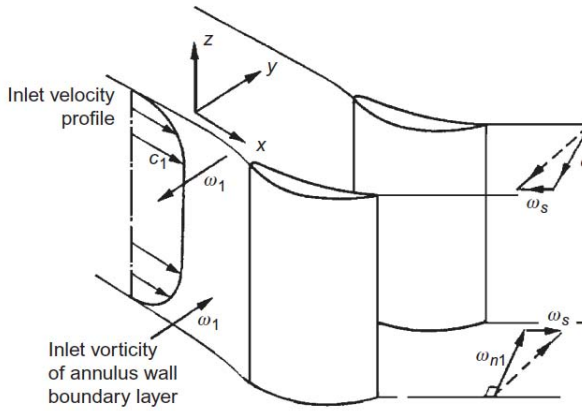

Figure 14: Pressure contours downstream of a stage [1]

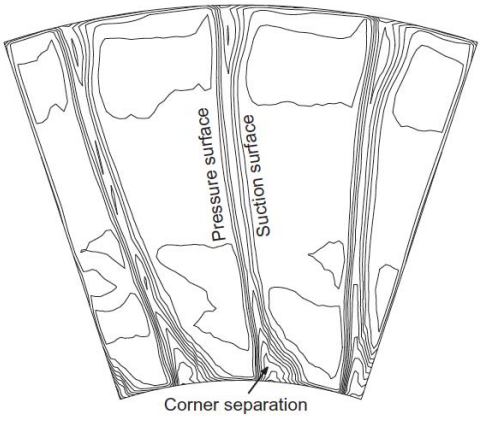

Tip clearance loss Clearance gaps in turbomachinery allow the so called *leakage flow* to pass from the blade pressure surface into the suction surface, driven by the pressure difference, as shown in picture 9. This flow usually separates from the pressure side corner of the blade tip through a separation bubble that reduces the passage area. If the blade thickness is small compared to the tip gap, the flow may not reattach, as it usually happens in compressors. In addition, the passing flow emerges as a high velocity jet at the suction surface tip, almost perpendicular to the free stream flow, generating a vortex with its rotation axis aligned to the streamwise direction. Therefore, tip

[18] see velocity profile and its effects in figures 13,8

clearance losses are mainly due to viscous shear in the gap as well as shear and mixing of the leakage flow with the free stream. Moreover, the induced blockage leads to total mass flow and work transfer reduction, that means a decrease in performance and, in compressors, a more serious reduction of the stable operating range.

Finally, some extra clarifications about losses evaluation will be reported:

- Boundary layer and mixing losses are strongly dependent on blade surface pressure distribution; for this reason pressure should be maintained as constant as possible, avoiding peaks or falls. Speed diffusion control over blade walls could help in this purpose
- Precompression blade aimed is to reduce shock wave losses through inlet speed decreasing, as better explained in chapter 3.4
- Shock and boundary layer losses are comparable in magnitude at inlet Mach number about 1.4 while at higher speed value the first one becomes dominant. This behavior is
- Despite what above said, when the diffusion level on the blade surface become too high, stall or surge could occur, hence flow separation losses must be taken into account. This scenario is typical at off-design condition
- Reminding to endwall losses, high velocity leakage flow could prevent corner separations reducing the entropy generated by secondary flow interaction. In addiction, blade skewness helps to drive the endwall fluid towards the blade pressure surface reducing the negative secondary flow effects
- Shrouds or reduced gaps help to prevent losses due to tip clearance. Obviously it is not possible to completely remove leakage flows, but a minimum value could be reached finding the optimum distance between blades and machine body
- Focusing on bi-dimensional compressor cascade analysis, three-dimensional losses are out of the scope of this work. Despite that, as reported in [3], 3D flows generate about 50% of the total losses and their interaction with other loss sources must be considered for a more accurate performance prediction

The analytical methods for entropy evaluation presented in this chapter are merely indicative but extremely representative of loss origin and its development in turbomachinery.

2.3.2 Total pressure loss coefficient

Another way to find losses influence in performance evaluation is to compare total pressure at cascade inlet and outlet. Total pressure decreases in irreversible process giving an idea about performances trend. Remembering the previous losses classification, blades boundary layers, flow separation and shock waves effects in a point in the flow could be evaluated using the equation in 7. Calculation points are usually chosen along a line normal to the flow field exit (as p_{02}), while reference value of both static and total pressure are collected in a point in the undisturbed flow before flow-blades interaction. In order to obtain an useful performance parameter, the previous ω will be integrated along the p_{02} "collecting line" averaging with density:

$$Y_p = \frac{\int_0^s \omega \, \rho c_x \, dy}{\int_0^s \rho c_x \, dy} \tag{22}$$

where c_x is the flow speed along the flow direction and s is the length of the line with the evaluation points. Therefore, after plotting the ω trend and its average value, from figure 15 is possible to distinguish the different loss sources: the peak near trailing edge position, at $y/s = 0.5$, is due to velocity and pressure change inside the wake[19] while, in presence of shock waves, other lower peaks would appears on right and left side of the major one, as in figure 67. Reminding the equation 22 evaluation method and figure 12, the integration should be done near the flow field exit and, when

[19] this wake is due to wall viscous effect and eventual flow separations; its width will increase with distance, as shown in figure 12

comparing different configuration performance, at the same x position. Note that, averaging along the whole flow field width with more than one blade lead ω trend to be periodic, as in picture 67.

Figure 15: Typical total presure loss coefficient trend and its average value [1]

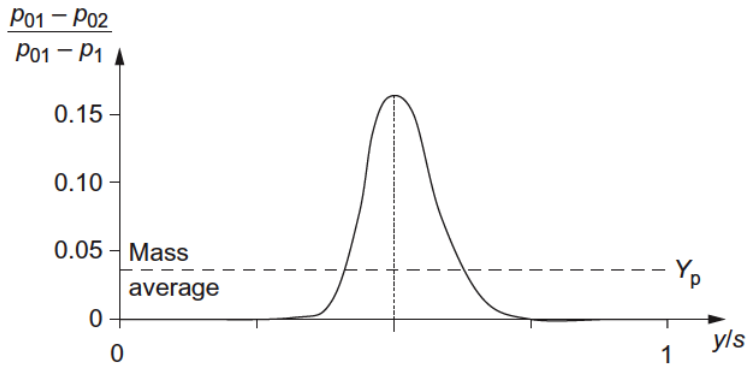

Finally, as above mentioned, Y_p evaluation needs to take into account rotational effect: in a stage, where both rotor and stator are carried, the pressure loss coefficient must be calculated apart for each component and then summed together.
Three-dimensional losses in compressor are not so easy to find using the mere total pressure change; for that aim ΔS should be used.
Despite all the drawbacks afore reported, the ω trend will become useful to have an immediate idea about blades shape role in losses generation (see chapter 6).

2.4 Stability analysis in compressor stages

The performance of a compressor blade change with inlet flow conditions. Therefore, a machine designed for a certain value of total pressure or flow angle could be less performant as inlet conditions changes. This behavior becomes more severe in multi-stage turbomachinery, where the performance of the i-th stage is bound to both the previous and following stages. Considering an incoming flow with a given total pressure and total temperature, the following relation will be found:

$$\frac{p_{02}}{p_{01}},\ \eta,\ \frac{\Delta T_0}{T_{01}} = f\left(\frac{\dot{m}\sqrt{T_{01}}}{p_{01}},\ \frac{\Omega}{\sqrt{T_{01}}}\right) \tag{23}$$

where $\Delta T = T_{02} - T_{01}$, $\dot{m}$ is the mass flow rate through the stages, Ω is the rotor speed and the subscripts 1 and 2 refer respectively to inlet and outlet condition. So, using the equation 23 and plotting the pressure ratio through the machine as function of $\frac{\dot{m}\sqrt{T_{01}}}{p_{01}}$ for several fixed value of $\frac{\Omega}{\sqrt{T_{01}}}$, is possible to understand at which conditions the machine operation stability is guaranteed. In figure 16, each of the constant velocity curves terminate at the *instability* or *surge line*; beyond this curve the operation is unstable, that means the machine behavior will be not predictable and performances are extremely affect by even small flow changes. At high velocity and low pressure ratio, the constant speed line becomes vertical: here the flow is choked, i.e. at least a shock wave occurs. Hence, as $\frac{p_{02}}{p_{01}}$ increases, the isentropic efficiency η_c rises quickly and losses decrease (see figure 16). For these reasons, transonic compressors are preferred to the subsonic one when high performance is required. In general, the machine will be allowed to operate along the so called *operating line*, which is set by the flow area downstream of the machine and is chosen to pass as close as possible to the maximum efficiency point. Usually, as reported in [1], for a turbojet engine compressor, this line will be placed at a fixed pressure ratio value in respect to the instability line, i.e. at a *surge margin* about $SM = 20\%$, where:

$$SM = \frac{(pr)_s - (pr)_o}{(pr)_o} \tag{24}$$

with $(pr)_o$ as pressure ratio in the operating line at a certain speed value, while $(pr)_s$ is the surge line pressure ratio at the same $\frac{\Omega}{\sqrt{T_{01}}}$. Considering the instability line, above it two phenomena could occur:

- *surge*: an axial oscillation of the total mass flow will be generated, with relative noise and mechanical vibration increase. The efficiency will decrease immediately.
- *rotating stall*: when it happens, the blades of the same row stall in separate patches which rotate around the annulus. This rotation is simply due to increase of flow incidence in the left side of the stall and to the relative decrease in the other side[20]. Therefore, the stall is led to move to the left, loading and unloading each blade at a frequency that may be close to the blades natural frequency. Hence, rotating stall could cause blades failure with a resulting severe increase in losses. About the mass flow, in this case it will be simply redistributed over the annulus without oscillation.

At this point becomes clear that both previous phenomena can be considered as a disturbance of the natural oscillatory modes of the compression system. In particular, the disturbance quickly grows into a large amplitude form wave, leading the machine to instability. For these reasons, the stability of a compressor can be considered equal to the stability of waves generated by surge and stall; damping them helps to keep the machine below the surge line. Casing treatments, for example, could help to damp the small amplitude waves rotating about the annulus prior to stall.
Finally, the non-dimensional mass flow value results fundamental in stability maintenance and, considering equation 23, it is related to the total pressure ratio, i.e. to Mach number. An inlet condition change, such as flow incidence angle variation, leads to speed change, and the machine can deviate from the operative line condition, as shown in figure 16. For these reasons, when varying flow property at inlet, an accurate stability analysis is strongly recommended, together with an off-design analysis.

Figure 16: Operative range of 10-stage compressor [1]

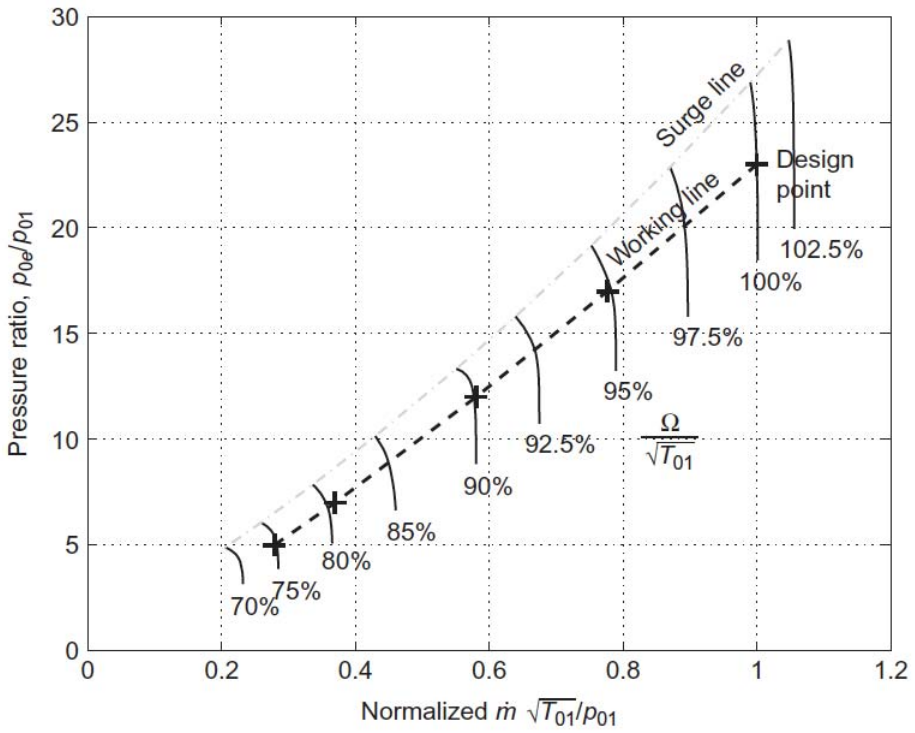

[20] as better explained in the next chapter, an increase in flow incidence could encourage blade stall

3 Compressor design

Compressors blades must be designed in order to make the flow achieving the required pressure rise, furthermore tolerating variation to the operative point without over-designing the machine. For these reasons flow properties, cascades and blades shape must be chosen carefully balancing benefits and drawbacks.

3.1 Cascade performance

The presence of more blades obliges the designer to consider additional parameter for an accurate performance evaluation. Therefore, in addition to Δs coefficient, diffusion factor, fluid deviation and incidence must be taken into account and their influence on losses requires an accurate analysis.

Diffusion factor Growth and separation of blade boundary layer can reduce dramatically the performance of the cascade; in particular, high levels of velocity diffusion on the blade surfaces tent to generate thick boundary layer with the resulting separation. Moreover, it is proved that the diffusion in velocity over the suction surface plays a much more severe role than the pressure one in losses generation; the reason, as better explained in [1], is that the suction side produces the largest portion of the blade wake. Hence, the difference between leading and trailing edge speed on that surface can be used as a boundary layer behavior quantifier and can be evaluated with the following *diffusion factor*:

$$DF = \left(1 - \frac{c_2}{c_1}\right) + \left(\frac{c_{\theta 1} - c_{\theta 2}}{2\,c_1}\right)\frac{s}{l} \tag{25}$$

where c_1, c_2 are the flow speeds at the two opposite corners of suction surface, $1 - c_2/c_1$ represent the mean deceleration, $c_{\theta 1}$, $c_{\theta 2}$ are the tangential components, $(c_{\theta 1} - c_{\theta 1})/2\,c_1$ is the flow turning while s/l is the pitch-chord ratio, as shown in figures 17,18. About the latter term, it proves how well the fluid is guided between the blades: a low value means lower pressure gradients across the blade passage required to turn the flow, i.e. a well guided flow, so low speed diffusion. When $DF > 0.6$ flow separation occurs, while a well-designed and high performing blade operates with a diffusion factor around 0.45. Finally, the equation 25 is used with both compressible and incompressible flows but for preliminary design purpose only. In the latter condition, DF equation can be written showing its dependance to flow angle, wake momentum thickness and, finally providing a simple relationship with total pressure loss coefficient[21].
Another way to evaluate the speed diffusion can be found in the *De Haller number*, simply the ratio between c_2 and c_1. As reported in [1], in order to reduce boundary layer losses, its value should remains above 0.72.

Figure 17: Flow velocity within a turbomachinery [1]

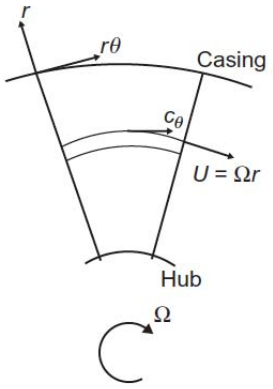

Figure 18: Velocity distribution above blade surface [1]

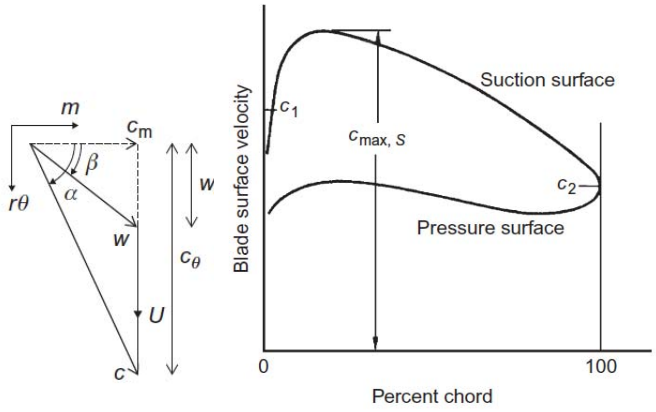

[21] incompressible case is reported here only for completeness. More details are found in [1] in chapter 3.5

Fluid deviation At trailing edge the flow does not follow the blade camber line completely; here diffusion plays an important role, making the flow not moving in a single direction and causing streamlines divergence. Moreover, blade pitch and boundary layer viscous effects will increase the fluid deviation: the first not allows the flow to well follow the passage shape while the latter leads to fluid blockage and relative blade shape modification. Hence, the flow deviation can be quantified as:

$$\delta^* = m\,\theta \left(\frac{s}{l}\right)^n \qquad \text{with} \quad m = 0.23 \left(\frac{2a}{l}\right)^2 + \frac{\alpha_2^*}{500} \tag{26}$$

where m depends on camber line shape and stagger, θ here stands for the blade camber angle, s/l is the pitch-cord ratio, n is a constant which value is about 0.5 for compressor cascades and 1 for inlet guide vanes, a is the distance from the leading edge along the camber line, α_2 the exit flow angle and the superscript $*$ refers to nominal or design conditions. So, the equation 26 demonstrates that the deviation increases with pitch-cord ratio and blade camber. Furthermore, as explained below, is possible to relate the above δ^* to the incidence angle i, showing how its increase will rise the flow deviation.

Incidence effect The incidence angle is simply the angle between the flow and the camber line tangent and it can be evaluated such as the difference between the inlet flow angle α and the *metal angle* α':

$$i = \alpha_1 - \alpha_1' \tag{27}$$

as shown in figure 5; obviously α' is the slope of the tangent to the camber line. Furthermore, while i varies from positive to negative values, over blade surface three different Mach number distributions[22] take place. From figure 19:

- if $i = 0$ the inlet flow angle is almost parallel to the camber line, giving a smooth and continuous pressure distribution and the deflection of the flow is entirely due to blade camber; for these reasons in this case (termed *design condition*), the flow angle α is called *optimum angle* (clearly equal to the metal angle) and losses due to boundary layer and separation are minimized.
- when $i > 0$ the fluid begins to flow against the blade pressure surface, accelerating on suction side near leading edge and suddenly decelerating to a speed comparable with the mainstream velocity. At this point high local diffusion, i.e. high DF values, leads to severe flow turning and blade loading; moreover, M_{iso} increases quickly near the leading edge on suction side, showing the so-called *leading edge spike*. As the incidence increases, boundary layer becomes thicker and near transition, while flow can separate leading to stall. Hence, with a positive i, losses are always higher than in other configurations.
- if $i < 0$ Mach behavior changes completely from the previous case, showing the opposite trend: at leading edge, on pressure side, the flow accelerates, increasing diffusion, while, on the other side, DF values become lower than at $i > 0$. Therefore, the whole flow turning is reduced, as well as the blade loading and obviously the overall losses. At very high values of negative incidence the diffusion become higher and the flow can separate on the pressure side.

Incidence and isentropic Mach number are related. Furthermore, when the flow becomes transonic, machine stability is strictly affected by incidence value and inlet speed. Indeed, from figure 20, at positive incidence the flow compression is limited by velocity diffusion on pressure side while at $i < 0$ choking and pressure side diffusion do not allow safe operation. In both condition, as the inlet speed approaches $M = 1$, the machine tolerance decreases quickly, i.e. flow will choke or starting to separate even with small deviation from design incidence.

[22] i.e. isentropic Mach number distribution, M_{iso} or M_s in figure 19

Figure 19: Incidence effects on blade isentropic Mach number [1]

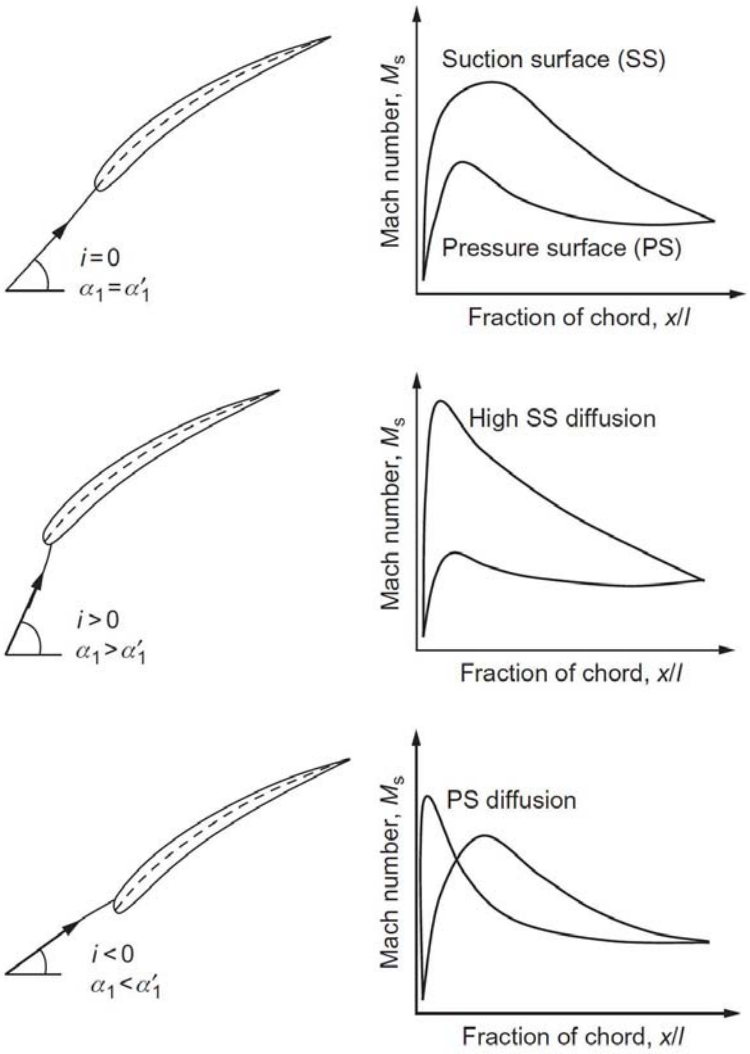

Figure 20: Incidence and inlet mach number influence on compressor stability [1]

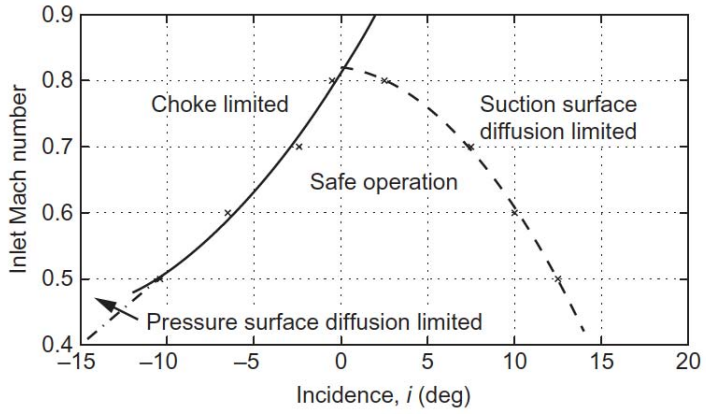

Unique incidence principle In a supersonic cascade with subsonic axial velocity, the inlet flow results dependent to the inlet Mach number, or better $\alpha_1 = f(M_1)$. This correlation simply comes from chocking condition, since when a normal shock occurs inside the passage, the back pressure can

be varied without affecting the upstream flow anymore. For this reason, at maximum back pressure (i.e. the p_2 value that caused the passage normal shock), the corresponding inlet flow conditions are called "unique incidence" condition; increasing that inlet angle means enhancing the detachment of the bow shock at leading edge. In section 3.4 this principle, together with the dependency depicted in figure 16, will be important to understand and justify the behavior of a precompression blade cascade at off-design conditions

3.2 Shock waves

At Mach number equal or above $M = 1$ the flow behaves in a different way than at lower speed. That difference is more severe when it interacts with a wall or in general in a duct and the results of this interaction can be useful in order to increase or decrease static pressure for "free" through the so-called *shock waves*. Three different types of shock waves exist, *normal*, *oblique* or *expansion waves*, all caused by the flow passage through $M = 1$ imposed by boundary conditions such as high outlet static pressure or section changes. Note that, when dealing with transonic and supersonic speed, the change in density must be taken into account, i.e. when $M > 0.3$ the flow is considered compressible and the density changes according to equation 28:

$$\frac{\rho_0}{\rho} = \left(1 + \frac{k-1}{2} M^2\right)^{1/(k-1)} \tag{28}$$

where ρ_0 is the total fluid density, ρ is the density of the part of the fluid at a certain speed and $k = c_p/c_v$ the specific heat ratio. As clear, the density decreases with the Mach number increase and its change is related to static pressure through the equation 1. In the next lines the different shocks features will be briefly explained. More details can be found in [9] chapters $7, 8, 9$.

Normal shock A normal shock is an *adiabatic* and *nonisentropic* phenomenon which implies a *discontinuity* in the flow. In particular, this discontinuity propagates through a gas such as an acoustic wave; the latter moves thanks to limited amplitude pressure waves at a speed a that depends on the elastic behavior of the fluid:

$$a = \sqrt{\upsilon\, E_s} = \sqrt{k\, R\, T} \qquad \text{with} \quad E_s = -\upsilon \left(\frac{\partial p}{\partial \upsilon}\right)_s = k\, p \tag{29}$$

where E_s is the isentropic bulk modulus of the gas (more details in [16]), $\upsilon = 1/\rho$ is the specific volume, R is the gas constant and a is also referred as *speed of sound*. Note that, once the gas type is chosen (i.e. R and k remains constant), the speed value varies with static temperature. Therefore, considering a fluid moving into a duct, where the flow reaches the sonic speed value a shock wave can occur with the resulting pressure perturbation. That nonisentropic perturbation affects the whole flow, splitting the field into two areas at different speed, one at supersonic ($u > a$), the other at subsonic speed ($u < a$). Not only speed and pressure show a discontinuity: static temperature, density, total pressure and obviously entropy change across the shock, while total temperature and total enthalpy remain the same. In particular, the flow properties variation ahead and behind the shock (respectively subscript 1 and 2 in figure 21), can be

Figure 21: Normal shock wave with flow conditions ahead and behind it [9]

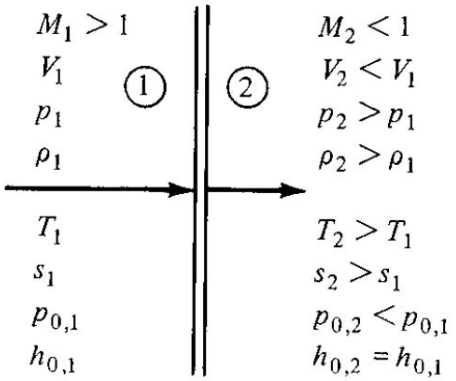

simply evaluated by using the continuity, energy and momentum equations rearranged as in equations 30÷32, plus the perfect gas law in equation 33 and sonic relation in equation 29. Note that, what happens inside the shock (where friction must be taken into account) can be neglected, focusing only on flow

$$u_1 + \rho_1 = u_2 + \rho_2 \qquad \text{continuity} \tag{30}$$

$$h_1 + \frac{u_1^2}{2} = h_2 + \frac{u_2^2}{2} = h_0 \qquad \text{energy equation} \tag{31}$$

$$p_1 + \rho_1 u_1^2 = p_2 + \rho_2 u_2^2 \qquad \text{momentum} \tag{32}$$

$$p\upsilon = RT \qquad \text{perfect gas law} \tag{33}$$

behavior just before and after the source of this perturbation. Therefore becomes useful to replace the speed expression with the *Mach number* formula, that allows to immediately distinguish subsonic from transonic flow:

$$M = \frac{u}{a} \tag{34}$$

where $M < 1$ for subsonic speed, while for supersonic velocity $M > 1$. Finally, when $M = 1$, the flow reaches the speed of sound, i.e. $u = a$ and in this case a shock wave occurs. At this point, the so-called *Prandtl-Meyer equation* can be reported, giving the basic relation for normal shock waves:

$$M_1^* \cdot M_2^* = 1 \qquad \text{with} \quad M^* = \frac{u}{a^*} = \frac{k+1}{2} \frac{M^2}{1 + \frac{k-1}{2} M^2} \tag{35}$$

where M^* is the critical Mach number and $a^* = \sqrt{k\,R\,T_0}$ is the critical speed of sound. Note that the equality just above simply imposes the M_2 value to be subsonic if M_1 is supersonic and vice-versa, permitting a shock to emanate from both subsonic or supersonic flow. Otherwise, a normal shock wave from a subsonic flow would make the entropy to decrease, breaking the second law of thermodynamics (i.e., from equation 3, if $M_1 < 1$ and $M_2 > 1$, the entropy value must decrease through the shock); a normal shock wave, with the resulting nonisentropic change in flow condition, is possible only from flow at speed above the speed of sound. For this reason, in the following lines, no reference to "subsonic normal shock" will be made anymore. Moreover, the T_0 dependence keeps the a^* value constant through the shock and allows the equation 35 to become the starting point for the remaining flow properties evaluation. Hence, from the Prandtl-Meyer equation, the Mach number behind the normal shock can be found in function of the upstream Mach number M_1:

$$M_2^2 = \frac{M_1^2 + \frac{2}{k-1}}{\frac{2k}{k-1} M_1^2 - 1} \tag{36}$$

Finally, static temperature, static and total pressure and density values change follows from the replacements of equation 36 into the rearranged energy equation 31:

$$\frac{T_2}{T_1} = \frac{\left(1 + \frac{k-1}{2} M_1^2\right)\left(\frac{2k}{k-1} M_1^2 - 1\right)}{\frac{(k+1)^2}{2(k-1)} M_1^2} \tag{37}$$

$$\frac{p_2}{p_1} = \frac{2k}{k+1} M_1^2 - \frac{k-1}{k+1} \tag{38}$$

$$\frac{\rho_2}{\rho_1} = \frac{k+1}{2} \frac{M_1^2}{1 + \frac{k-1}{2} M_1^2} \tag{39}$$

$$\frac{p_{02}}{p_{01}} = \left(\frac{\frac{k+1}{2} M_1^2}{1 + \frac{k-1}{2} M_1^2}\right)^{\frac{k}{k-1}} \left(\frac{2k}{k+1} M_1^2 - \frac{k-1}{k+1}\right)^{\frac{1}{1-k}} \tag{40}$$

As clear from figure 22 and equations 36÷40, upstream Mach number increase reduces speed and total pressure, while static pressure, static temperature and density increase. So, in order to obtain the higher pressure increase possible across the shock, M_1 value should be increase, obviously avoiding flow separation or severe loss generation.

Figure 22: Flow properties trend across a normal shock wave with $k = 1.4$ [9]

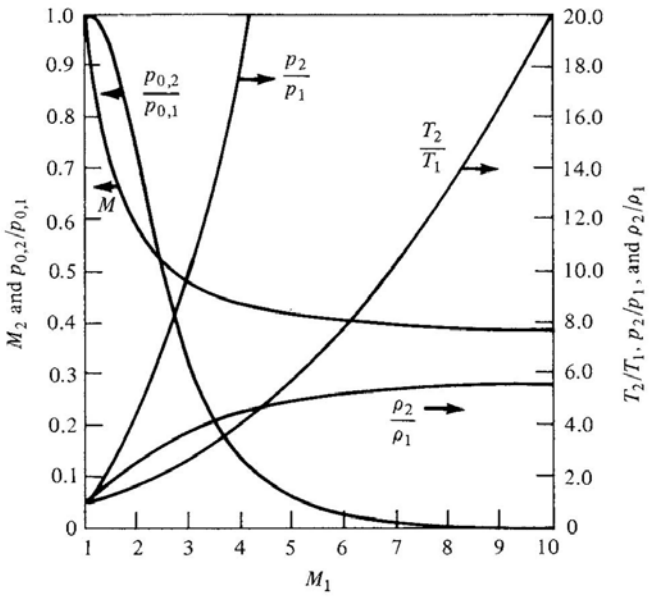

At the end can be useful to highlight the most important features of normal shock waves, in order to better understand how to exploit it in transonic compressors:

- The shock wave is a very thin region (thickness comparable to the free path of the molecules) in which friction and thermal conduction play an important role on the flow structure inside it. Outside it, no viscous effects will be taken into account
- No deviation is achieved: fluid remains normal to the shock
- Shock waves occur only from supersonic to subsonic speed when high value of back pressure are required to an initially supersonic flow
- Static temperature increase is not due to heat transfer from or to an external location, but to kinetic-to-internal energy conversion across the shock

- The increase in pressure is basically due to energy dissipation through the shock; therefore it is a "free" and sometimes positive result
- The ratio between the flow properties before and after the shock depends completely on inlet Mach number M_1
- Once the sonic condition is reached, the flow is chocked and any change in downstream flow condition does not affect the fluid before the shock
- Flow is considered steady and the body forces will be neglected

Oblique shock A normal shock wave is a particular case of the more common oblique wave. This discontinuity has the same nature of the previous one but is caused by a deviation of a supersonic flow along a *concave* surface, as shown in figure 23. Furthermore this deviation turns *upward* the streamlines into the main bulk of the flow through the same wall angle θ, while shock wave is also deflected through another angle β. For these reasons the main speed v must be split into normal and tangential component, as in figure 23. Hence, substituting $V^2 = u^2 + w^2$ into the continuity, momentum and energy equations 30÷32, the resulting governing equation for oblique shock wave are:

$$u_1\rho_1 = u_2\rho_2 \qquad \text{continuity} \tag{41}$$

$$w_1 = w_2 \qquad \text{momentum - tangential component} \tag{42}$$

$$p_1 + \rho_1\, u_1^2 = p_2 + \rho_2\, u_2^2 \qquad \text{momentum - normal component} \tag{43}$$

$$h_1 + \frac{u_1^2}{2} = h_2 + \frac{u_2^2}{2} = h_0 \qquad \text{energy equation} \tag{44}$$

In particular, in oblique shock the tangential component of the flow is constant across that shock (see momentum equation 42) and, as consequence, the property changes across the wave are governed only by the velocity component normal to the oblique shock wave, as clear in equation 44. Note that, despite they are written precisely in the same way, the speed in equations 30÷32, results made only by the normal component, i.e. $V = u$ in normal shock equations. Similarly, the correlation between upstream and downstream flow properties must be rearranged introducing the normal Mach number M_n:

$$M_{n1} = M_1\, \sin\beta \tag{45}$$

$$M_{n2} = M_2\, \sin(\beta - \theta) \tag{46}$$

where β is the angle between the inlet flow direction and the shock and θ gives the angle between the downstream flow and the shock, as shown in figure 23; hence, M_{n1} and M_{n2} are respectively the component of the pre- and post-shock speed in the direction normal to the wave. At this point, M_{n2}, T_2, p_2, p_{02} and ρ_2 can be evaluated from 36÷40 in terms of M_{n1} and through equation 46 the Mach number value of the outcoming flow is found.

Figure 23: Oblique shock wave with flow conditions ahead and behind it [9]

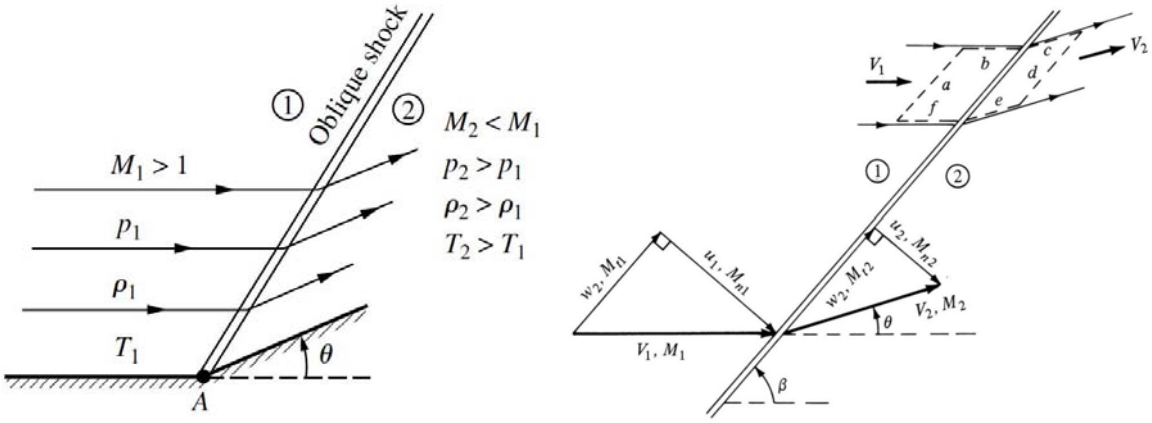

No more details can be given about the flow behavior until finding the correlation between the deflection angle and the shock wave angle. So, from continuity and momentum equations 41, 42 rearranged with speed components[23] and trigonometric substitutions, follows the $\theta - \beta - M$ relation:

$$\tan\theta = 2\,\cot\beta\,\frac{M_1^2\sin^2\beta - 1}{M_1^2(k + \cos 2\beta) + 2} \tag{47}$$

Therefore, the flow behavior across an oblique shock can be solved through θ and its maximum value θ_{max} once plotting this equation as in figure 25:

- when $\theta > \theta_{max}$ no straight oblique shock can occur and a detached shock is the only solution possible; indeed, for any given upstream Mach number M_1, a maximum deflection θ_{max} exists. In that case, the so-called *curve shock* shows a normal wave near the corner plus an oblique shock away from the wall, as better explained in paragraph 3.3. Hence, increasing the inlet Mach number, the range of θ raises, avoiding the detachment; moreover, that increase has a limit at about 45.5° , where M_1 approaches infinity

Figure 24: Oblique shocks: (a) attached and (b) detached [9]

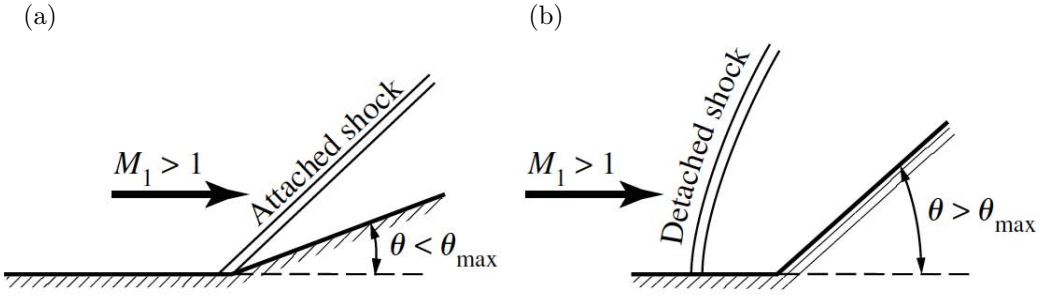

- when $\theta < \theta_{max}$, two straight oblique shocks are possible: a *strong solution* with a certain β value or a *weak solution* with a lower β angle[24]. So, above the $\theta = \theta_{max}$ curve (red dashed line in figure 25) the strong shock solution prevails with a steep shock wave, high normal component of upstream Mach number M_{n1} and the relative high compressed and subsonic downstream flow (i.e. $M_2 < 1$). On the other hand, below that line, the flow remains supersonic ($M_1 > M_2 > 1$) with a lower β value and less pressure increase. Note that, also in the weak case a subsonic solution is possible, but only very near θ_{max}. Finally, in nature, the more common solution is the weak one, so it can be state that with a straight, attached oblique shock is always $M_2 > 1$

[23] from figure 23 , $\tan\beta = \frac{u_1}{w_1}$ and $\tan(\beta - \theta) = \frac{u_2}{w_2}$

[24] the shock wave with higher β angle will compress the flow more than the lower-angle shock wave (see equation 38 with $M_1 = M_{n1}$); hence the term "strong" and "weak" solution

- if $\theta = 0°$, the strong solution is given by a normal shock wave (i.e. $\beta = 90°$) while the weak case occurs when $\beta = \arcsin(1/M_1)$. The latter angle is called *Mach angle* μ and represents the case of an infinitely weak oblique shock, the weakest shock wave possible, that behaves exactly as an acoustic wave. In both cases the flow streamlines will show no deflection
- at a fixed value of the deflection angle, an upstream mach number increase leads to a less steep shock wave and static pressure raise. In the other hand, with constant upstream flow speed, as the deflection increases the shock wave inclination and p_2 value become larger. Obviously only the weak solution is considered.

At this point is clear that normal shock waves are only a particular shock case that, in general in compressors, should be avoided while an attached, oblique shock with high p_2/p_1 value is preferred.

Figure 25: Oblique shock properties for $k = 1.4$ in the so-called $\theta - \beta - M$ diagram

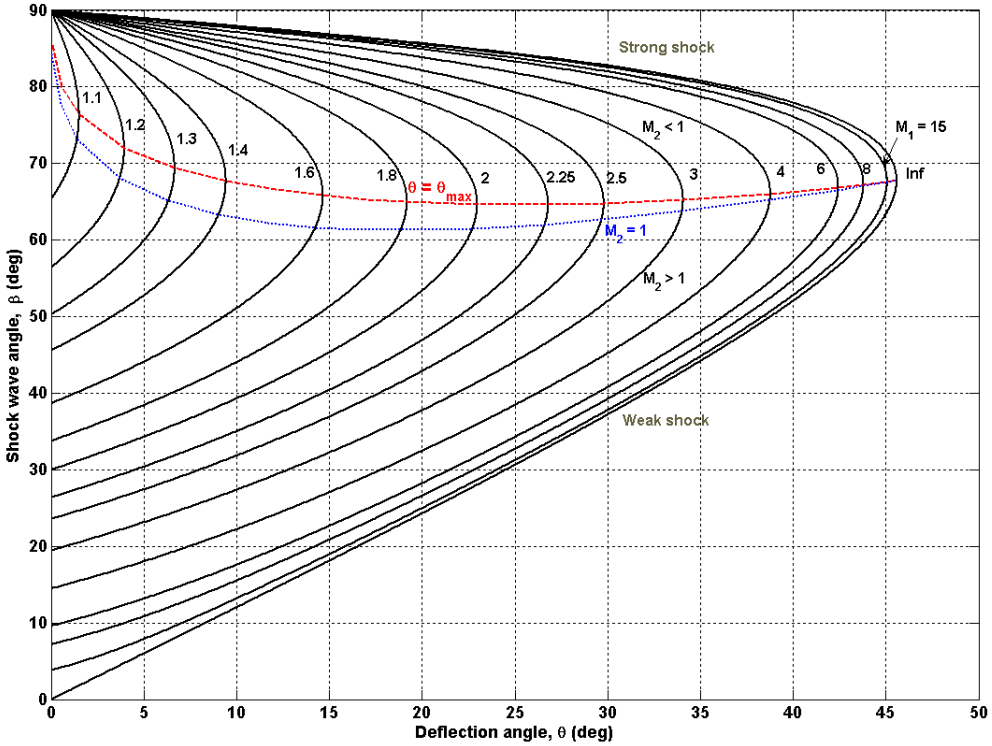

Expansion wave When a supersonic flow is turned *away from itself*, as in figure 26, an expansion wave is formed in a shape of a fan centered in the wall convex corner. This expansion fan is a *continuous expansion region*, that can be seen as an infinite number of very weak Mach waves, each making the Mach angle μ with the flow direction. In particular, the originally horizontal streamlines ahead of the expansion wave are deflected smoothly and continuously through the expansion fan such that the streamlines behind the wave are parallel to each other and inclined downward at the deflection angle θ. This continuous deflection, that is bounded upstream by a Mach wave with the angle μ_1 with respect to the flow and downstream by another Mach wave with the angle μ_2, causes an *isentropic expansion*.

Figure 26: Expansion wave with flow conditions ahead and behind it [9]

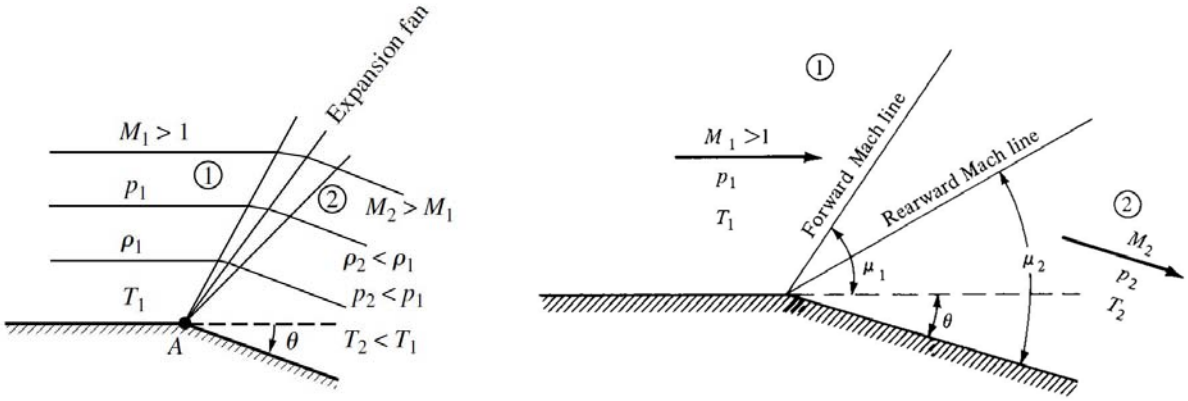

Hence, unlike normal and oblique shock, across an expansion wave the entropy does not change ($\Delta s = 0$) and $T_{01} = T_{02} = T_0$, $p_{01} = p_{02} = p_0$. This important feature, bound with the continuous flow change through the expansion fan, allows to describes the behavior of the flow inside the wave with the following differential equation:

$$d\theta = \sqrt{M^2 - 1}\,\frac{dV}{V} \tag{48}$$

where the infinitesimal change in velocity dV is related to the infinitesimal deflection $d\theta$. Integrating the first side of the equation 48 between 0 and θ, the second term between M_1 and M_2, and after some rearrangements, the so-called *Prandtl-Mayer function* $\upsilon(M)$ can be written:

$$\upsilon(M) = \sqrt{\frac{\gamma+1}{\gamma-1}}\,\tan^{-1}\sqrt{\frac{\gamma-1}{\gamma+1}(M^2-1)} - \tan^{-1}\sqrt{M^2-1} \tag{49}$$

$$\theta = \upsilon(M_2) - \upsilon(M_1) \tag{50}$$

where the speed-dependent function υ is the key to the evaluation of the flow properties change across an expansion wave. In particular, after calculating $\upsilon(M_1)$ then $\upsilon(M_2)$ thanks to equation 50 and the known θ angle, is possible to find the downward Mach number M_2 again from the Prandtl-Mayer function. At this point, the remaining properties follows from isentropic relation for a calorically perfect gas.
Finally, summing up the most relevant features of expansion waves, is possible to note that:

- unlike an oblique or normal shock, an expansion wave is not a "line", but an ensemble of infinitesimal shock waves that spread out from the wall corner, imposing a continuous and so isentropic change in speed and direction to a "slice" of the flow
- across that shock the flow speeds up, the static pressure decrease as static temperature and density do. For these reasons, while an oblique shock is required to increase the static pressure "for free", an expansion wave can be used to re-accelerate the flow after a shock in order to spoilt all the energy of the fluid
- thanks to its isentropic behavior, an expansion wave does not create losses making this kind of wave even more different from the previous phenomena

In order to close this brief introduction on shock wave, it can be useful to note that oblique and expansion waves are two or three dimensional while normal shocks are pretty one dimensional. Furthermore, across each shock the flow streamlines can be deviated but remain at the same distance from each other.

3.3 Transonic flow in cascades

When flowing inside a duct, section changes, wall boundary layers and obstacles can modify the flow behavior and influence existing phenomena such as shock waves; in turn, shock waves can "change" the geometry seen by the fluid in order to reached the exit flow conditions. Hence, what happened for example inside a compressor cascade required more attention and deeper analysis. In the next lines this need will be satisfied.

Section change A concave or convex surface imposes a deviation to the flow causing non-isentropic phenomena such as oblique shock. Moreover, when dealing with variable-area-duct, its section increase or decrease can isentropically influence the flow behavior even with no shock wave or entropy-losing phenomena. In such case, starting from the differential form of the continuity and the energy equation for an inviscid, adiabatic flow, respectively $d(\rho V A) = 0$ and $dh + VdV = 0$, a relation between density ρ, speed V and area A change can be found:

$$\frac{d\rho}{\rho} + \frac{dV}{V} + \frac{dA}{A} = 0 \tag{51}$$

After some other passage and thanks to the pressure-density dependence in isentropic flow[25], the so-called *area-velocity relation* in equation 52 allows to relate directly area and velocity change:

$$\frac{dA}{A} = (M^2 - 1)\frac{dV}{V} \tag{52}$$

Hence, when a flow enters a variable-area duct as in figure 27, its response to section change depends on its inlet velocity:

- if the incoming flow is subsonic, i.e. $0 \leq M < 1$, the term between parentheses in equation 52 is negative. Hence, through converging ducts ($dA < 0$) the flow will speed up ($dV > 0$) in order to maintain the equality in the area-velocity relation; in the other hand, in diverging ducts ($dA > 0$), the speed will decrease ($dV < 0$)
- if the incoming flow is supersonic, i.e. $M > 1$, the term between parentheses in equation 52 is positive. Hence, through converging ducts ($dA < 0$) the flow will speed down ($dV < 0$) in order to maintain the equality in the area-velocity relation; in the other hand, in diverging ducts ($dA > 0$), the speed will increase ($dV > 0$)
- when $M = 1$, the equation 52 reaches its minimum value, or better the sonic condition is achieved in a section of the duct with the smallest area.

Figure 27: Compressible flow in converging and diverging ducts [9]

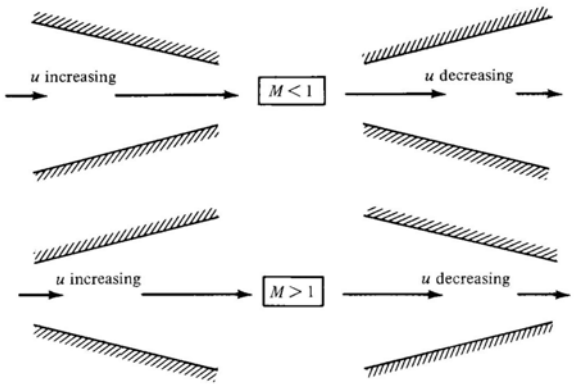

This latter point requires more clarification since $dA/A = 0$ mathematically can correspond even to a local maximum in area distribution. Contrariwise, this condition will be soon discarded when

[25] for the moment, no shock waves or non-isentropic phenomena will be taken into account. Hence, for isentropic, compressible flow $dp = -\rho V dV$

considering a nozzle/diffuser, i.e. a combination of a converging and a diverging duct which aims is to isentropically speed up/down a fluid, as depicted in figure 28*a*: indeed, from equation 52, the only way to make subsonic an initially supersonic flow is to reach the sonic condition in the section of the duct where A is minimum, i.e. in the so-called *throat*. Likewise, a subsonic flow becomes supersonic only accelerating and passing through the duct throat at $M = 1$. Hence, in an isentropic nozzle or diffuser the throat area A_t coincide with the "sonic section", or better $A_t = A^*$. This known area can be used to evaluate the Mach number at any location in the duct thanks to the following *area-Mach number relation*:

$$\left(\frac{A}{A^*}\right)^2 = \frac{1}{M^2}\left[\frac{2}{k+1}\left(1+\frac{k-1}{2}M^2\right)\right]^{\frac{k+1}{k-1}} \tag{53}$$

in which A is the area of the section in the chosen location and $A/A^* < 1$ since $A_t = A_{min} = A^*$. Therefore, the area-Mach number relation gives two possible solutions for M at a given A/A^*, one subsonic and another supersonic; the choice between these cases depends on pressure at inlet and outlet of the duct. Moreover, equation 53 confirms again that, after chocking, the sonic conditions throat are the only connection between the supersonic and the transonic area (more details in chapter 3.2). So, since equation 53 states that $M = f(A/A^*)$, the distribution of M and hence the resulting distribution of p and T are univocally given once the nozzle area distribution is known.
At the end, consider the nozzle in figure 28b: there, the flow is not isentropic any more, hence total pressure and entropy do not remain constant. Section changes speed up/down the flow again but even thanks to oblique shocks (where the flow is turned against itself), expansion shocks (where the flow is turned away from itself) and normal shocks. Moreover, due to entropy increase across the shock waves and in boundary layer, the real throat area becomes $A_t > A^*$. This is a clear example of how a compressor cascade can be designed in order to compress a flow in the best way possible.

Figure 28: Supersonic diffusers: (a) ideal (isentropic) and (b) real case [9]

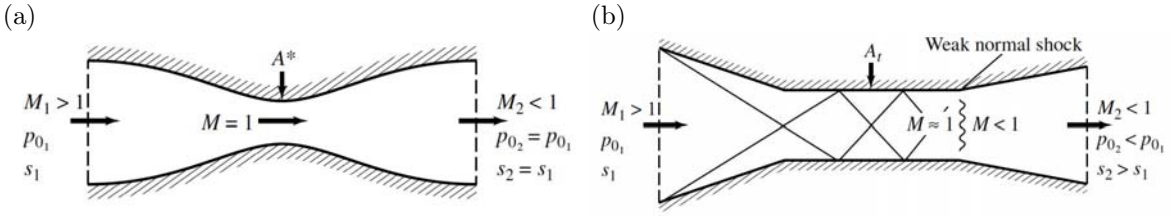

Detached shock When the deflection imposed to a supersonic flow is too severe, i.e. $\theta > \theta_{max}$, a detached and curved shock occurs. In particular, with the blunt body in figure 29, the shock is at distance δ from the nose and is a combination of normal and oblique shock waves. Therefore, the so-called *curved bow shock* shows in point a a normal shock, with the relative subsonic and rectilinear flow after the wave. In point b, the shock becomes oblique and the flow follows the strong shock-wave solution, as showed in figure 29. Here, the deflection increases and reaches its maximum at point c. Above it, all the points correspond to the weak solution and from c' the downward flow remains supersonic. In particular, in this position, the so-called sonic line divides the supersonic from the subsonic flow. Moreover, the shape of the detached shock, its distance δ and flow behavior between the wave and body nose depend on M_1 and the shape of the body.
Obviously, this flow condition with normal and strong oblique shock wave should be avoided in order to decrease losses and flow detachments (more details in paragraphs 2.3 and 3.2). Finally, the above analysis can be applied either to the detached shock case in figure 24b. Note that, bow shocks and in general shock wave over a cone extend in three-dimensional space: therefore the two-dimensional oblique shock theory in section 3.2 is no longer sufficient and a more sophisticated analysis is required, as better reported in chapter 4 of [17] and in chapter 9 of [9].

Figure 29: Curved bow shock over a supersonic blunt body and its $\theta - \beta - M$ diagram [9]

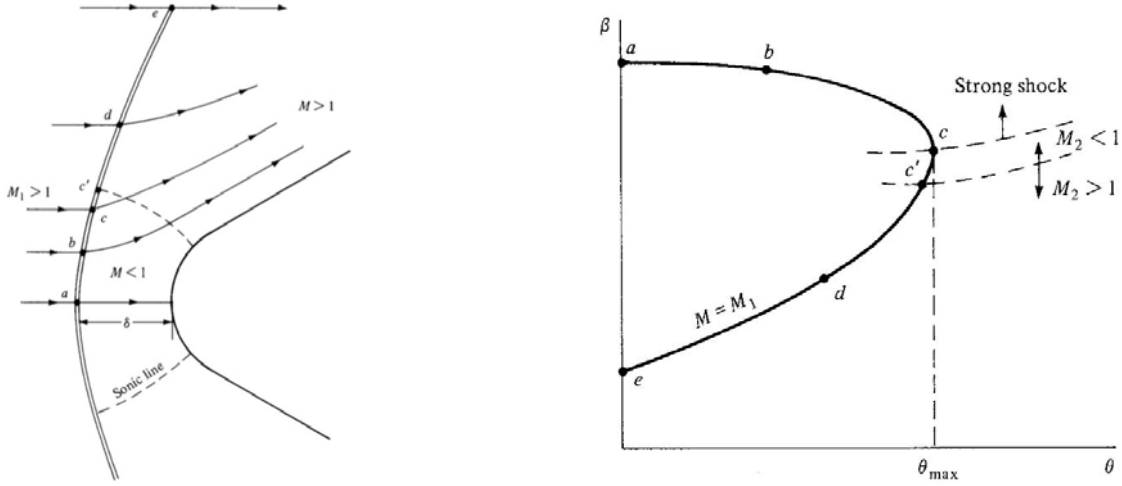

Shock interaction and reflection The oblique shock in figure 23 seems to extend unchanged to infinity. However, in real inviscid transonic flow, the *incident shock wave* can impinge against a solid boundary like the wall of a duct or a blade side, generating another wave, called *reflected shock wave*; both waves can be *left running* or *right running*, depending on starting point position and flow conditions. Considering the case depicted in figure 30a, the incident left-running shock, generated at A, diverts the flow by the concave surface angle θ making the streamlines no longer parallel to the upper straight wall; so, in order to satisfy the no-slip condition along that surface, another shock wave branches from the impingement point B turning the flow tangent to the wall again. In particular, three different region can be distinguish: in region 1 the flow is supersonic with no deflection ($\theta_1 = 0$); in region 2 the streamlines are turned upward by an angle $\theta_2 = \theta$ and the speed decreases through the oblique straight shock ($M_2 < M_1$); in the third part of the flow, streamlines must be turned downward and become tangent to the upper wall, so $\theta_2 = -\theta$ with the related $M_3 < M_2$ and $\Phi \neq \beta_1$. At this point, two different solution can occur:

- if $\theta < \theta_{max\,3}$, i.e. M_1 is quite enough above the minimum speed for a straight oblique shock, so either M_2. Therefore, both the shocks are straight, as showed in picture 30a. The flow properties can be simply evaluated applying the oblique shock formulation, first for the shock between region 1 and region 2, suddenly to the flow passing through the reflected wave. Note that, considering the more common weak shock solution only (see figure 25), the flow remains supersonic in the whole pattern

- if $\theta > \theta_{max\,3}$, i.e. the flow after the incident shock is too slow. Therefore, the incident shock must be curved near the upper wall, terminating with a normal shock, named *Mach stem* and the reflected wave becomes curved too, as depicted in picture 30b; consequently, the streamlines at the upper wall are allowed to continue parallel to the wall behind the shock intersection; for these reasons this wave pattern is called *Mach reflection* and can be numerically solved only by the Von Neumann's *three-shock theory*. To conclude, in this case the flow becomes subsonic, but only after the normal shock and strictly above the *slip line* or *slipstream* (a discontinuity over which the pressure remains the same, Mach number has identical direction, entropy changes discontinuously and viscous effects influence the flow). More details can be found in [18]

Figure 30: Oblique shock reflection from a wall: (a) regular (straight shock) and (b) Mach reflection (curved shock) [9]

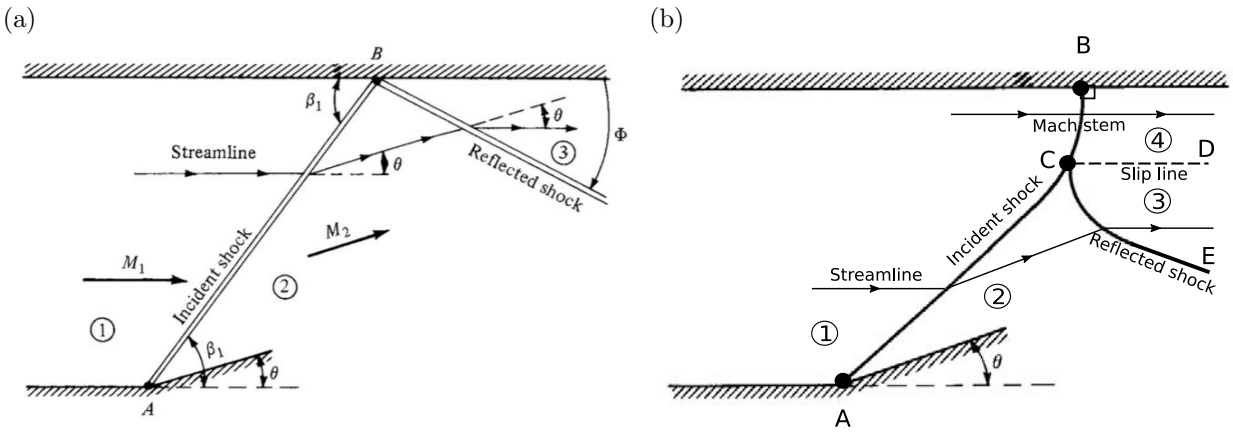

Another type of shock interaction is depicted in figure 31a, in which a left- and a right-running straight shocks impinge in point E generating the two refracted waves called respectively C and D. Considering a duct with walls at different slope (e.g. $\theta_1 > \theta_2$), the fluid deviation in region 2 is higher than in region 3, as consequence, $M_2 < M_3$. The following shocks turn the streamlines in region 4 parallel to streamlines in region $4'$, in order to maintain velocity across the slip line at the same direction (but not with equal magnitude). Moreover, if $\theta_1 = \theta_2$, the intersecting shocks will have the same strength, flow pattern become symmetrical and $s_4 = s_{4'}$, so there is no slip line. In addition, note that, depending on upstream conditions, the two incident shocks A and B can become curved and meet at E with normal shocks.
Finally, two left-running shocks generated at corners with different slope will impinge and two straight oblique shock will branch from the intersection point, as suggested in [17] and in figure 31b. Actually, the shock named CD is the natural propagation of the two incident waves, while the shock CE is a reflected wave that can be a weak oblique shock or a expansion wave. The purpose of this ambivalence is to change flow conditions in region 4 in order to satisfy slip line requirements, i.e. $p_4 = p_5$ and $\theta_4 = \theta_5$; moreover, this choice depends on the upstream conditions θ_1 and θ_2.

Figure 31: Intersection of: (a) a right-runnig and left-running shocks and (b) two left-running shocks [9]

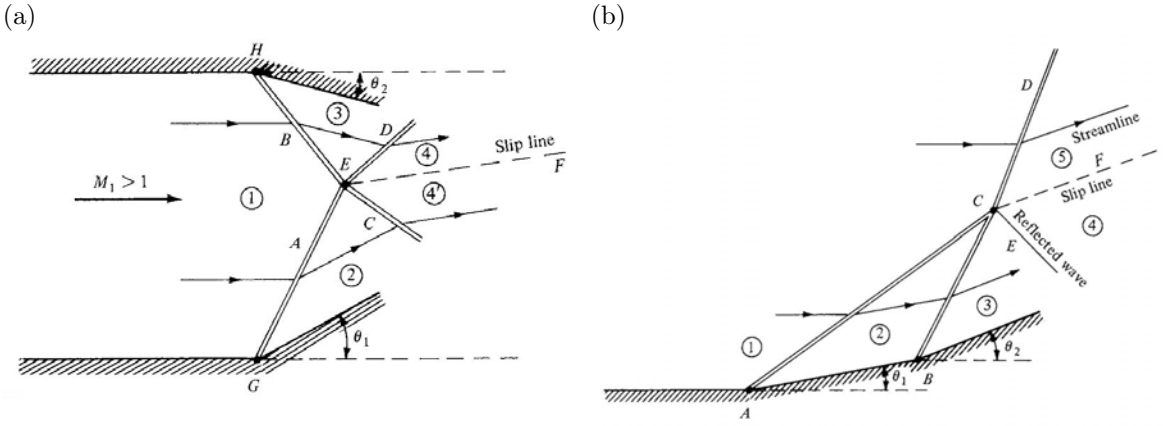

Shock-boundary layer interaction Taking into account the afore neglected viscosity, boundary layer presence influences shock waves behavior and vice versa, however not mixing and imposing a severe change in flow properties. For these reasons becomes necessary to focus on the flow configuration depicted in figure 32: a incident shock wave emanating from point A impinges the boundary layer at point D, not directly the wall. The infinitely large adverse pressure gradient, experienced in the impingement point, will make the boundary layer to separate from the surface. In the separation region the flow becomes subsonic, while in the opposite side of the boundary layer it is still supersonic; this huge pressure difference moves the separation point ahead of the theoretical inviscid

flow impingement point, i.e. in C. In turn, from this point, the separated boundary layer deflects the supersonic flow into itself generating a second shock wave, called *induced separation shock wave*; moving downward, the boundary layer will reattach at point E, turning the flow upward and so causing a third shock wave (*reattachment shock wave*); between the second and the third waves, as obvious, expansion waves occurs speeding up the flow; finally, further away from the plate, at point F, the separation and reattachment shock merge in the conventional reflected wave already experienced in inviscid flow. Note that, a laminar boundary layer will separate more readily than turbulent boundary layer, with the related more severe attendant consequences. Consequently, as suggested in [9], this shock-boundary layer interaction will increase total pressure loss, enhance the peaks of heat-transfer rate and encourage flow separation. However, at second glance, this interaction seems to improve flow performance and directly control fluid direction. To better explain the last sentence, take the case of the over expanded nozzle in figure 33a as reported in [19]. Here, the nozzle expansion ratio (exit-to-throat area ratio) is too large for a given nozzle pressure ratio (exit-to-inlet pressure ratio), i.e. the p_f/p_0 value from equation 53 with A_f/A_t is lower than the real nozzle pressure ratio (where $p_f = p_a$); therefore, the flow is driven to expand below exit back pressure. At this point, only flow separation from the nozzle flaps and the two related *lambda-shape shocks* allow the fluid pressure to enhance, reaching the required exit value. The named lambda-shape shock is a evolution of the shock system $ABCD$ in figure 32: the incident shock AB is replaced with a curved oblique shock that affects the middle of the duct, while the remaining waves are straight oblique shocks; hence, the lambda structure is the combination of two identical and specular Mach reflection phenomena (see figure 30b). With this configuration, the flow is subsonic beneath the separations bubble and after the shock center, however it remains supersonic in other flow regions. Moreover, after the shock, the actual section is reduced to A_0 by the separation bubbles, remaining constant until the exit ($A_f = A_0$) and obtaining the desire A_f/A_t value (see figure 33a).

Figure 32: Schematic illustration of shock wave-boundary layer interaction [9]

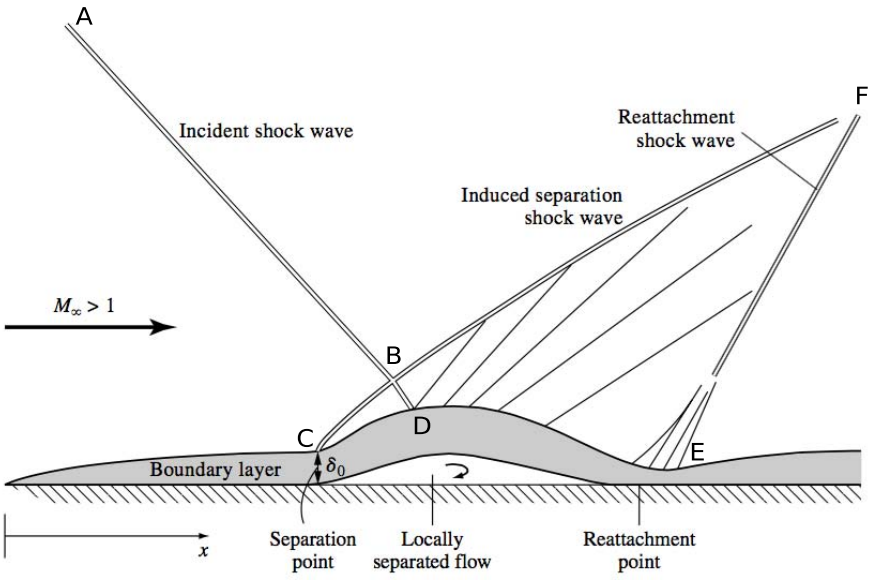

This "pressure adjustment mechanism" becomes important at off-design conditions, where the shock system moves upward and downward inside the nozzle in order to adapt the pressure to the exit value, changing the effective flow section. Therefore, the nozzle centerline pressure trend in figure 33b shows a different behavior as the inlet pressure p_0 decreases (or better, as the $NPR = 1/(p_a/p_0)$ reduces). Near design condition. i.e. $NPR \leq 5.423$, the pressure trend has no shock induced peaks since the exit pressure value is reached (hence, from picture 33a, $p_f = p_a$). At NPR just below 5, the flow becomes over expanded ($p_f < p_a$): a lambda-shape shock occurs within the nozzle outlet causing the p to increase to the exit value. As the inlet pressure decreases, the shock moves upstream and the "pressure step" becomes larger; as soon as NPR reaches 1.4, the huge pressure rise starts at throat ($x/x_t = 1$), where a normal weak shock develops. In order to better understand that pressure adjustment trend, the Schlieren photographs in figure 34 are necessary. At design condition

(figure 34a), the sonic velocity is reached before the nozzle throat (dark band ahead of $x/x_t = 1$), then flow pressure is decreased by expansion waves and suddenly a left- and right-running straight shock system enhances p_f to the exit value p_a; so no lambda-shape shocks are required and the flow is completely attached inside the duct while expansion fan emanates from the nozzle side at exit. Decreasing the NPR, the flow inside the duct becomes dependent of pressure ratio and at $NPR = 3.4$ the lambda-shape shock appear at exit, the flow separates between the lambda feet and nozzle walls causing the decrease in actual exit area. In figure 33c, the expansion and compression waves inside the nozzle disappear, the lambda shock system approaches the nozzle throat and the flow shows fully detached boundary layers; this separation imposes stronger turning requirements than a closed separation bubble and so it requires a bigger oblique shock system. For these reasons the size and extent of a lambda foot is more a result of separation effects than the development of basic shock-boundary layer interaction conditions. Furthermore, the separation point behaves like the nozzle exit, decreasing the expansion ratio and reducing the flow area to the area along the shock steam. Finally, at very low pressure ratio (see figure 33d), only a normal weak shock occurs at nozzle throat and no flow separation develops since the boundary layer is too thin.
In conclusion, the flow separation is not the mere result of a strong shock-boundary layer interaction but the natural trend of an over expanded nozzle flow to adjust the expansion ratio through separation. In other words, the flow detachment depicted in figures 33 is the result of the shock-boundary layer mutual dependence. Therefore, when a inlet flow state change (e.g. the inlet Mach number) does not allow the fluid to adapt to nozzle exit conditions, a shock induced boundary layer separation can "vary" the nozzle geometry adjusting the outlet pressure and meanwhile "choosing" the more efficient and lower expansion ratio. For these reasons, off-design nozzle thrust efficiency can be improved encouraging stable separation and controlling its location and extent through passive porous cavity or thanks to specific geometrical devices.

Figure 33: Overexpanded nozzle flow (a) sketch with lambda-shape shocks and (b) centerline pressure trend at different $NPR = p_0/p_f$ values [19]

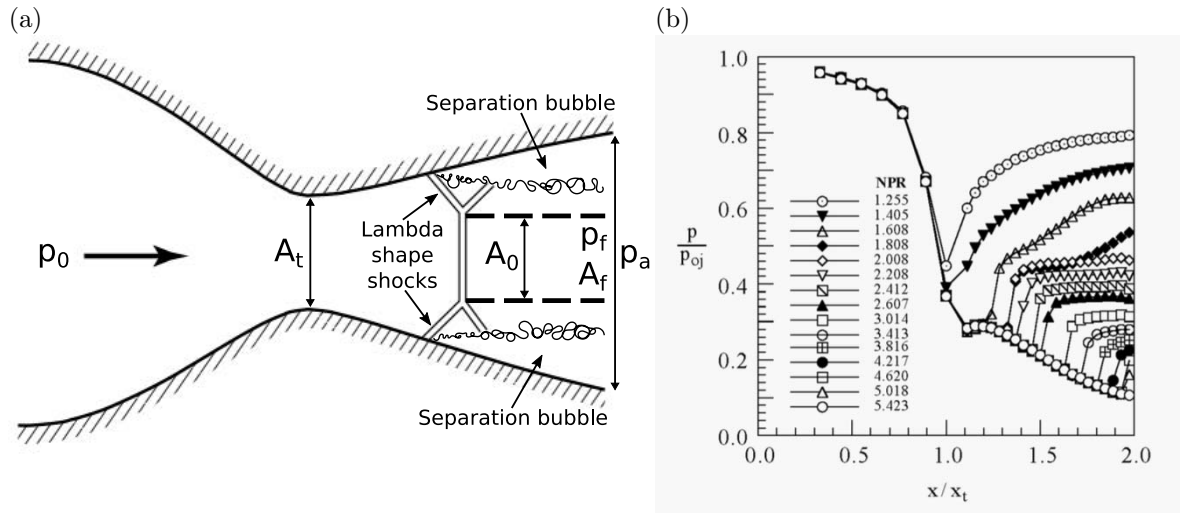

Figure 34: Schlieren photographs of a overexpanded nozzle at several NPR values: (a) 8.95, (b) 3.4, (c) 2.0 and (d) 1.4 [19]

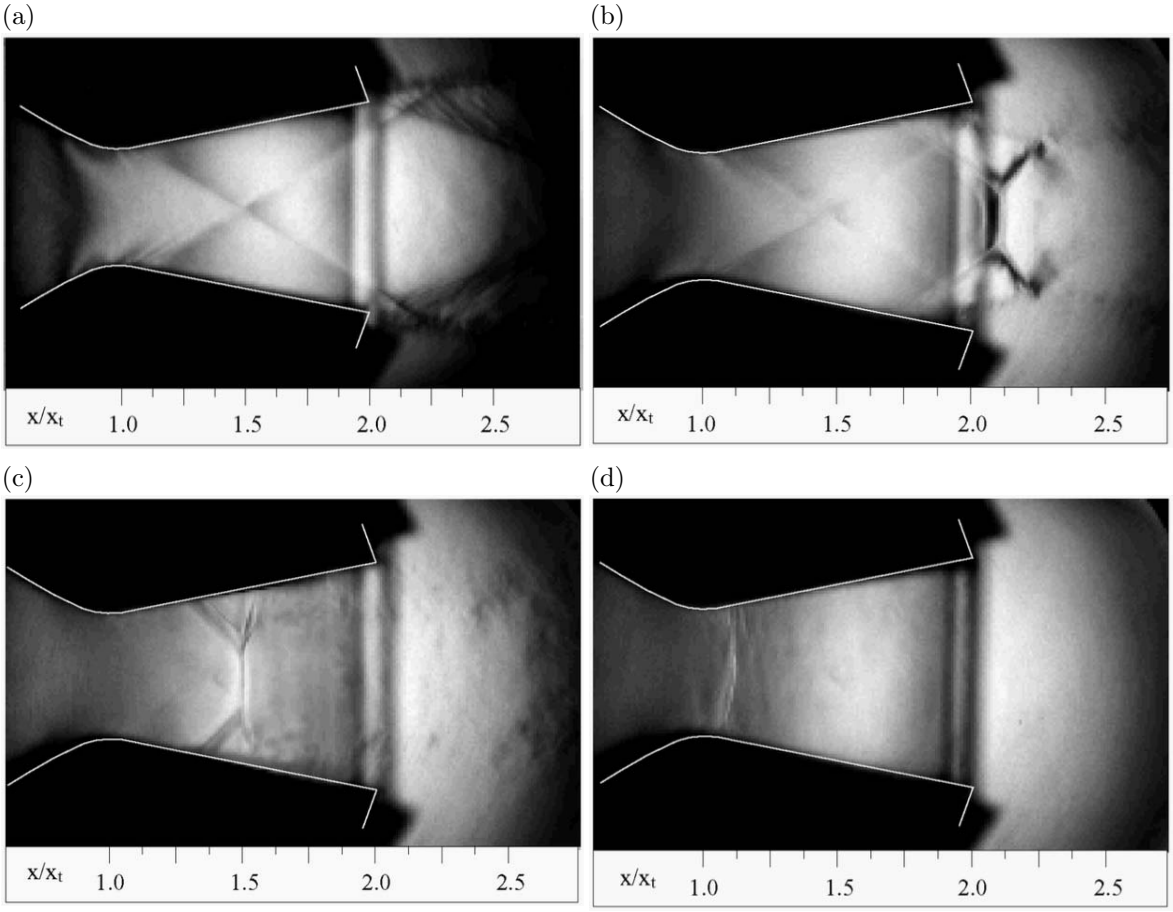

3.4 Precompression blade

In order to achieve a low-loss cascade, pressure gradient on the the airfoil should be minimized reducing shocks strength and avoiding normal or strong oblique shocks; moreover, the inlet flow velocity should be reduced as well as the flow separation. Finally, the cascade should be able to operate at off-design conditions remaining in safe-operation range (see 16). Accordingly with this consideration, in a supersonic compressor cascade, low losses and so high performances can be achieved using *precompression blade*, also called *s-shape blade*. As showed in figures 5 and 35a, this blades class reveals a very thin leading edge, a characteristic concave shape of the suction side at inlet, a thickness concentrated towards the trailing edge and a s-shape camberline. Such features lead to a flow behavior inside the cascade that can differ from the situation depicted in the previous sections. Before going on, becomes necessary to distinguish the cascade dependent flow parameters from the independent flow variables: the latter are obviously the inlet Mach number M_1, inlet flow angle, the static pressure ratio p_2/p_1 and the axial-velocity-density ratio $AVDR$, as reported in equation 54; however, exit flow angle, exit mach number M_2 and total pressure loss coefficient Y_p are strongly influenced by the previous variables. Note that, in chocking condition, the flow incidence at inlet becomes dependent to M_1 too (following the unique incidence principle, as reported in section 3.1).

$$AVDR = \frac{\rho_2 \, c_{x2}}{\rho_1 \, c_{x1}} \tag{54}$$

Shock model A typical shock pattern of a supersonic cascade can be reduced to the so called two-shock model, in which a detached bow shock, two oblique strong shock (at inlet and in the middle of the passage) and a completely separate boundary layer on suction side generate large pressure gradient and so high value of losses. Thereby, as suggested in [13], the reduction of the inlet Mach

number through a precompression blade makes neglectable the bow shock detachment, turns the first normal shock into oblique shock, reduces the strength of the second passage shock and tends to avoid downstream boundary layer separation on suction side. In particular, taking as example modified two-shock model reported in [13] and depicted in figure 35b, the negative camber surface near leading edge turns the flow into itself generating left-running compression weak shocks that isentropically reduces the fluid velocity and intersect the bow shock of the adjacent blade (point B). The left-running bow shock (AF), that turns into subsonic velocity the flow just ahead the blade leading edge, attenuates rapidly its strength with distance; nevertheless, it enters in the blade passage impinging the adjacent blade boundary layer. This interaction, generates a delta-shape shock (EF) and cause large boundary layer separation (point D). The second passage shock (G) is normal and, depending on inlet flow condition, does not interest the whole blade-to-blade section. Note that, all the possible shock patterns of a supersonic compressor cascade are simply the combination of the flow and shock interaction reported in chapter 3.3.

Figure 35: Precompression blades in ARL-SL19 supersonic compressor cascade: (a) section and geometrical parameters and (b) shock wave pattern at design condition

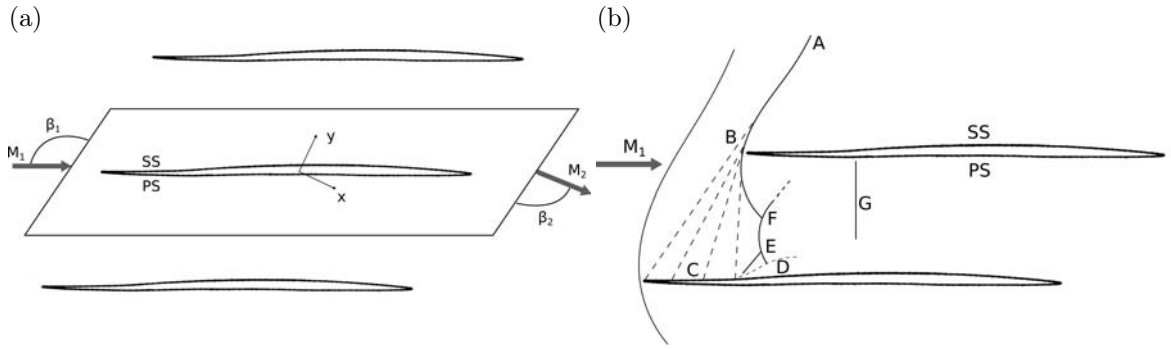

Off-design condition At this point, changing the independent flow variables, the above depicted flow pattern can vary completely. Remembering the unique incidence principle (i.e. the inlet flow angle is imposed by the shock ahead of the blade and back pressure change does not affect the upstream flow), $AVDR$, inlet mach number and static pressure ratio influence on cascade shocks behavior will be analyzed. At first, as the inlet Mach number enhances, the maximum static pressure achievable increases, as well as the total pressure loss. On the other hand, the variation of cascade static pressure ratio (fixing the remaining inlet conditions) causes a large alteration in blade passage and exit flow fields, besides affecting the cascade performances. In other words, pressure ratio and so back pressure rise strengthens shock-boundary layer interactions with the relative increase in boundary layer separations and Mach reflections; moreover, as p_2 become larger, an already formed lambda-shape shock system (e.g. DEF in figure 35b) moves upward reducing its strength until it almost disappears; at the same time, an oblique shock inside the passage will form a lambda-shape shock with the related boundary layer complete separation; hence, back pressure increase cause an increment in viscous losses while losses due to shocks are reduced. Last but not least, $AVDR$ increase will shift upstream the second passage shock, steepening the wave at inlet and so reducing the effective section between the blades (as happens when large boundary layer separation and so lambda-shape shocks occur, as explained in section and figures 34). In addition, the exit flow angle (i.e. β_2 in figure 35a) reduces while the flow turning increase ($\beta_1 - \beta_2$ with fixed inlet condition β_1) in order to maintain a constant static pressure ratio and so a constant exit flow area; in other words, as the $AVDR$ increase, the related section contraction will be avoided simply maintaining the flow more parallel to the passage walls. In conclusion, reduction in losses can be achieved enhancing $AVDR$ value and this decrease will be more severe at higher static pressure ratios. Note that, this performances increase occurs only with sonic-to-subsonic exit conditions, as suggested in [20]. Moreover, the $AVDR$ value can varied keeping constant p_2/p_1 thanks to the unique incidence condition.
As an example, the graphs in pictures 36 show how, as $AVDR$ and p_2/p_1 increase with fixed inlet Mach number, the curved shock at the end of the passage moves upward becoming even more thin and normal, while the oblique shock at entrance turns into a delta-shape shock. Considering the M_{iso} trend along the blade pressure side, the progressive reduction of leading edge peak (the so-called sonic pocket) from 1.4 to 1.1 is simply due to rear shock shifting and weakening; on the other hand, the

lambda-shape shock generation and the related increase in boundary layer separation on suction side, cause the M_{iso} trend to becomes steeper within the passage inlet; in particular, the isentropic Mach number shows a steep decrease near suction side separation point, i.e. where the delta-shape shock occurs. Similarly, the total pressure loss coefficient Y_p (named ω_η in pictures 36) shows a decrease in shock induced losses (i.e. a reduction in ω_η peak at half blade pitch) and an increase in boundary layer losses (i.e. ω_η values at passage sides become higher).

Figure 36: Influence of static pressure ratio on isentropic mach number, shock pattern and pressure loss coefficient at $M_1 = 1.58$ and different AVDR [20]

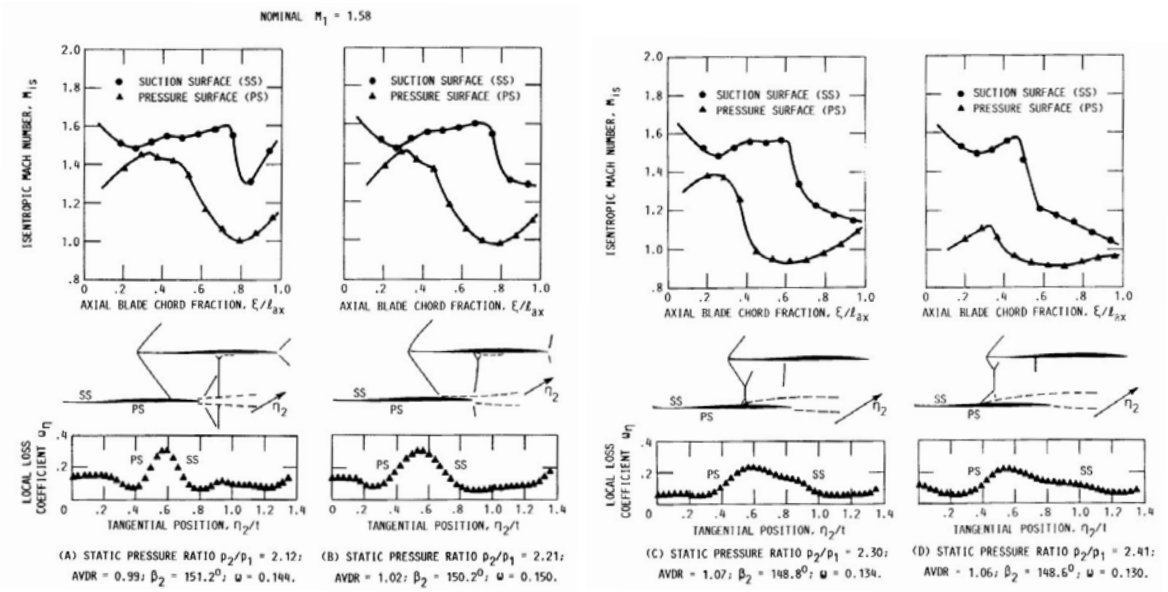

Strong interaction region The lambda-shape shock at passage inlet requires a further analysis, since its interaction with boundary layer and the flow can change the whole cascade performance. The detached bow shock in front of the blade branches into two oblique shocks, the weaker extends into the upstream region, the stronger runs into the blade passage impinging the boundary layer on blade suction surface; the adverse pressure gradient in the impingement point generates the lambda-shock system and cause the complete separation of the boundary layer, as depicted in figure 37 and largely discussed in section 3.4. Moreover, the high difference in velocity and density achieved between the Mach stem and the lambda legs develops vortex sheets downstream of this bifurcation points. Note that, the particular lambda configuration occurs when the intensity of the oblique passage shock is too high and no regular reflection is possible. Hence, across the two lambda-leg oblique shocks, the corresponding deflection and deceleration become strong: indeed, after the second oblique shock, the flow becomes subsonic (dashed area in figure 38). This huge deceleration, that affects all the passage width, will be soon recovered thanks to the so called *supersonic tongue*; this phenomenon is related to the lambda shock system and develops a region of locally supersonic flow near the edge of the boundary layer; here, as reported in [10], the maximum level of shock losses can be found. Furthermore, the growth of the separate region with the relative re-acceleration area is function of the pre-shock Mach number. Once again, becomes clear that the precompression of the flow at the cascade entrance and so the precompression blades plays an extremely important role in loss reduction of a compressor cascade.

Figure 37: Flow structure at strong interaction region [10]

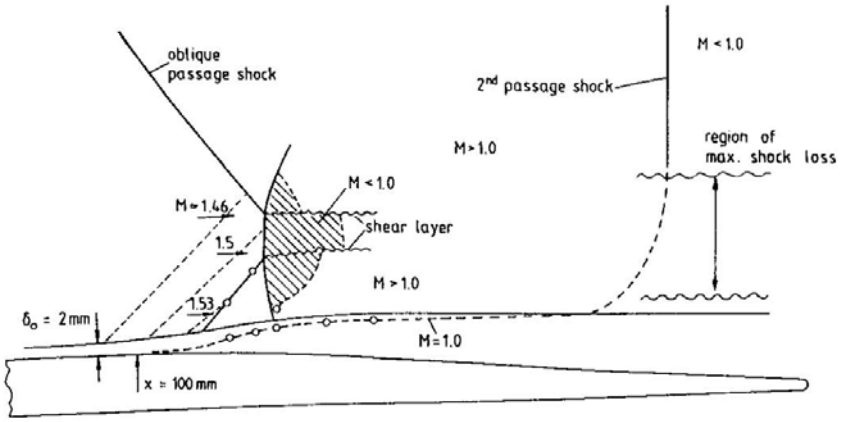

Finally, considering the off-design condition effects on lambda-shape shock systems, a decrease in $AVDR$ values results in a stronger boundary layer separation, a higher shock bifurcation point and so higher losses; on the contrary, increasing that variable allows to shift the shock system upstream into the blade passage with the related losses reduction, as shown in figure 38

Figure 38: Influence of AVDR on shock-waveposition [10]

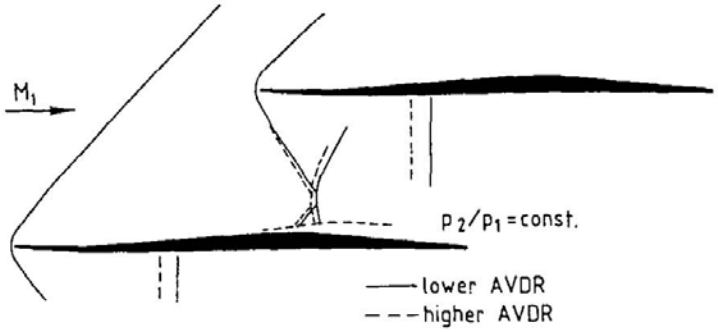

4 Compressor optimization

This chapter presents first general information about optimization analysis and then an VKI in-house optimization software, called CADO, will be briefly discussed (more details will be found in [4],[5]).

4.1 Optimization algorithms

The purpose of optimization analysis is to minimize one or more features of an object[26] in order to improve its performance satisfying design requirements. In particular, starting from one *individual* (or *design vector*) $\overline{\mathbf{x}}$ and changing some chosen characteristic (called *design parameter* x_i), new individuals are obtained. These new individuals should have more "performant" features, i.e. their *function objectives* $f(\overline{\mathbf{x}})$ must have "better" value than the previous one and respect the same *constraint* of their *parents*. Therefore, going through generation, $f(\overline{\mathbf{x}})$ should decrease/increase, according to optimization aims and objective nature. Note that, every optimization algorithm requires a *parametrization* of the real object in order to handle it as a design vector; moreover its *fitness* evaluation needs a time-consuming CAE analysis, as *CFD* one, at least for each new individual.
In the next part the above keyword in italic will be explained to better understand the following optimization techniques:

- **Individual** t: is the subject of optimization and is represented by design variable vector $\overline{\mathbf{x_t}} = (x_{t_1}, x_{t_2}, ..., x_{t_n})$, where x_{t_i} are the design parameters that can be modified (e.g. thickness of a rod, chord length, flow inlet angle, ...). In the next lines "individual", "design" and "candidates" will be used as synonyms even if the first one should be reserved to Evolutionary methods.

- **Function objective** $f(\overline{\mathbf{x}})$: quantity to minimized or maximize such as relative speed of the flow, speed or pressure ratio, efficiency, stall margin, etc etc[27]. If an optimization problem has one objective, it is called *single objective optimization*, otherwise it is named *multiple objective optimization*.

- **Generation**: set of new individuals generated from existing individuals called parents during one single generation step. Therefore new designs are based on previous one, following the next rule:

$$\overline{\mathbf{x}}_{\mathbf{t+1}} = \overline{\mathbf{x}}_{\mathbf{t}} + \alpha_i \cdot \overline{\mathbf{S}}_{\mathbf{i}} \tag{55}$$

  where $\overline{\mathbf{S}}_{\mathbf{i}}$ is the search direction and α_i defines its change amplitude

- **Population**: group of N individuals made through several generation steps.

- **Constraint**: feature to respect in order to be a valid new individual, usually present as an inequality (e.g. $\overline{\mathbf{x}}_{\mathbf{t+1}}$ would be a new design if its value of tensile strength is lower than 1200 MPa)

- **Pareto front**: set or rank of individuals that do not dominate each others in term of two or more objective values, e.g. $f(\overline{\mathbf{x}})$ and $g(\overline{\mathbf{x}})$ in figure 39. This scheme is useful in multi-objective optimizations to evaluate and compare new designs and to reduce population number

- **Evolutionary Algorithm**: zero order method where individuals with higher fitness have more chance to survive and/or get reproduced[28]. In contrast with other methods (for more information see Ref. [4]) EA is population based, requires at each iteration the evaluation of an entire population of designs and it is not deterministic. *Genetic Algorithm* (GA) and *Differential Evolution* (DE) are two of the most popular evolutionary strategy.

[26] e.g. a beam, a blade, an airfoil, ...
[27] note that, in every optimization methods, "fitness" and "objective function" could be used as synonyms, except in EAs where only the latter one makes sense
[28] in agreement with Darwinian evolution theory

Figure 39: Pareto front for a two-objective optimization and relative population ranking.

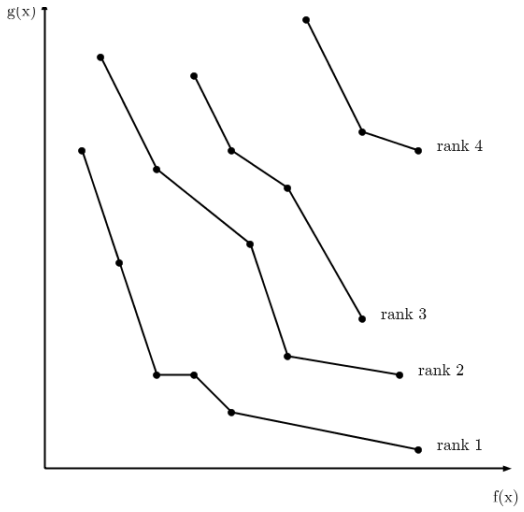

- **Computational Fluid Dynamics** (CFD): accurate tool used to check the performance and the feasibility of the new set of individuals. The analysis result can be stored in *Metamodel* databases in order to perform a better generation loop.
- **Metamodel**: model not based on physical one, but on interpolation of individuals chosen by an higher fidelity method (as a CFD software). Using metamodel in generation loop helps to speed up the optimization process. Featuring higher fidelity evaluation, the method can be self-learning. Artificial Neuronal Network (ANN) and Kriging model are two wide-used metamodel. To reduce even more the time-consumption and address the optimum search in the right direction, an initial "knowledge" is required: *Design Of Experiment* method will fit these requirements.
- **Design of the Experiment** (DOE): first choice of design parameters based on statistical method. It plays a relevant rule in goal reaching.

With the previous definitions in mind, let's now deepen the optimization methods, dividing them into zero, first and second order methods.

4.1.1 Zero order methods

Also known as derivative-free methods, these techniques use only the function values to find the minimum/maximum, not the derivative. There are many types of zero order methods, in the following some of them will be briefly discussed.

Random search A large number of candidates $\overline{\mathbf{x}}$ are randomly chosen and their objective function evaluated: obviously the design with the smallest $f(\overline{\mathbf{x}})$ value will become the optimum. This simple and intuitive method has a big drawback, the large number of individual to be evaluated that increase the optimization time.

Random walk Unlike the previous one, in this method the new design is found from equation 55 with a random perturbation[29] of the previous individual. Moreover, the $\overline{\mathbf{x}}_{\mathbf{t+1}}$ replaces the $\overline{\mathbf{x}}_{\mathbf{t}}$ only when it has no constraint violation and better objective (if the old design constraints are satisfied) or simply less constraint violation (if the old design does no respect the constraints).

Simulated annealing This algorithm, based on the analogy with annealing solid simulation[30], allows to create a new design by randomly changing the previous one. Unlike the Random walk method,

[29] i.e. random choice of $\overline{\mathbf{S}}_{\mathbf{i}}$ and α_i

[30] an annealing process is a physical process where, after reaching a specific temperature, all the particle of a solid randomly move in the liquid phase arranging themselves in the low energy ground state; this phenomena required slow cooling. For more detail see [4]

the old individual replacement probability depends on virtual energy and virtual temperature: the latter one decreases with iteration step and prevent to accept worse $\overline{\mathbf{x}}$, while the remaining is the difference between new and old design performances. Worse individual could be accepted, but only in order to the "escape" from a local minima of the objective function. The big drawback, as before, is the high number of designs required to obtain the optimum individual.

Evolutionary algorithms This set of algorithms is population based and, at each iteration, requires the evaluation of an entire population. Note that EA are not deterministic and the random choice is already used to address the optimization towards the optimum point. Different generation techniques lead to different EA based methods.

Genetic algorithms GA are global search algorithms that use the fittest survivals in order to find the optimum. Here, an individual is represented by a binary string where every design parameter is translated into bits, which number depends on the required accuracy (as shown in figure 40).

Figure 40: Design representation with binary strings.

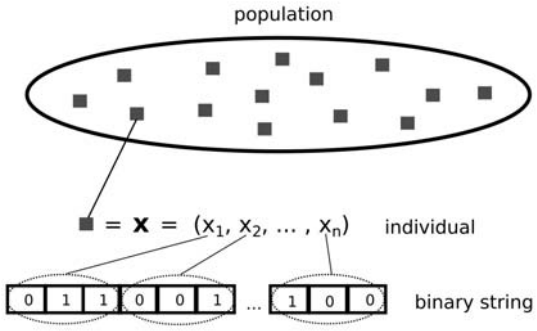

For the reproduction, two individuals, called parents[31], are selected through *tournament selection* or *roulette wheel selection*. In the latter one, the probability of an individual to be chosen is proportional to its fitness[32] and, for this reason, the resulting population is less diversified. On the other hand, in a tournament selection, the best individual from a randomly chosen s-individuals group becomes a parent. As the tournament size s increase, the two selected parents are more similar, while with low value the individuals could be less fit and more diverse[33]. Once found the parents, with *crossover* new individual binary string is made from a piece of the two previously chosen givers bits, as done in figure 42; this, through generation, could lead to individual too similar to each other. At this point *mutation* method will be used in order to randomly change bits. If constrains are considered, to evaluate the performance of an individual the afore used function objective must be replaced by a pseudo objective function:

$$\widetilde{f}(\overline{\mathbf{x}}) \;=\; f(\overline{\mathbf{x}}) \;+\; R \cdot \sum_{j=1}^{m} \delta_j \cdot \left(g_j(\overline{\mathbf{x}}_{\mathbf{t}}) \right)^2 \tag{56}$$

$$\text{where} \begin{cases} \delta_j = 0 & \text{if } g_j(\overline{\mathbf{x}}) \leq 0 \\ \delta_j = 1 & \text{if } g_j(\overline{\mathbf{x}}) > 0 \end{cases}$$

and R, the penalty multiplier, gives the weight to satisfy the constraint $g_j(\overline{\mathbf{x}})$[34]. Another approach,

[31] note that every pair of parents could have two children

[32] or better, taking into account the roulette, higher the individual fitness, the more area on the roulette wheel is given to this design and the higher its chance to be selected

[33] usually a tournament size value about 2 is used; therefore every parent is chosen between only 2 individuals, as in figure 41. In this way, the tournament selection become a very simple and highly effective method

[34] as R value increase, the optimum of $\widetilde{f}(\overline{\mathbf{x}})$ becomes closer to the constrained optimum. Thus R value is a trade off between optimization numerical stability and the degree of constraints satisfaction

called *death penality*, consists in rejecting unfeasible individuals. This method, unfortunately, could lead to informations loss.
Once found the right parents, generated and evaluated new individuals, a comparison results necessary to choose the best design. Considering a single objective analysis, for each individual you can simply compare their $f(\overline{\mathbf{x_t}})$ values. With two or more objective functions, you will handle simultaneously with two or more fitness values per individual. Therefore is possible to treat them as a single-objective function using the weighted sum of objective:

$$F(\overline{\mathbf{x}}_\mathbf{t}) = \sum_{j=1}^{l} \omega_j \cdot f_j(\overline{\mathbf{x}}_\mathbf{t}) \tag{57}$$

where ω_j are the weights given to the j-th objective function. Another technique uses the Pareto front method; the goal is to obtain a population distributed evenly on the front at different rank, where the rank is inversely proportional to the fitness of an individual[35]. The aim is to have, through the generation process, individuals with rank lower as possible.
Finally, note that in GA a new generation is build replacing the previous generation individuals (two parents) by the new ones (two children) maintaining the population size.

Figure 41: Example of tournament selection method.

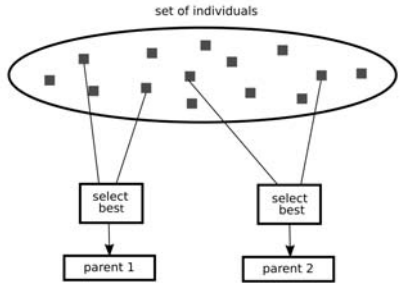

Figure 42: New designs generation through crossover.

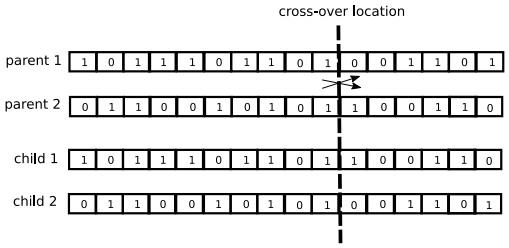

Differential evolution Unlike the previous method, DE does not required the transformation into binary strings and reproduction is made through *replacement*. In particular, starting from an individual $\overline{\mathbf{x}}_\mathbf{t}$, new "trial" candidate is generate in the mutation process:

$$y_i = a_i + F \cdot (b_i - c_i) \qquad i = 1..n \tag{58}$$

where a_i, b_i, c_i are parameters of the relative randomly chosen parameter vectors $\overline{\mathbf{a}}_\mathbf{t}$, $\overline{\mathbf{b}}_\mathbf{t}$, $\overline{\mathbf{c}}_\mathbf{t}$ [36] and F is a user defined constant[37]. At this point, a recombination will perform, obtaining the real candidate:

$$z_i = \begin{cases} y_i & \text{if } r_i \leq C \\ x_i & \text{if } r_i > 0 \end{cases} \qquad i = 1..n \tag{59}$$

where r_i and C help the crossover procedure to prevent similarity between individuals[38]. Note that, as suggested in [6], C values of 0.9 or 1 can be the first choice while, if convergence do not come quickly, $C = 0.1$ is a good start. Finally, after new candidates generation, a fitness evaluation and the eventual replacement of the original vector will perform:

$$\overline{\mathbf{x}}_{\mathbf{t+1}} = \begin{cases} \overline{\mathbf{z}} & \text{if } f(\overline{\mathbf{z}}) \leq f(\overline{\mathbf{x}}_\mathbf{t}) \\ \overline{\mathbf{x}}_\mathbf{t} & \text{if } f(\overline{\mathbf{z}}) > f(\overline{\mathbf{x}}_\mathbf{t}) \end{cases} \tag{60}$$

[35] i.e. the design points along *rank* 1 have the highest fitness and have more chance to be reproduced. See picture 39 too
[36] or better, $\overline{\mathbf{a}}_\mathbf{t} \neq \overline{\mathbf{b}}_\mathbf{t} \neq \overline{\mathbf{c}}_\mathbf{t} \neq \overline{\mathbf{x}}_\mathbf{t}$
[37] usually $F \,\epsilon\,]0, 2[$; its role is to control the amplification of the differential variation between b_i and c_i. As explained in [6], first choice should be $F = 0.5$, while value less than 0.4 and more than 1 works rarely
[38] in particular, r_i is a uniformly distributed random variable $(0 \leq r_i < 1)$ while $C \,\epsilon\,]0, 1[$

Obviously, the latter evaluation and comparison is possible directly only in unconstrained single-objective optimization. Considering the constraints too, the replacement becomes more intricate:

- $\overline{\mathbf{x}}_\mathbf{t}$ satisfies all the constraints: $\overline{\mathbf{z}}$ will replace the previous individual only if the new one matches every constraints too and has a better objective[39]
- $\overline{\mathbf{x}}_\mathbf{t}$ does not satisfy all the constraints: $\overline{\mathbf{z}}$ replaces the original design only if the constraint violations are reduced[40].

In this way, two goals are achieved simultaneously: obtaining a feasible design and improving the individual performance maintaining the feasibility.
Going back to the mutation step (in equation 58), with unconstrained multiple-objectives three different methods are proposed:

- in accordance with Abbas et al. (see [5]), a *non-domination requirements* will be introduced, i.e. $\overline{\mathbf{a}}_\mathbf{t} \neq \overline{\mathbf{b}}_\mathbf{t} \neq \overline{\mathbf{c}}_\mathbf{t}$ must belong to the same rank in the Pareto front. Moreover, new individual $\overline{\mathbf{z}}$ replaces its "parent" $\overline{\mathbf{x}}_\mathbf{t}$ only if it dominates $\overline{\mathbf{a}}_\mathbf{t}$. At this point, a new population are made with individuals that do not dominate each other. Once this set of new design reaches the user defined threshold value, a *distance metric selection* will be made in order to remove too closer individual[41]
- another techniques imposed to *rank* together new and old designs in the Pareto front; each rank is made with non-dominating individual and the rank 1 is given to the first set[42]. The second step consist in reducing the population by an half, restoring the original size[43]; as before, starting from rank 1, a distance metric selection will apply, decreasing the number of individuals and ensuring diversity
- considering again the differential variation in equation 58, Rai et al. ([5]) suggest to choose the vector parameters, $\overline{\mathbf{b}}_\mathbf{t}$ and $\overline{\mathbf{c}}_\mathbf{t}$, close to the original design $\overline{\mathbf{x}}_\mathbf{t}$. Therefore, going on with optimization, the afore mentioned difference becomes smaller and smaller, leading to individuals located near the optimum[44]. This wanted behavior, obviously, is similar to the single-objective one, reducing optimization time and complexity.

Finally, in the constrained multi-objective case, the individual respecting better the constraint is considered to dominate the other one[45]. At this point one of the techniques afore mentioned could be used.
Summing up in few lines what above said, DE:

- is a *stochastic divert search method*, that can handle with non-differentiable, non linear and multimodal cost functions[46]
- allow to run *parallel computation*, so stochastic perturbation of the population vectors can be done separately
- is a *self organizing*, *cost less* and *powerful techniques* that alter the search space by itself using two (or three) individuals near the old one to generate a new design

For these reasons, DE can be considered reasonably one of the best method for optimization process.

[39] i.e. only if $g_j(\overline{\mathbf{z}}) \leq 0\ ,\ j = 1..m\ \wedge\ f(\overline{\mathbf{z}}) \leq f(\overline{\mathbf{x}}_\mathbf{t})$
[40] that is, $\forall j : g_j(\overline{\mathbf{x}}_\mathbf{t}) > 0\,,\ g_j(\overline{\mathbf{z}}) \leq g_j(\overline{\mathbf{x}}_\mathbf{t})\ \wedge\ \forall j : g_j(\overline{\mathbf{x}}_\mathbf{t}) \leq 0\,,\ g_j(\overline{\mathbf{z}}) \leq 0$. Obviously $f(\overline{\mathbf{z}}) \leq f(\overline{\mathbf{x}}_\mathbf{t})$
[41] as crossover, this procedure allows to improve diversity
[42] this procedure will be repeated with the entire population, as shown in figure 39
[43] unlike the previous, in this method, collecting together original and new design, the population doubles
[44] as clear, if the first selected individual objective is too far from the optimum value, the best design search could be trapped in a local minimum of the objective function without chance to escape.
[45] this means that one individual dominates another if all unsatisfied constraint are less or equal in number to the other individual and at least one constraint is better satisfied
[46] i.e. simply, the objective function to minimized/maximized. Note that usually the objective function is the cost function negative

Metamodel assisted DE Metamodels allow to reduce the total computation cost, using an interpolation of already analyzed individuals with an high fidelity tools (e.g. CFD softwares)[47]. For better understand the difference between this two methods, without considering the time consumption, see figure 43: here the continuos line shows the objective function $f(\overline{\mathbf{x}})$ real trend, trend that should be found through optimization. Furthermore, a "database sample" can be known design or simply new optimized individual, both tested with a CFD tool. On the other hand, dashed curve is made by individuals that are created through an interpolation and which objective function value is the result of a weighted sum[48]. As shown, metamodel predicted design-fitness trend suggests also unfeasible individual and could lead to a relative minimum point (called *predicted optimum* in figure 43), but, thanks to its amount of data and low time-consumption, less and more "fit" individual can be tested further with high fidelity tools addressing the optimization closer to the real optimum with less computations.

Figure 43: Real vs. metamodel predicted function objective - design vector relationship.

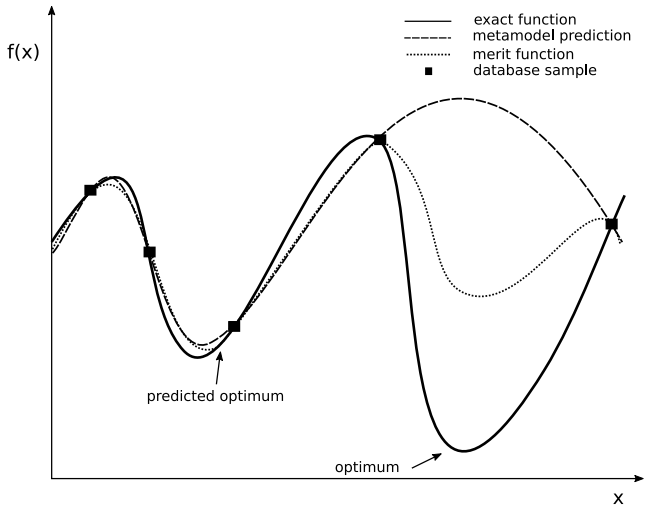

Considering the above mentioned metamodel-CFD relationship, three different ways to link low and high fidelity tool could be found:

- metamodel and CFD are used together during each generation
- CFD simulations are made only at the end of a population generation process on the most promising individuals found by metamodel (called *on-line trained metamodel*). During DE process metamodel training is required
- metamodel is used for several population generation; at a certain point the best individual will be checked with CFD tools and added to the metamodel database. Therefore the self-learning capability is added to the method, that will be referred to as *off-line trained metamodel*).

Considering the mathematical side, in general a metamodel could be represented as a lower computation cost function $\widetilde{f}(\overline{\mathbf{x}})$:

$$\| \widetilde{f}(\overline{\mathbf{x}}) - f(\overline{\mathbf{x}}) \| < \epsilon \tag{61}$$

where $\widetilde{f}(\overline{\mathbf{x}}) : \mathbb{R}^n \mapsto \mathbb{R}^m$, $f(\overline{\mathbf{x}})$ is the already known and high cost performance vector, ϵ is a sufficient small constant and $\|\|$ is a p-norm. Changing the mathematical form of $\widetilde{f}$, different type of metamodel could be found[49]; in particular *Artificial Neuronal Networks* and *Kriging* methods will be

[47] Note that, using interpolation instead of FEM or FVM, metamodels accuracy is very low, as well as its time consumption

[48] obviously the metamodel needs some known designs and their $f(\overline{\mathbf{x}})$ in order to perform the interpolation; the database samples (i.e. DOE) satisfied this requirement. More detail will be given in the next lines and in [4],[5]

[49] or better, each metamodel has different coefficients in $\widetilde{f}(\overline{\mathbf{x}})$

discussed[50]. The first one is simply a simulation of a human brain behavior, where neuron (in your case, the x_n parameters of the design vector) are arrange in layers and contains information that pass from one to another one thanks to parallels connections, as explained in figure 44. Each "passage" is not cost-less and its efficiency is given by a weight, $w_{i,j}^{hidden}$ or $w_{i,j}^{out}$ where *hidden/out* refers to the $j-th$ neuron that stands on a hidden/output layer and it is linked to the $i-th$ neuron[51].

Figure 44: ANN network layout example.

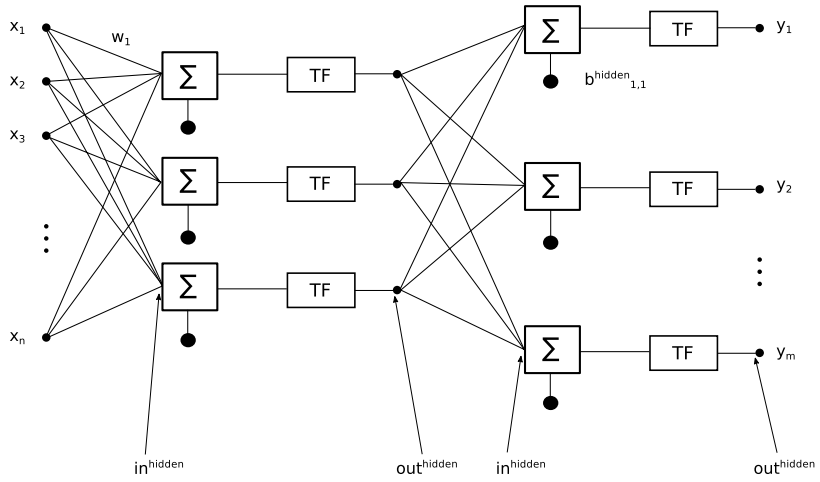

In addiction bias coefficient has to be considered while computing hidden or output layer response, b_j^{hidden} or b_j^{out} respectively. At the end, the output information y_j is given by:

$$y_j \;=\; TF\left(\sum_{i=1}^{h} w_{i,j}^{out}\cdot out_i^{hidden} + b_j^{out}\right) \tag{62}$$

$$\text{with}\;\begin{cases} TF \;=\; out_j^{hidden}\,/\,in_j^{hidden} \;=\; \frac{1}{1+e^{-in_j^{hidden}}} \\ in_j^{hidden} \;=\; \sum_{i=1}^{n} w_{i,j}^{hidden}\cdot x_i + b_j^{hidden} \end{cases} \tag{63}$$

where TF is a sigmoid transfer function, out_i^{hidden} is the output of the connection between the $i-th$ hidden neuron and the $j-th$ output[52]. As above said, connection weight and bias has to be chosen[53] and their value affect severely the objective function search, where $\overline{\mathbf{y}} = f(\overline{\mathbf{x}})$ or better $\overline{\mathbf{y}} = \widetilde{f}(\overline{\mathbf{x}})$. Even the parameter number affects the goal reaching: in particular if n are the input neuron number and m the output one, the hidden layer parameter should be $h = 2n+1$ in order to have a metamodel noise-free and capable to recognize the noise in the data. Thanks to its nature, ANN needs only three layer to better describe the $\widetilde{f}(\overline{\mathbf{x}})$, that is one input layer, one hidden layer and an output one[54].
Considering the second method, i.e. Kriging, it belong to the linear least square algorithms while it reproduces exactly the observe data[55]. Therefore is possible to find immediately the objective function trend:

$$\widetilde{f}(\overline{\mathbf{x}}) \;=\; \sum_{j=1}^{k} \beta_j\, g_j(\overline{\mathbf{x}}) + Z(\overline{\mathbf{x}}) \tag{64}$$

[50] more methods and accurate details could be found in [5]
[51] as in figure, the connection are strictly between neurons in different layers
[52] note that, as better explained in figure 44, the expression in 63 is valid for each output/input; that is, for example $in_j^{out} \;=\; \sum_{i=1}^{h} w_{i,j}^{out}\cdot out_i^{hidden} + b_j^{out}$. The latter one is nothing but the expression in brackets in equation 62. Moreover, $out_j^{out} \;=\; y_j$ and TF used in equation 62 is simply gives by $out_j^{out}\,/\,in_j^{out}$, as obvious
[53] iterative error back-propagation method with know inputs and outputs is used for this aim
[54] better known as Kolmogorovs Theorem, valid for any continuos function from $\mathbb{R}^n$ to $\mathbb{R}^m$
[55] that means, the right member in equation 61 becomes equal to 0, or better $\widetilde{f}(\overline{\mathbf{x}}) \;=\; f(\overline{\mathbf{x}})$.

where g_j is a regression function, β_j could be a constant and $Z(\overline{\mathbf{x}})$ is a model of a Gaussian and stationary random process with zero meaning. The previous parameter and function, can be found considering $\widetilde{f}(\overline{\mathbf{x}})$ as the best linear unbiased predictor, that means a linear combination of the observation sample:

$$\widetilde{f}(\overline{\mathbf{x}}) \;=\; \sum_{i=1}^{N} w_i(\overline{\mathbf{x}}) \cdot f(\overline{\mathbf{x}}) \qquad with \quad \begin{cases} E\left[\widetilde{f}(\overline{\mathbf{x}}) \;-\; f(\overline{\mathbf{x}})\right] = 0 \\ MSE = E\left[\left(\widetilde{f}(\overline{\mathbf{x}}) \;-\; f(\overline{\mathbf{x}})\right)^2\right] \end{cases} \tag{65}$$

where E, the mean error, must be equal to zero to satisfy the unbiasedness constraint and MSE, mean square error, could be minimized and used as the best linear unbiased predictor. Hence, with the Kriging method, the predicted objective function value and an estimation on the prediction error are given. This feature is obviously an advantage, but, sometimes, an high uncertainty can hide an individual not as bad as predicted. For this reason, a parallel evaluation process can be used, in order to check the uncertain designs with an high fidelity tool and increase the database knowledge. Another way consists in minimizing the following:

$$m(\overline{\mathbf{x}}) = \widetilde{f}(\overline{\mathbf{x}}) - \rho \cdot p\,(\overline{\mathbf{x}}) \tag{66}$$

where m is called the *merit function*, $p\,(\overline{\mathbf{x}})$ is the uncertainty of the prediction, ρ is a weight and its value is positive. Note that with kriging model the uncertainty is known. The advantage of using the merit function is shown in figure 43: m can help to avoid objective function local minima and guide the optimization towards the absolute minimum (i.e. optimum point). Considering ρ, it should decrease through the iteration: high value means giving more knowledge of the objective (first iterations) while low value leads the search to the optimum point.
Finally, the ANN metamodel can be used to accelerate the optimization but, when more accuracy is required (e.g. in constraints prediction), kriging method is preferred.
More metamodel examples, such as RSM or RBF, can be find in [5].

4.1.2 Upper order methods

When a derivative is required, zero order methods can not be used in $f(\overline{\mathbf{x}})$ minimum pursuit. Here, first and second order techniques are briefly reported; for more details see [4].

First order In first order method the new design search is moved where the objective function decrease becomes more intense. Hence, the search direction $\overline{\mathbf{S}}_i$ in equation 55 can be found as follow:

$$\overline{\mathbf{S}}_i = -\,\Delta f(\overline{\mathbf{x}}_i) \tag{67}$$

while the amplitude α_i is chosen small enough to avoid function objective overshooting and can be evaluated minimizing the 1D function $f(\overline{\mathbf{x}}_\mathbf{i} + \alpha_i \cdot \overline{\mathbf{S}}_\mathbf{i})$. Considering again $\overline{\mathbf{S}}_i$, another method, called *conjugate directions method* is based on the principle of the steepest descend method, where the last iteration helps to guide the search towards the minimum:

$$\overline{\mathbf{S}}_i = -\,\Delta f(\overline{\mathbf{x}}_i) + \beta_i \cdot S_{i-1} \qquad \text{with} \quad \beta_i = \frac{\left|\Delta f(\overline{\mathbf{x}}_i)\right|^2}{\left|\Delta f(\overline{\mathbf{x}}_{i-1})\right|^2} \tag{68}$$

The previous iteration number in equation 68 can be increased, leading to a more accurate search with second-order methods features[56]. At this point the gradient $\Delta f(\overline{\mathbf{x}}_i)$ must be evaluated; various method can be used, as the *finite difference method*, *complex variable method*, *algorithmic differentation* or *adjoint methods*. More details about the just mentioned gradient evaluation techniques can be found in [4], while the given informations are sufficient for the aim of this work.

[56] for this reason, Davidson-Fletcher-Powell and Broydon-Fletcher-Goldfrab-Shanno methods are called quasi-Newton methods

Second order Second order methods are simply derived from Newton's method and can be consider quasi-Newton schemes. Only one iteration is needed to minimized a quadratic function while $\overline{\mathbf{S}}_i$ and α_i are determined directly, leading immediately to the optimum point. Otherwise, with non-quadratic functions more passages are needed, but the convergence are faster than any other methods. Obviously, due to Newton's method nature, second order techniques are computational expensive and numerically unstable. For these reasons, their are not used in optimization problems that involved a Naiver-Stokes and/or stress computation.

4.2 Choice of optimization parameters

Once chosen the generation model, the object to optimized must be parametrized, or better reduced to a sequence of $\overline{\mathbf{x_t}} = (x_{t_1}, x_{t_2}, ..., x_{t_n})$. Moreover, constraints are imposed on the design parameters x_{t_i} and an initial database should be built using the Design of Experiments (DOE) method. A brief example on optimization of a compressor stage willl be reported in order to .

Parametrization Any optimization method requires the parametrization of the subject that should be improved. For this reason, its charachteristics (thickness of a rod, lenght of the blade chord, etc...) are depicted by several parameters which together makes the design vector $\overline{\mathbf{x_t}}$. Moreover, for each subject feature, a numerical distribution is given through Bézier curve or B-spline curve. The control points of these distributions are simply the related parameters which variation allows the optimizer to find a more fit design vector. As an example, the parametrization of a 3D radial compressor is reported from [21]. First at all, the meriodional shape of the impeller is divided in seven patches, as in figure 46; for each patch a curve is defined at hub (lower surface) and shroud (upper surface) by a Bézier curve which control points (red points in figure 45b) are the coordinates of these curves. Considering the blade (showed in patch number 4), four metal angle β are used as Bèzier points to define the camberlines at hub and shroud. In particular, the β distribution between the meridional plane m and the streamline S are defined by the thrid order polynomials:

$$\beta(s) = \beta_0\, s^3 + 3\,\beta_1\, s^2(1-s) + 3\,\beta_2\, s\,(1-s)^2 + \beta_3\,(1-s)^3 \tag{69}$$

where s is the non dimensional length starting from leading edge ($s = 0$) and ending at trailing edge ($s = 1$). Note that, equation 69 depicted the carbeline in a $\beta - s$ plane; hence, the trasformation into $x - y - z$ coordinates are given through the camberline circumferential position θ (see figure 45b). The blade camberline shape, as showed in figure 46b, are now controlled by four β so the camberline of the entire blade is parametrized with eight Bézier point (four at hub and four at shroud). In addition, is possible to define the trailing edge (rake) or leading edge (lean) position with respect to the hub camberline without affecting the shroud camberline distribution; using the rake as a parameter allow to define a larger radius resulting in a smaller sensitivity. At this point, becomes necessary to define the blade thickness at hub and shroud; usually it is given by a parabolic distribution in which a Bézier point can be used to specify the radius of curvature at leading edge; furthermore all the thickness distribution coordinates can be considered as optimization parameters or can be kept constant. Finally, even the number of blades could be parametrized and changed during the optimization process.

Figure 45: Definition of (a) the meridional contour at hub and shroud and (b) the camberline by beta distribution [21]

(a) (b)

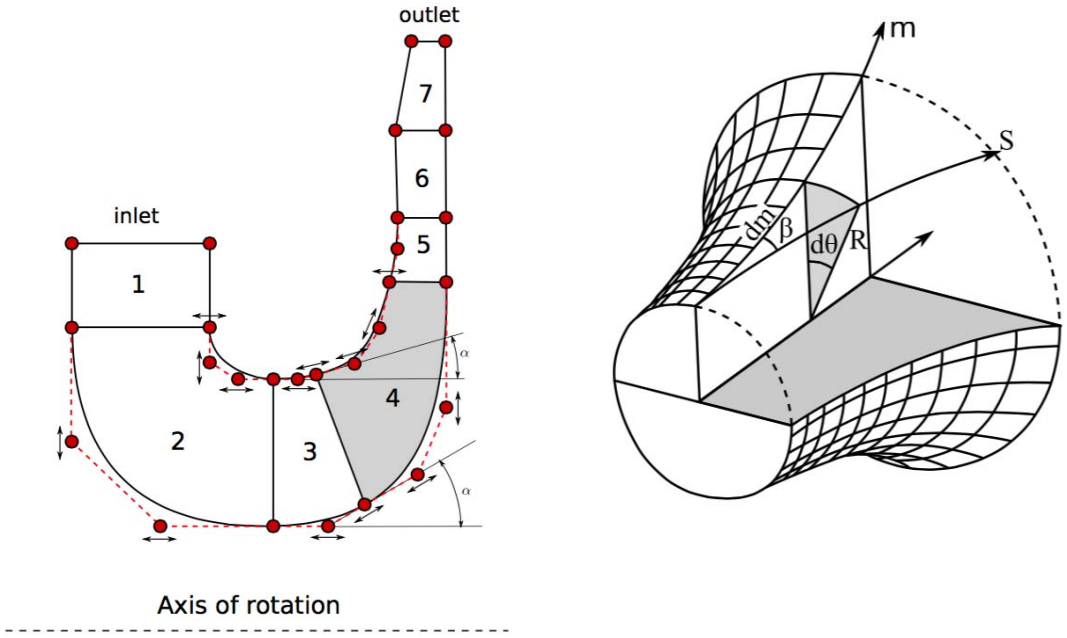

Figure 46: Parametrization of (a) the suction side and (b) the camberline by beta distribution [21]

(a) (b)

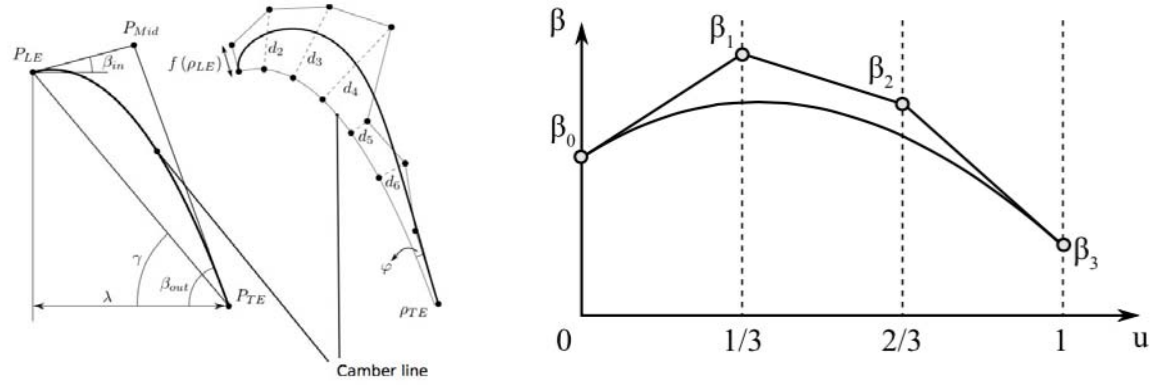

Constraint Constraints help to choose the feasible designs through the replacement teqniques (see equation 60). Therefore, in single-objective optimization, the rule reported in section 4.1.1 and in [5], replaces a design which had constraints violation by a design which reduces the amount of constraint violations. In this way, the highest priority is given to achieve a feasible and improved design. For multi-objective, if the two analyzed individuals do not satisfied the constraint, the dominance is checked for the constraints, i.e. one individual dominates another if all unsatisfied constraint are less or equal to the other individual and at least one constraint is better satisfied. Moreover, the individual that respects the constraint is consider to dominate the other which does not satisfied that constraint. As an example, on a blade parametrization, the designs with a average thickness less then a specified value will be discard.

DOE The DOE method is developed to create the initial database which will be used to address the metamodel in the optimum search. This technique considers that each of the k design variables can take two values, fixed at 25% and 75% of the maximum design range; the maximum amount

of experiments needed is given by 2^k, i.e. the number of any possible combination of the design variables. To reduce the number of the required evaluation, the so-called *fractional design approach* can be used; this method allow to consider 2^{k-p} experiments with p taken such $k-p=a$. Note that, in this work the a value is chosen as 5.
Other methods can be used to generate the first database, such as a creation of random samples. Obviously the DOE should be preferred when dealing with multi-objective and multi-constraint optimization or when the number of optimization parameters is high.

4.3 CADO software

The Computer Aided Design and Optimization toll (CADO) was developed at the Von Karman Institute for Fluid Dynamics with the purpose to have a complete and adjustable turbo machinery optimizer. The main components are a Computer Aided Graphical Design (CAGD) library for the automated generation of blades, an automatic mesh generation toll for both the fluid and solid domain, a Computational Solid Mechanics (CSM) and Computational Fluid Dynamics (CFD) codes and a metamodel assisted evolutionary algorithm. The correlation between these component, depicted in figure 47, is very important for a positive outcome, so further clarification are needed. As concern the inner loop (the generation loop), a metamodel assisted DE algorithm guarantees the generation of new feasible designs which feasibility are check through the metamodel knowhow; this knowhow, fundamental for addressing the search in the right direction, simply comes from the database. This database, that "stand" inside the iteration loop, is created usign a DOE method or with random samples while it is kept updated by the high fidelity tools. The latter, the CFD software, checks the designs which come from the generation loop validating or not the metamodel ability. In the negative case, the CFD response is stored into the database in order to adjust the metamodel search. As reported in section 4.1.1, the number of design checked by the high fidelity tools can be varied, choosing between lower computational cost but lower precision and higher accuracy but higher computational time. Considering the metamodel, CADO allows to use several methods, as ANN and Kriging model. Obviously, before starting any loop, the parametrization must be done, choosing the geometrical parameters and constants as done in section 4.2. Finally, one of the major benefits of this software is the possibility to use different CFD, CSM and pre-processing softwares in combination with the CADO optimization tool, as done in this work.

Figure 47: Optimization process flowchart.

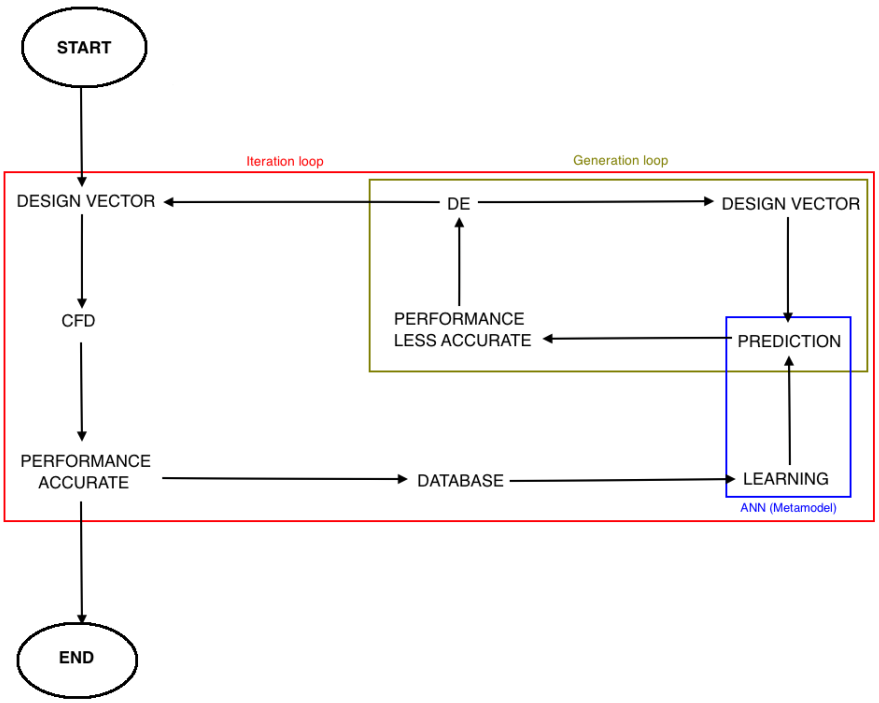

5 Method

The target of this work, i.e. the most performant blade attainment, is achieved not with one single process, but thanks to the combination of several process performed by different softwares. Five softwares are matched together, anyone with a different task: starting from the optimizer, the VKI's in-house software CADO generates several new blades that fulfill the chosen requirements; its outputs, data-file containing geometrical coordinates, will be loaded in IGG^{TM}, a Numeca's software capable to create cascade flow field using the input blade geometry. Then, the mesh is built thanks to an hexahedral grid generator called Autogrid5^{TM}, another Numeca's software. The mesh files, the geometry files and configuration files containing the simulation setup, will be loaded in a VKI's in-house CFD software. All the previous passages, once compiled the setup files for each software (this should be made only one time for the entire optimization process), are completely automatic and self-sustaining, with no need to human aid. Finally, only the simulation result files of the best design, the baseline design and few other individuals are analyzed with the post-processing software called Techplot 360^{TM}. This last operation is partially automatic: macro-files can be loaded in order to make the software to plot the chosen flow variables and cascade features, otherwise the user had to understand and interpret the outputs. Therefore, for a successful result, the setup of each software must be done carefully. For this reason, in the following lines, each component will be introduced briefly and its configuration will be reported.

5.1 CADO setup

First at all, the optimization software requires a blade parametrization, or better the parametrization of meridional contour, camberline, suction and pressure surfaces and thickness. For the latter, the $x - y$ coordinates of eleven points are given, which in turn define the distance between between suction and pressure side normal to the camberline. Suction and pressure side do not require further parametrization, since their distribution follows from the thickness. For the meridional contour, only the blade patch is taken into account, without considering the whole flow path; hence, the four couple of $x - y$ coordinates are given, specifying the limits of the hub and shroud meridional contour. All the previous parameters will not change during the optimization, therefore all the optimized blade have the same thickness and surface distribution of the baseline, as well as identical hub and shroud meridional shape. Furthermore, the camberline is defined as the metal angle β distribution along line in five points ($x - \beta$ coordinates), which are the Bezier control point. The first five points will be chosen using the baseline β distribution; suddenly, for each point, a β range will be given, allowing the optimizer to vary the metal angle distribution but maintaining the same x-coordinate, as shown in table 1. In figure 48, the β value change are depicted in function of the position along the chord, or better the x/c ratio. Note that the best design β_5 point is equal to the lower limit value: this could prevent the optimizer to generate a more performant individual with a lower β_5 since the camberline are the only design parameter that can be modify by *CADO*.

Table 1: Range of five β points defining the camberline metal angle distribution

	β_1	β_2	β_3	β_4	β_5
$\%c$	0.0	1.95	2.69	5.05	1
Lower limit [°]	−48.0	−57.0	−59.0	−56.0	−57.0
Upper limit [°]	−52.0	−61.0	−62.0	−61.0	−60.0
Baseline [°]	−50.0	−58.0	−61.0	−60.0	−58.0
Best design [°]	−51.0	−60.0	−61.0	−60.0	−57.0

Figure 48: Metal angle distribution as function of chord percentage $\%c$

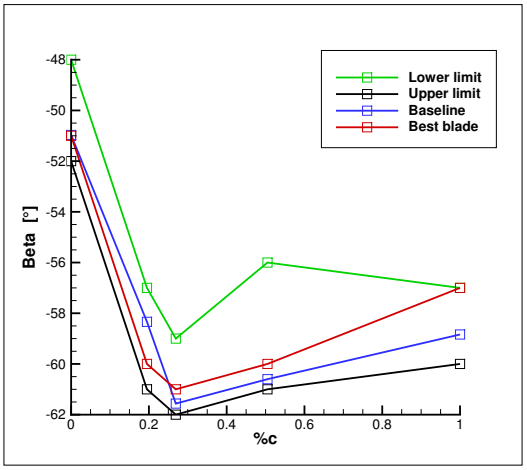

Once the blade is parametrized, the optimizer requires the optimization parameters, i.e. the objective functions, the performance parameters and the constraints, necessary to address the optimum search in the desired direction (more details in chapter 4). The chosen optimization parameter is the entropy change coefficient Δ_s, evaluated as the difference between the inlet and outlet cascade entropy values; obviously, between all the generated individuals, CADO will maintain the ones with the lower δ_s value, i.e. the more performant blades in terms of loss reduction. Moreover, three different performance parameters are used, since each blade is optimized for three different inlet flow angle. Thereby, the optimizer evaluates three objective function per individual, one for each performance parameter (i.e. the optimization becomes multi-objective). Finally, the individuals with a exit flow angle β_2 bigger than $-61°$ will not be consider as reliable candidates; this means that for the i-th performance parameter of each individual (i.e. the i-th inlet flow angle) the following inequality must be respected:

$$\Delta\beta_i = -\beta_{2i} - 61° > 0 \qquad \text{with} \quad i = 1 \text{ or } 2 \text{ or } 3 \tag{70}$$

As shown in equations 70, the constraint is imposed only to one inlet flow angle, i.e. $\alpha_2 = -64.2557°$ per each blade, otherwise the performances comparison would be not reliable. Moreover, the choice of the limit value (i.e. $-61°$) follows from the low flow turning requirements. Finally, note that using the metal angle as parametrization method helps to directly check and control the flow turning (locally and globally) simply reducing or increasing the β range in table 1.
In order to speed up the optimum search, an initial sampling of the database should be perform through the DOE. Contrariwise, in this case, the initial database was generated using 80 random individuals. Obviously this method can affect negatively the entire optimization process but, thanks to the simple optimization setup that choice do not compromise the positive outcome of this work.
As regard the DE setup, the number of evaluation in the iteration loop is 1000 while for the generation loop are required 100 calculations (see figure 47), the size of the population is 40 and the cross-over and mutation parameters are respectively $C = 0.8$ and $F = 0.6$ (see the DE section in chapter 4). These means that 1000 generations will be created with a constant population size of 40 individual (except for the first, in which 80 random designs are generated). Moreover, for sake of simplicity and due to the "trial" nature of this work, the high fidelity tool (CFD software) is used to check the performances for each individual at the end of any population generation and the optimum search was stopped once reached the 8-th generation.

5.2 Flow field setup

The blade shape in figure 49 is taken as baseline and further improvements in term of losses and camberline curvature are based on this blade; in particular, the chord length is $0.4271m$, the camber at inlet is about $\beta = 50°$, the design inlet Mach number is $M_1 = 1.3$ while the design inlet flow angle is $\alpha = -64.2557°$. Unfortunately, no more information can be disclosed, since the baseline is the rotor blade of a supersonic compressor in one of the VKI facilities used for commercial purpose. Hence, starting with the baseline shape in figure 49, the IGG^{TM} software allows to built the 3D flow field in figure 50, splitting

Figure 49: Blade shape used as baseline

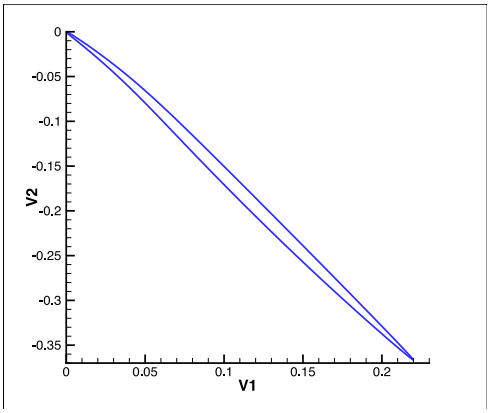

the entire field in five parts: (1) inlet, (2) upper half side of the cascade passage, (3) boundary layer, (4) blade, (5) lower half side of the cascade passage and (6) outlet. This partition allow to put the desire boundary conditions and take into account the periodicity of the flow; indeed, considering the upper side of section (1) as "*mirror*", the flow just above this side is supposed to behave as the flow just below; for the same reason, the "mirror" boundary condition will be assigned to the remaining outer surfaces in figure 50. Obviously, the blade sides are treated as "*wall*" boundaries. Furthermore, in this stage, the cascade size is set for all the further CFD analysis while the blade shape and the remaining flow field geometrical parameters are updated at each iteration; as example of fixed parameters, the blade chord length is $0.4271m$ while the distance between each blade (called *pitch*) is $0.31072m$.

Figure 50: 3D-cascade flow field with one blade

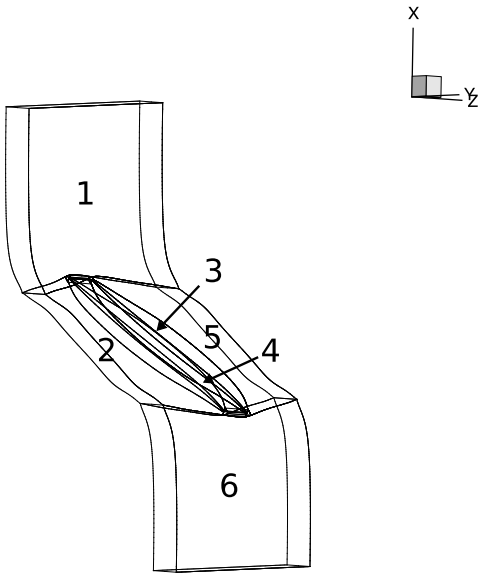

Figure 51: 2D-cascade flow field with two blades

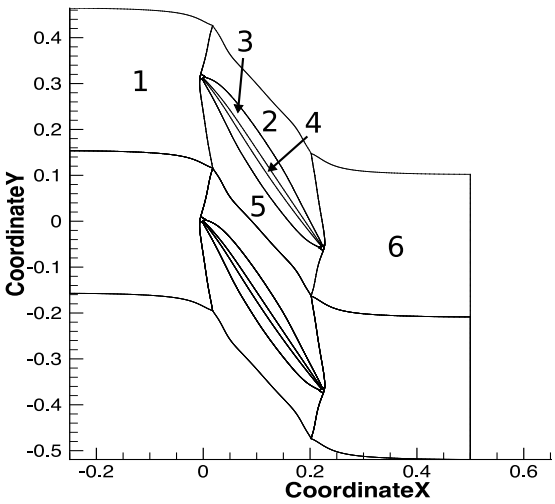

Note that, the two blades-configuration (built juxtaposing two slices cut from the 3D flow field in figure 50) is used only in the post-processing step; the CFD software simulated the flow behavior only around one blade, reducing the computational time and cost (see figure 51).

5.3 Grid setup

Once the flow field is mapped, the discretization of the 2D cascade is required in order to evaluate the flow property. For this reason, at first, an hexahedral structured grid is generated using

the automatic setup of Autogrid5^{TM} (named "mesh 1" in table 2); then, the mesh quality is improved increasing manually the number of grid points and reducing the cell skewness near trailing edge and outlet (as shown in table 2). Furthermore, a CFD simulation is running, testing the seven meshes and evaluating the trend of pressure loss coefficient Y_p (chosen as an example) during the simulation; as depicted in figure 52, the converge of the Y_p occurs around mesh 6 and 7, i.e. since the second last setup, the flow parameters becomes independent from the mesh features. Otherwise, due to the high computational time and cost related to the last two meshes, the third grid setup seems to be the best compromise between computational cost and flow accuracy; therefore it will be used in the following CFD simulation. Figure 53 reports more details about the chosen mesh. As regards the quality parameters in table 2, some more details should be given: starting from the *skewness angle*, its maximum and desired value is 90° (square cells); the *aspect ratio* is evaluated as the ratio between the longest and the shortest side of a cell, therefore its minimum is 1; finally, the *expansion ratio* measures size variations between two adjacent cells and the unity means no differential deformation between the two elements.
Another important grid feature is the ability to depict the flow behavior inside the blade boundary layer. For this reason, the first line of cells along the blade surface should lie inside the boundary layer. That distance y, in CFD analysis, is referred to the *non-dimensional wall distance* Y^+ and can be evaluated using the flat-plate boundary layer theory in equation 71 (more details in chapter 18 of [9]):

$$y = \frac{\nu Y^+}{u_\tau} \tag{71}$$

where ν is the kinematic viscosity, u_τ is the friction velocity and Y^+ get unitary value inside the boundary layer (i.e. the desired position). Hence, with the flow condition related to this work, the height of the first element near the blade surface should be $y = 0.2127567 \cdot 10^{-5} m$; this requirements is entirely satisfied by all the meshes reported in table 2.

Table 2: Mesh skewness angle, aspect ratio and expansion ratio at different grid points

Mesh	Grid points	Skewness (minimum) [°]	Aspect ratio (maximum)	Expansion ratio (maximum)
1	40209	25.178	12495.0	4.3178
2	72681	27.591	24426.0	3.2348
3	89421	29.741	24497.0	3.1628
4	117141	25.586	24799.0	2.9263
5	169281	21.051	24813.0	2.8292
6	181749	21.876	24929.0	2.7917
7	194193	21.373	24616.0	2.7431

Figure 52: Mesh convergence

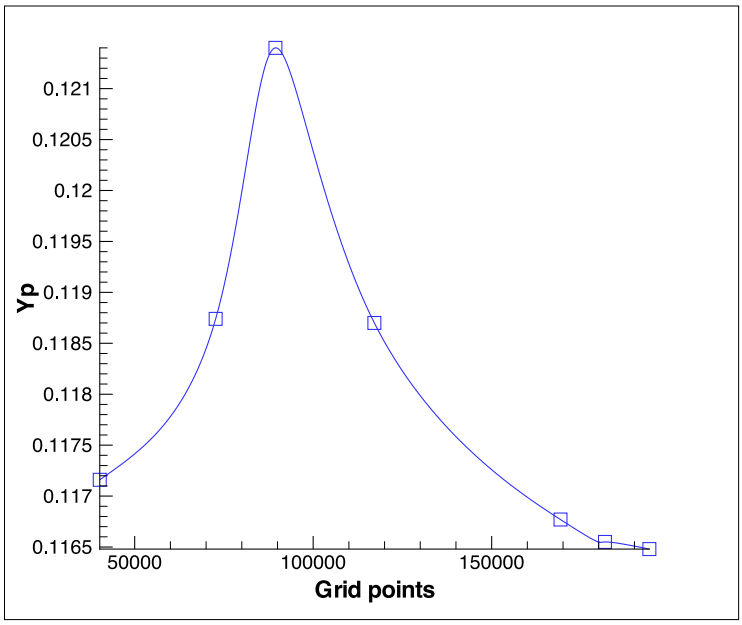

Figure 53: Main features of the mesh used in the CFD analysis (mesh 3)

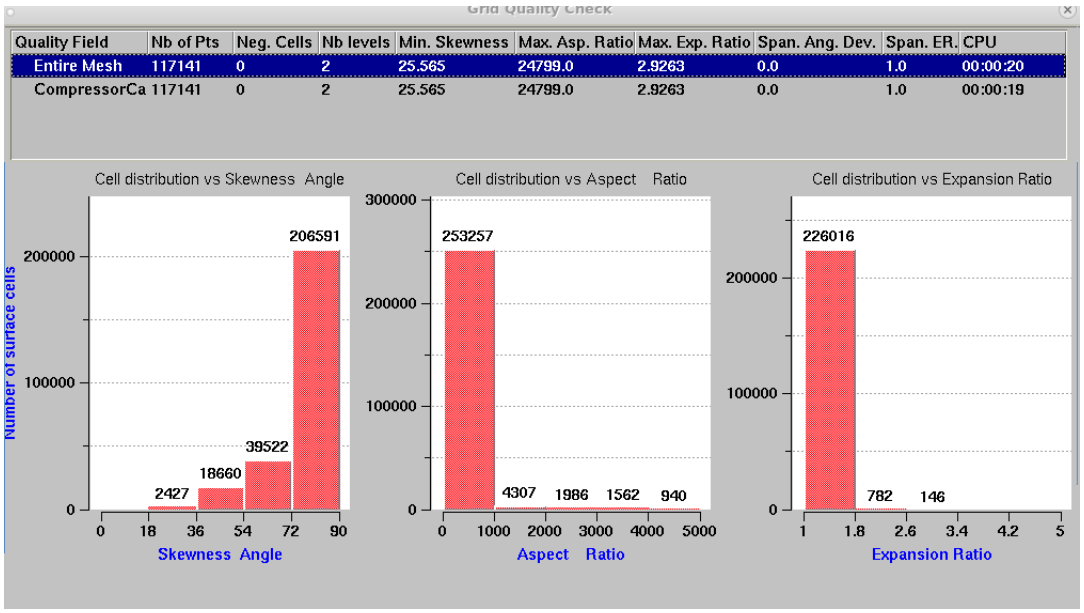

5.4 CFD simulation setup

The CFD software setup is the more error sensitive configuration, since a wrong parameter would affect not only the flow simulation but also the following new population. For this reason, several tests were made to validate the final setup, even with another CFD software. At the end, the chosen inlet flow model was the *turbolent* type, with a *reference lenght* of $0.43m$, a *reference pressure* of $100000Pa$ and a *reference temperature* of $300°C$. The *Spalart-Allmaras* model is used to pattern the turbulence, with the related boundary condition at inlet, i.e. $\chi = \widetilde{\nu}/\nu = 0.1$. The remaining boundary condition on velocity and pressure are reported in tables 3 and 4; in particular, the first depends on the inlet flow angle, hence three different speed value must be specified since the optimizer works with three inlet angle $\alpha_1 = -63.2557°$, $\alpha_2 = -64.2557°$ and $\alpha_3 = -65.2557°$ (i.e. the performance parameters); the angle negative value is necessary to achieve low losses, increasing off-design stability and flow velocity on suction side (more details in section 3.1). Note that all the

CFD simulations are done with the same inlet Mach number and outlet static pressure as well as the inlet static pressure. The initial solution is *constant*, with the variable values showed in table 5; here, the blade is kept fixed ($RPM = 0.0$), since it is considered as a stator blade. Considering the spatial discretization, the second order *Roe* discretization scheme is implemented, while the *GMRES linear solver* is used to perform the *implicit* spatial discretization. Moreover, for the latter scheme, the maximum iteration number is 50 while the *CFL* vary following a *ramp model* between 1 and 10 with 200 iterations. Finally, the fluid is treated as a perfect gas with the usual constants ($k = 1.4$, $\overline{R} = 287 J/(kgK)$). Furthermore the simulation starts with 600 *robust iterations* and stops at 5000 iterations or when one between the density and mass flow *convergence criteria* is satisfied ($2.0 \cdot 10^{-6}$ for both). In addition, the 3D cascade in figure 50 is used as flow field, hence the flow can move even in the z-direction.
The software outputs at the end of every blade simulation, i.e. a file for each inlet flow angle, contains the flow properties at inlet and outlet of the cascade which the optimizer used to understand the reliability and performance ranking of that blade evaluating the entropy change, the metal angle, ...

Table 3: Boundary condition at cascade inlet and outlet

	Static pressure $[Pa]$ p	Total pressure $[Pa]$ p_0	Total temperature $[°C]$ T_0	Mach number $[\ ]$ M
Inlet	\	10000	300	1.3
Outlet	60404.601	\	\	\

Table 4: Inlet flow velocity at different inlet flow angle

Inlet flow angle α $[°]$	Inlet flow velocity ratio $[\ ]$		
	v_x/v	v_y/v	v_z/v
-63.2557	-0.4500096	-0.8930237	0
-64.2557	-0.4343556	-0.9007414	0
-65.2557	-0.4185694	-0.9079655	0

Table 5: Initial constant flow solution

Static pressure $[Pa]$ p	Static temperature $[°C]$ T	Flow velocity $[m/s]$			Spalart-Allmaras costant $[\ ]$ χ
		v_x	v_y	v_z	
30000	220	150	-250	0	0.1

In conclusion, the major benefit with the chosen softwares is the complete adaptability of each setup file to the different geometry. The optimization loop is therefore automatic and will stop only if an error occurs or when the maximum computational time is reached (in this case it was set to 90 hours). Obviously the entire process was performed in a cluster, using 8 cores for any of the required 5 nodes (in this way, the 40 individual of each population are computed at the same time in different "part" of the cluster). Note that, the computational time to generate and test 460 designs (seven population with 40 individuals and one with 80 designs) is high, about one week, due to generation-iteration loop ratio, grid features and the chosen discretization parameters.

5.5 Post-processing setup

The analysis of results is done on a thin slice along the $x - y$ plane of the original 3D flow field. This is possible since the z-component of the inlet velocity is zero and the flow field is takes as homogeneous. In general, the inlet and outlet value of each variable are evaluated respectively along the line 1 and 2 in figure 54. The total pressure gradient ω is calculated in 80 point along the vertical line 2 in figure 54, while the loss coefficient ΔS is the average of Δs values in equation 3:

$$\Delta S = \frac{\Delta s}{s_{ref}} = \frac{s_2 - s_1}{s_{ref}} \tag{72}$$

where $s_{ref} = 120540 Pa/(kg/m^3)$ is the entropy taken as reference value. Moreover, the isentropic Mach number trend is depicted evaluating the M_{iso} in equation 2 along the blade pressure side and suction side, not considering the boundary layer and so the no-slip condition at wall. Finally, the 3D Pareto front in figure 69 is plotted interpolating the ΔS values and meshing the related planes through two Matlab® function (called respectively *TriScatteredInterp* and *surfc*). The remaining variables and contour types are simply the Techplot^{TM} defaults variables.

Figure 54: 2D-cascade flow field used for post-processing analysis

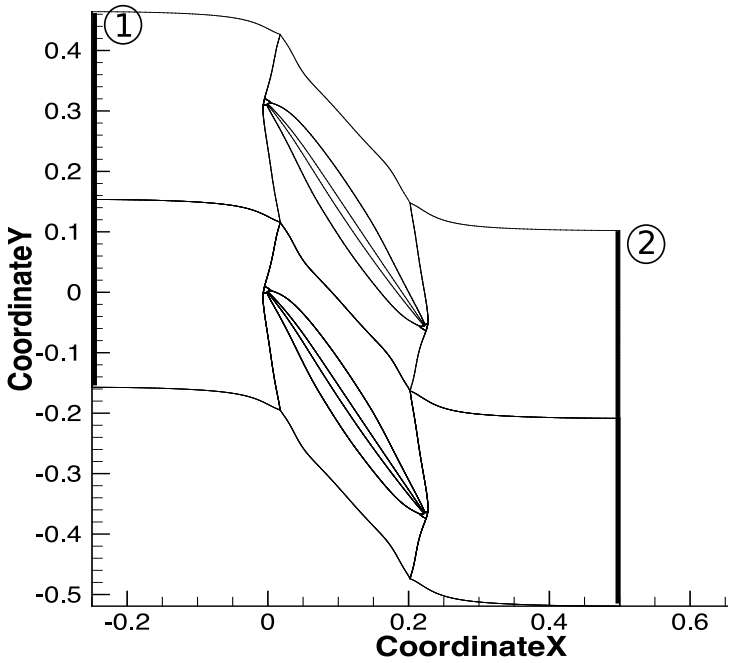

6 Results

This section reports the analysis of multi-objective optimization, proposing the main difference between baseline and best blade, focusing on shape improvements and on flow behavior changes. Moreover, about the latter, the fluid-blade interactions are first analyzed at one inlet angle while suddenly all the three angles are taken into account maintaining constant the remaining flow variables. In both cases, only the best individuals per each generation are considered.

Best blade shape Considering the blade shape, through the optimization process the blade camberline increases its curvature at leading edge and trailing edge, assuming a more s-shaped profile, as shown in figure 55; in particular, considering the metal angles (i.e. the camberline slopes) in 1, the increase in the first two point results in a increment in downward flow deviation while the decrease of β_5 makes larger the outlet passage. Similarly, suction and pressure side curvature changes make the blade tip more concave at suction side while the tail goes upward; that difference will affect the leading edge Mach number enhancing flow pre-compression and reducing the trailing edge wakes, i.e. the flow turns less and remains more attached to walls. Figure 56 shows how the profile changes from baseline to last individual; the difference seems very small, but the changes in flow properties are significant. Moreover, the thickness distribution does not change, as imposed in the optimizer setup. Note that, for obvious reasons, the blade shape does not change from single to multi-objective optimization.

Figure 55: Camberline

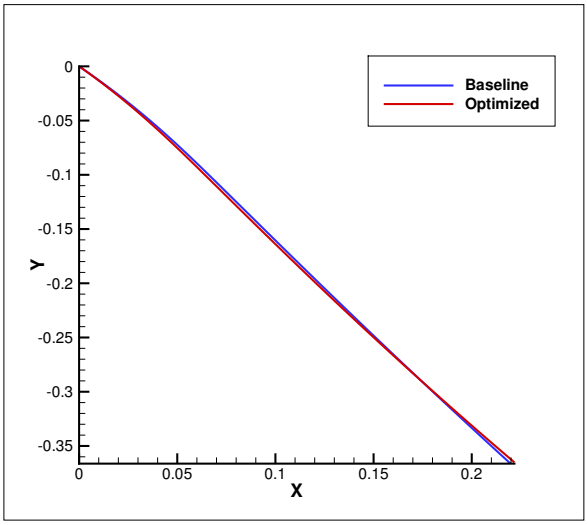

Figure 56: Suction and pressure side

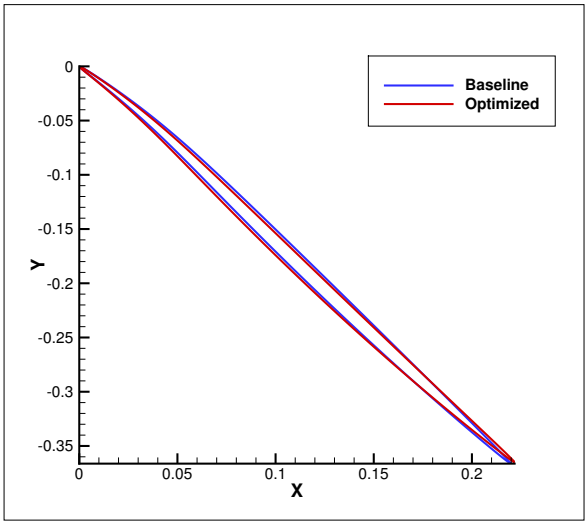

Best blade flow behavior at $\alpha = -64.2557°$ Starting from the performance coefficient ΔS at $\alpha = -64.2557°$, its trend in figure 57 shows the expected loss decrease from baseline to the last best design (40% improvement). Indeed, as reported in chapter 3.4, an increase in inlet flow pre-compression allows to grow the inlet flow pressure, decreasing the Mach number at leading edge and inducing a shock pattern with less losses. This trend does not decrease monotonically, but some peaks develop, also in the last generated design (i.e. the best individual). Obviously, that loss increase is bound to the multi-objective optimum search where the best individual must shows the best compromise between the three function objectives, i.e. between ΔS_1, ΔS_2 and ΔS_3. For this reason, considering the complete entropy behavior even in table 7 or figure 69, a worsening in one design objective could lead to better both the other ones, making that individual eligible as best design. Note, as written before, that little changes in blade shape generate a considerable variation of ΔS.

Figure 57: Static entrophy generation change on baseline and last individual profile at $\alpha = -64.2557°$

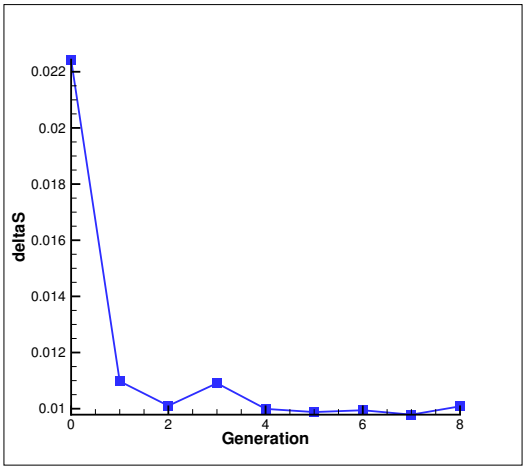

Due to the imposed initial condition (fixed inlet Mach number M_1 and back pressure p_2 reported in tables 3 and 4) and flow field characteristics, the inlet flow independent variables do not change, as shown in table 6. In other words, the inlet static pressure remains constant since it is function of M_1. Moreover, the $AVDR$ value remains constant and equal to one; in first instance this behavior allow to avoid stream tube convergence variation since the mass flow per unit of area should remind the same from inlet to outlet; in second instance, the $AVDR \approx 1$) follows the flow turning requirements in the optimizer setup. For this reason, its very slight increase is probably due to numerical approximation.

Table 6: Inlet flow independent variables at $\alpha = -64.2557°$ for baseline and best individual

$\alpha = -64.2557°$	Baseline	Best individual
M_1 [ ]	1.3	1.3
$AVDR$ [ ]	1.02075	1.06203
p_2/p_1 [ ]	0.59759	0.59759

The constant values of the independent inlet variables from baseline to best blade, obviously, do not mean the flow pattern and losses will remain the same. Indeed, as depicted in figure 58, the variation of blade shape forces Mach number variation inside the blade passage as well as pressure and shocks distribution. Firstly, the bow shock (A in figure 59) becomes more attached to the blade leading edge and the subsonic area between the shock and the tip reduces to a small bubble inside a wider supersonic flow. Indeed, the oblique shock (C) becomes larger and the Mach stem (i.e. the passage normal shock named D) reduces its size. In second instance, as the inlet velocity decreases, the interaction between the "legs" of the lambda-shape shock system (E) and the boundary layer is more severe as well as the flow separation on suction side (F). To complete the flow pattern, near the best blade passage exit, a normal shock occurs (G), turning the flow within the pressure side into subsonic velocity; this shock does not interest the entire width of the blade passage, since the Mach number of the fluid near the suction side become subsonic thanks to the first normal shock (D). Finally, the compression shock (B) developing from the concave suction side, becomes more stronger, decreasing the passage inlet velocity and, in turn, generating the above depicted shock pattern.

Figure 58: Mach number on baseline and best individual.

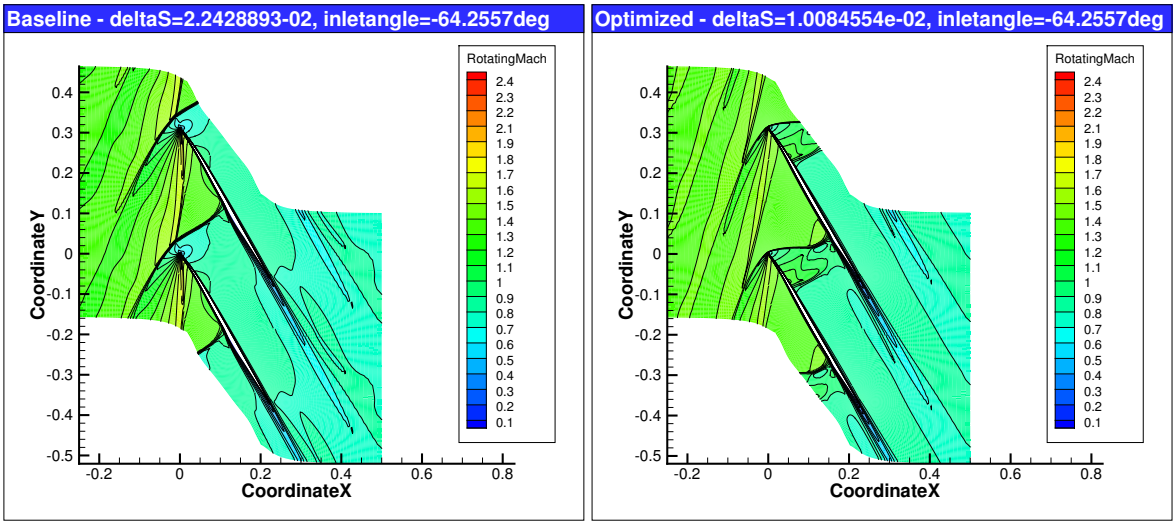

Figure 59: Particular of the shock pattern on (a) baseline and (b) best individual.

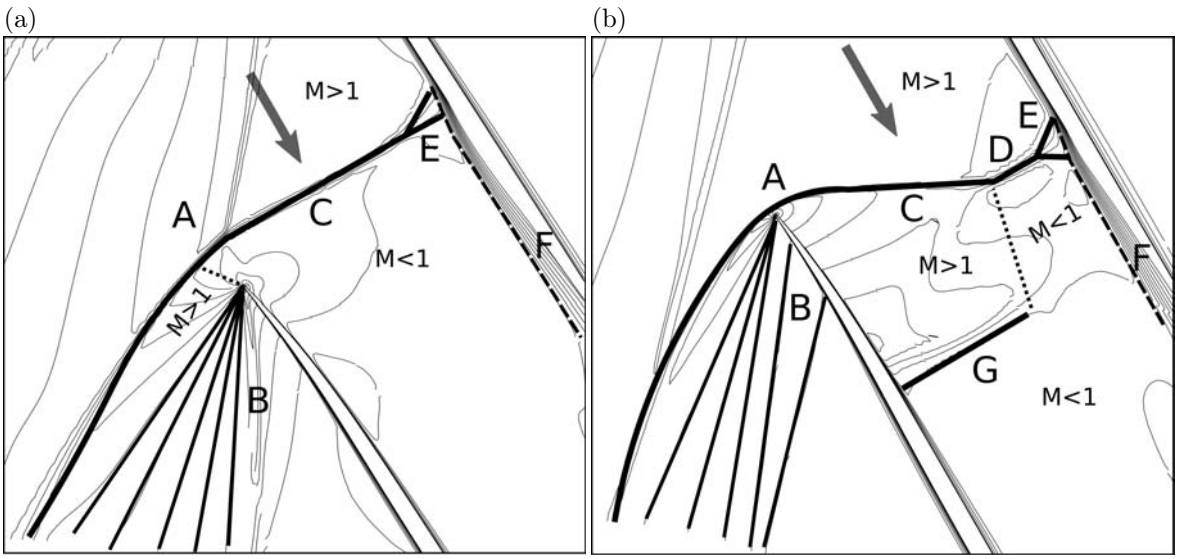

Another result, the most expected one, is the substantial loss reduction: ΔS drops from about $1.8 \cdot 10^{-2}$ to $0.9 \cdot 10^{-2}$. Indeed, as reported in section 3.4, suction side mach number decrease and pressure drop decrease helps to reduce losses leading to the shock pattern described above. Therefore, as better shown in figures 60 and 59b, the best blade supersonic area is wider and affects the first half part of the passage with a subsonic region in the upper part, while on baseline the whole pressure side is subsonic. Clearly, the oblique shock features plays an important role, maintaining the flow supersonic while decreasing the acceleration/deceleration, reducing the energy losses and so keeping the entropy mostly unchanged (unlike what happened within a normal shock, as reported in section 3.2). Note that, in the boundary layer $M < 1$ almost everywhere; nevertheless, a small supersonic area occurs just below the upstream lambda-leg. In addition, the re-acceleration of the flow just upstream of the delta-shape shock, generates a small supersonic bubble inside the subsonic area, barely below the separated boundary layer. These last two remarks confirm again the expected shock pattern depicted in figure 37.

Figure 60: Supersonic and subsonic areas on baseline and best individual.

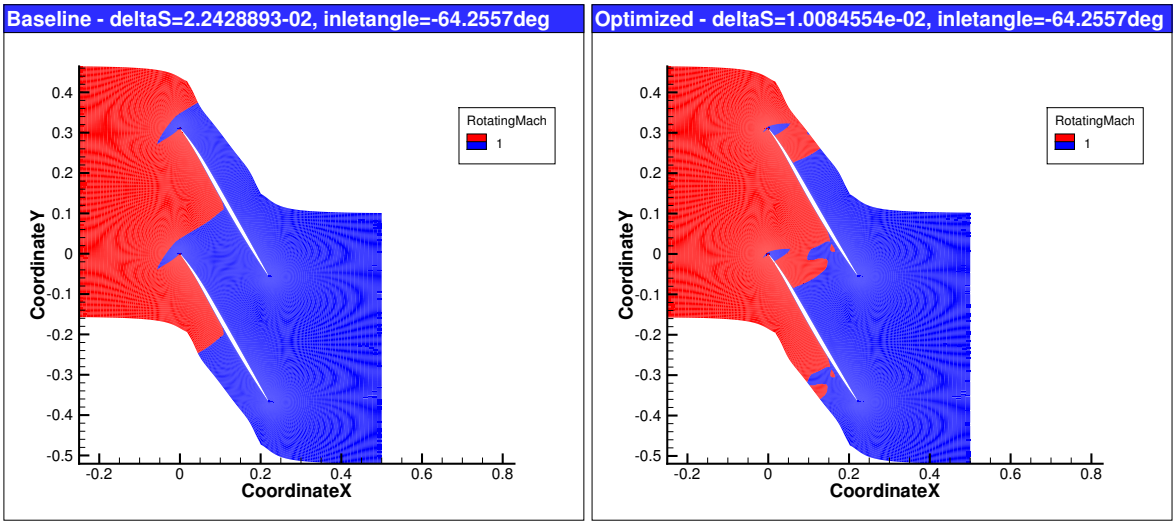

The flow pre-compression, due to the blade shape, reduces the p_0 losses, especially along the suction side boundary layer and streamwise after the trailing edge. Another remarkable effect is the lower value reached at inlet, drop also due to flow adaptation through the oblique shock. Indeed, the flow conditions before and after a normal shock are independent from each other (i.e. without sonic passage, the flow behaves in a "unique way").

Figure 61: Total pressure on baseline and best individual.

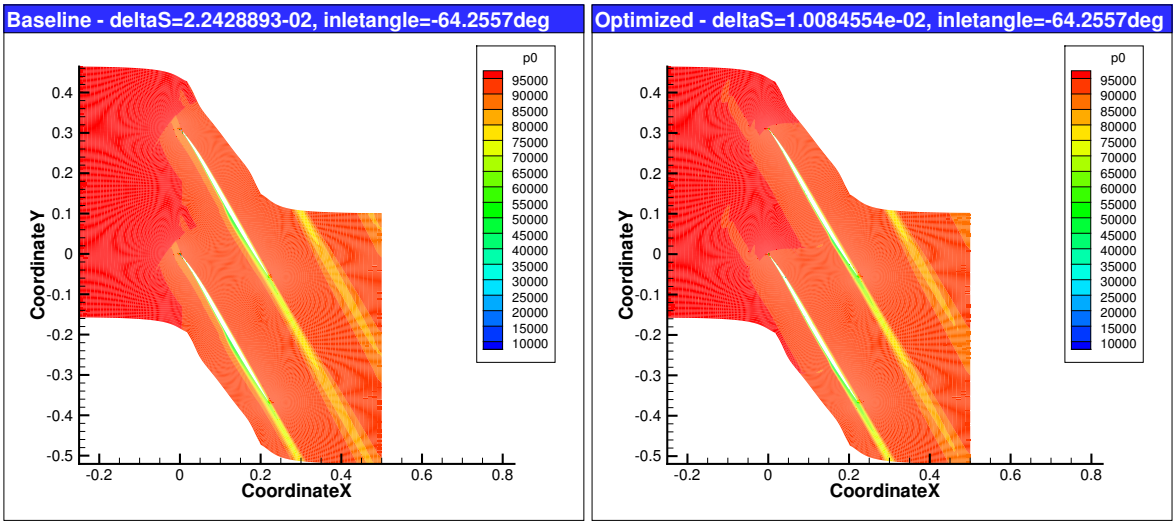

Suction side Mach distribution and shock pattern influence either the vorticity of the flow: from figure 62 is clear that the vorticity growth on suction side due to the delta-shape shock compression ramp (i.e. the increase in boundary layer growth at the shock interaction point) is delayed and the detached flow amount is reduced, as happened with sonic transition and flow speed. This confirms again that the wakes growth is bound with speed, or better with Reynolds number, and its magnitude increases with energy losses.

Figure 62: Vorticity on baseline and best individual.

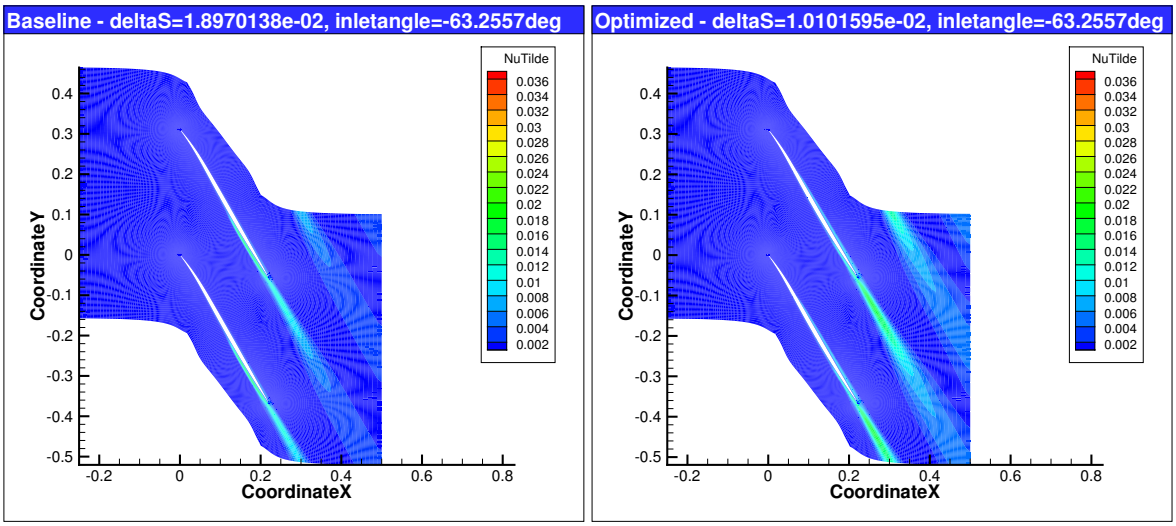

Figure 63 shows how at optimized leading edge the transition from detached to partially attached oblique shock allows the flow to follow the blade shape with less turning, moving the stagnation point backward along the pressure side. In the passage, on baseline suction side, the isospeed lines show several wakes and a severe flow detachment; on the other hand, with optimized blade, the flow remained more attached, the wakes rise is delayed and their size is reduced (see figure 64). At trailing edge, from suction side, streamlines turn into the pressure side area and, only in optimized blade, there are no vortices (as shown in picture 65). Obviously, if the flow is less turned, detachments and wakes are avoid or delayed and losses become less intense. Therefore the blade shape plays an important role in vorticity formation, increasing the flow acceleration and decreasing the flow blockage.

Figure 63: Flow behavior near leading edge on baseline and best individual.

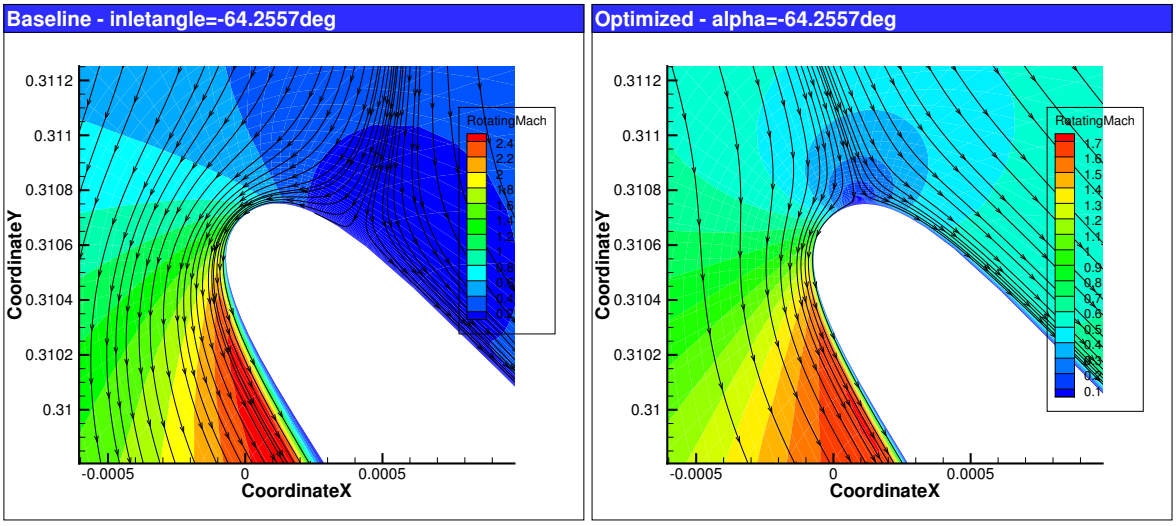

Furthermore, the isentropic Mach number trend over blade surface allows to omit the boundary layer influence and focus only on shocks result in order to make more clear how a precompression blade works and its importance in losses reduction. The optimized blade shape allows to decrease the passage inlet flow Mach number changing completely the shock type, reducing the normal shock width. What happen next in the passage, as shown in figure 66, is simply due to the upward translation

Figure 64: Wake and detached flow along pressure side on baseline and best individual.

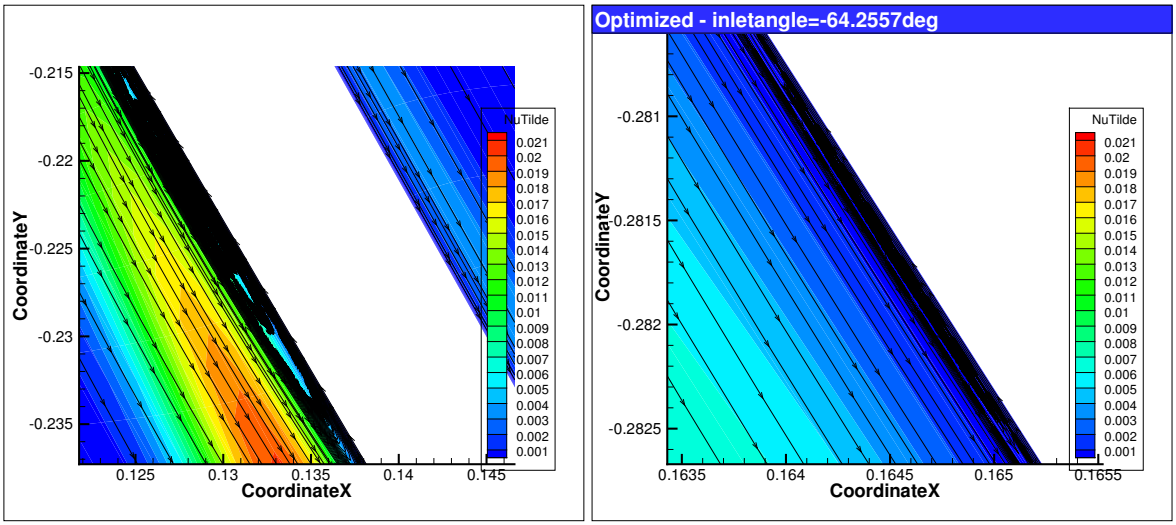

Figure 65: Flow behavior near trailing edge on baseline and best individual.

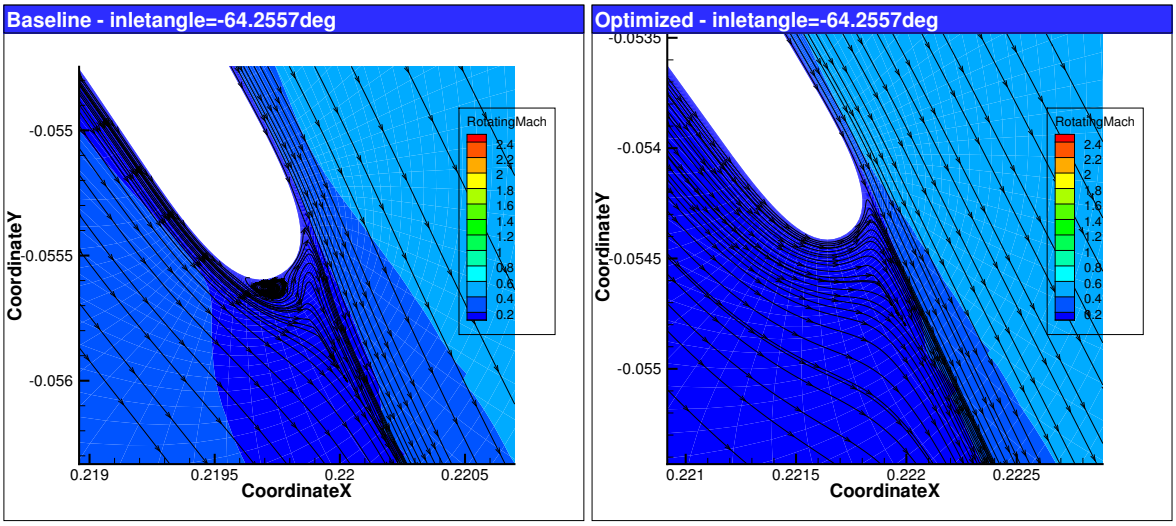

of the shock system, to the "generation" of a second wave at the end of the blade passage and to the normal "nature" of this last wave. For these reasons, the entire M_iso trend moves towards the trailing edge delaying the flow deceleration and, on suction side, the value at leading edge decrease. On the other hand, on best blade pressure side, the velocity increase due to the supersonic "pocket" at pressure side inlet; in particular, this speed increase, is due to the normal shock near the exit that alters the pressure pattern (see figure 59). This behavior is extremely important for the purpose of this work, i.e. decrease the compressor cascade losses and find a method for performance evaluation. Note that, both graphs show a steep reduction of M_{iso} on suction side, respectively at passage inlet and outlet; this means that, in both cases, a lambda-shape shock occurs.

Figure 66: Isentropic Mach number along baseline and best individual profile at $\alpha = -64.2557$.

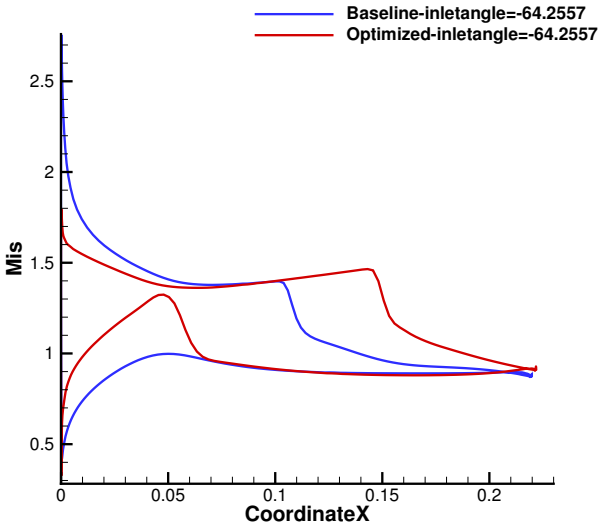

Finally, figure 67 shows the total pressure loss coefficient trend along a vertical line near the flow field outlet. First, note how the various sources of losses influence the ω trend: the slight decrease of the peak in the middle span of the passage (point 2 in figure 67) is due to the reduction of the shock system strength; on the other hand, the detached flow and in general the boundary layer make the ω rising along the blade surfaces (1). With this and ΔS trend in mind (see table 7), the sources of losses and the new blade shape role are more clear and tangible. It is important to remark that ω trend is the quicker and easier method to make clear how shock waves and boundary layer play a role in losses generation. Despite that, entropy increase is preferred as performance indicator.

Figure 67: Total pressure loss on baseline and best individual at $\alpha = -64.2557$.

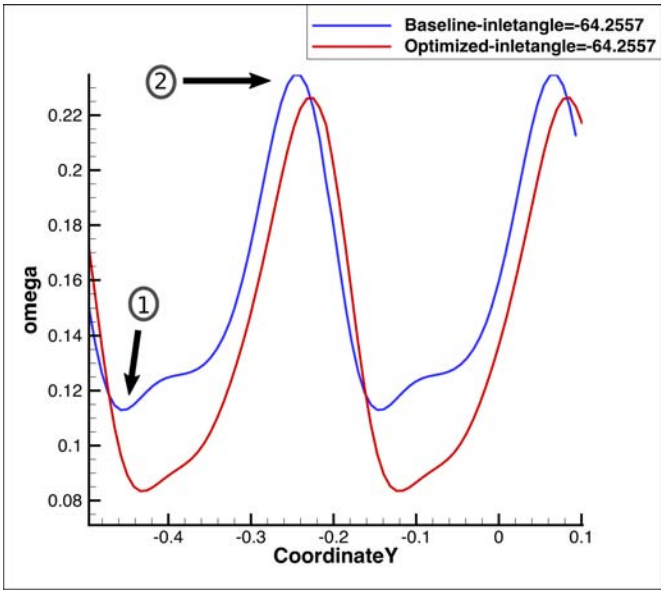

At the end of this section, it is important to remark that the previous analysis simply deals with a piece of a multi-objective optimization, not with a simple single-objective optimization; the difference between the two analysis will be clarified in the section just below.

Best blade flow behavior at different flow angles As discussed in chapter 5, imposing three different inlet flow angles leads to consider three function objectives for each individual. This means, unlike the previous case, the last optimized blade could be more performant for one angle, but worst for the remaining ones (see table 7).

Table 7: Static entropy coefficient change with angle

α [°]	ΔS [10^{-2}]								
	Baseline	Individual 1	Individual 2	Individual 3	Individual 4	Individual 5	Individual 6	Individual 7	Best individual
−63.2557	1.8970138	1.1127119	0.9373609	1.1104554	1.0326719	0.8902489	0.9766302	0.8697339	1.0101595
−64.2557	2.2428894	1.0975683	1.0103003	1.0907609	0.9992441	0.9879125	0.9943970	0.9786988	1.0084554
−65.2557	2.5314404	1.2747733	1.3993788	1.1913380	1.0786320	1.3883786	1.2364448	1.3684132	1.1568834

The optimum inlet flow angle is not a function of downstream condition but is set by the upstream shock; on the other hand, pressure (and obviously Mach number) distribution on profile, transition location and separation size are bound to inlet angle. That means, changing the flow incidence, the performance of the best individual at could become lower than the worse blade one[57]. In figure 68 the aforesaid *loss bucket* trend is shown: for each optimization, the ΔS minimum should be inside the chosen flow angle range (operative range). This minimum is the cascade optimum point, where the mass flow and the incidence allow safe and "performance" operation. Hence, for baseline and other individuals (the latter depicted by black symbols), the optimum conditions are not reached. For example, for individual 5, the optimum condition will be at less negative inlet angle, as shown comparing entropy trend in table 7 and in figure 68 (left triangle). Otherwise, the optimized design has its minimum between $\alpha = -63.2557°$ and $\alpha = -65.2557°$ allowing the flow to reach the metal angle around $\alpha = -64.2557°$; therefore the fluid follows the blade shape with low turning, separation and therefore low losses (nominal or design condition). Note that, having the flow turning constrain only on $\alpha = -64.2557°$, does not means that angle should be the metal angle[58] for every design. Therefore, in next optimizations, the incidence range could be extend to higher angles (i.e. less negative).

[57] e.g. compare last and second-last optimized blade ΔS at $\alpha = -64.2557$

[58] as afore said, the metal angle is the slope between the flow and the tangent to camberline. It could be different from the inlet flow angle

Figure 68: Loss variation with flow incidence

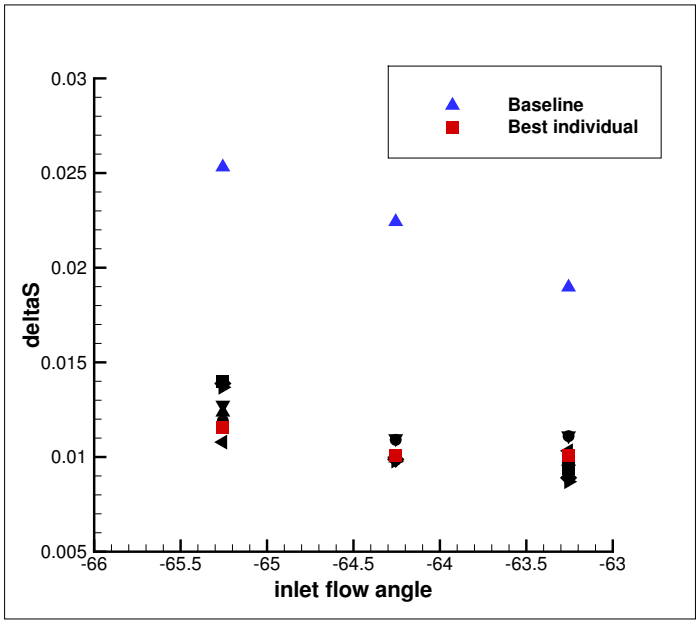

Moreover, as reports in chapter 4, with multiple objective the optimum design search for one objective is not "free" but bound to the remaining objectives, i.e. the best blade at α_2 could become the worst one when changing the angle. For these reasons, a 3D Pareto front becomes necessary to better understand the optimization process and objectives trend. As shown in figure 69, the Pareto front surface is made through interpolation of spare ΔS coordinates; moreover the points in that surface "belong" to the more fit individuals of the entire optimization while the best individual per each population lies in a local minimum. Finally, in the Pareto absolute minimum point lies the best design, i.e. here the best three ΔS compromise takes place. The remaining generated designs would stay above the Pareto front, that is why they are not plotted. Considering the different colors, the absolute minimum is located in the dark blue area, laying along the corresponding line in the ΔS_1,ΔS_2 plane. The best individual is the best compromise between the three ΔS values, i.e. decreasing one objective the others would increase and probably reach the ones that stand in a Pareto peak. For example, as you can see from isolines in figure 69, entropy coefficient values lower than 0.01 are reached for $\alpha = -63.2557°$ and $\alpha = -64.2557°$, while the ΔS_3 get its higher value[59]. Therefore, the best individual does not show the lowest performance coefficient for each inlet angle, but the lowest average ΔS, as is possible to see comparing the best individual and individual *3* in table 7.

[59] or better, its higher value for that area, i.e. the blue one

Figure 69: Pareto front

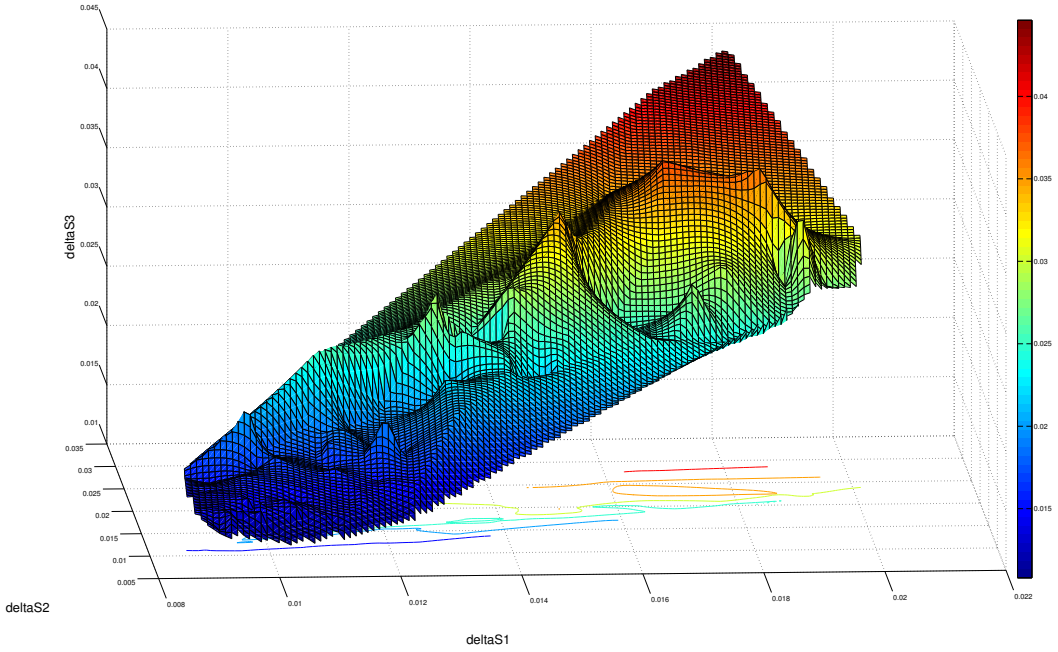

As the inlet flow angle changes, the remaining independent flow variables follow the trend shown in table 8; almost all the values remain constants, obviously due to inlet and outlet boundary conditions. The $AVDR$ behavior is the most unclear, since its increase should reduce losses (as reported in section 3.4). Probably, the slight increment must not be consider as a variation but as an numerical oscillation around a constant value. Therefore, the quasi-2D flow field and the flow turning requirement in optimizer setup helps to maintain the $AVDR$ equal to unity. However, the incidence increase, changes the flow behavior specially in front of the blade passage and inside it affecting losses value and shock pattern.

Table 8: Inlet flow independent variables on best individual at different flow angles

Best blade			
α [°]	-63.2557	-64.2557	-65.2557
M_1 [ ]	1.3	1.3	1.3
$AVDR$ [ ]	1.04344	1.06203	1.08122
p_2/p_1 [ ]	0.59759	0.59759	0.59759

In figure 70a, raising the inlet flow angle (i.e. from $-63.2557°$ to $-65.2557°$), the flow expands to higher pre-shock Mach numbers, i.e. in front of the leading edge along the suction side the velocity increase and the compression waves (B) becomes more distant from each other reducing their compression strength. In the meanwhile, the inlet shock becomes stronger, increasing the Mach stem width (named D in figure 70b) and the strength of the oblique shock (C) while downstream normal shock (G) moves upward reducing its size; moreover, the Mach number reduction between the two lambda leg is more severe. Hence, the supersonic region inside the passage will be limited to a small area within the second normal shock while the subsonic area expands until the first passage shock ($ACDE$), as depicted in figure 71a. The flow re-acceleration after the lambda-shape shock (E) becomes even more weak, reducing to a very small supersonic area just below the boundary layer. In conclusion, as the inlet angle increases, the flow behavior in the optimized blade passage becomes more similar to the baseline (in figure 59a), with high passage inlet Mach number, a quasi-normal

shock system and large pressure increase across the wave; obviously, the best individual losses is lower than baseline, even at $\alpha = -65.2557°$.
The total pressure distribution obviously follows the Mach number trend and shock wave pattern. Indeed, since at $\alpha = -63.2557°$ in the centre of the passage there are only oblique shocks, the p_0 in that area obviously remains the same. Otherwise, as the angle increases, the total pressure inside the passage decrease until a lower p_0 stream appears (see figure 71b). This trend is simply due to the increase in strength of the shocks.
Focusing on leading edge, figure 72a shows how, as incidence angle rises, the stagnation point moves slightly downward and suddenly upward, finally coming back to the first position. Furthermore, in the suction side, the flow turning (and so flow separation) decreases from $-63.2557°$ to $-64.2557°$, while it increases again at $\alpha = -65.2557°$. This behavior, due to metal angle achievement around $\alpha = -64.2557°$ (as shown in figure 68), do not prevents the flow to increase separation on suction side at $\alpha = -65.2557°$. In the opposite side, in the pressure side, at $-63.2557°$, the boundary layer separation is severe, due to the adverse pressure gradient near the normal shock; indeed, as it become smaller, that detachments almost disappears (see figure 70b).
The vorticity distribution shown in picture 72b, with angle raise, moves upward along the pressure side increasing its higher value streamwise after the trailing edge; as afore said, this behavior is due to the inlet Mach number trend and shock pattern. Likewise, the flow detachments is anticipated and becomes wider.
The isentropic Mach number follows the previous flow behavior: as α increases, on suction side, the flow decelerates earlier while on pressure side the supersonic "pocket" size decreases from 1.4 to 1.1. This behavior can be explained considering again the shock pattern in figure 70b: as the second passage shock becomes smaller and moves upward, the induced pressure gradient on pressure side is reduced as well as the peak in M_{iso} trend. On the suction side, the isentropic Mach number simply moves upstream, maintaining the typical shape due to the lambda-shape shock. Moreover, at $\alpha = -63.2557°$, the adverse pressure gradient influence even the suction side, causing a slight increase in M_{iso} values near the passage exit; as the normal shock (G in figure 70b) moves away from the suction side, this alteration disappears. Finally, despite the huge difference in pressure side M_{iso} values, the entropy coefficient does not change so much with angle increase; this is due to the suction side more severe role in loss generation, where the speed values remain almost the same.
Finally, the ω trend in figure 73b shows an increase in the minimum and maximum values; the latter is due to the increase of subsonic area after shocks, while detachments and flow deviation influence the higher difference between inlet and outlet total pressure. This increase in boundary layer loss can be seen even in the vorticity distribution in figure 72b and play an important role in reducing the blade performances at $\alpha = -65.2557°$.

Concluding, note that the analysis above is nothing more than an off-design analysis: the flow pattern at $\alpha = -64.2557°$ depicts the behavior of the best blade at almost nominal condition while for the remaining inlet angle the loss coefficient increases (see table 7 and figure 68). In addition, the whole flow behavior (i.e. the shock pattern and variables value) is well predicted by the situation reported in figure 36, where a β decrease corresponds to an increase of $|\alpha|$.

Figure 70: Mach number contour and shock pattern on best individual at different inlet flow angles

a) b)

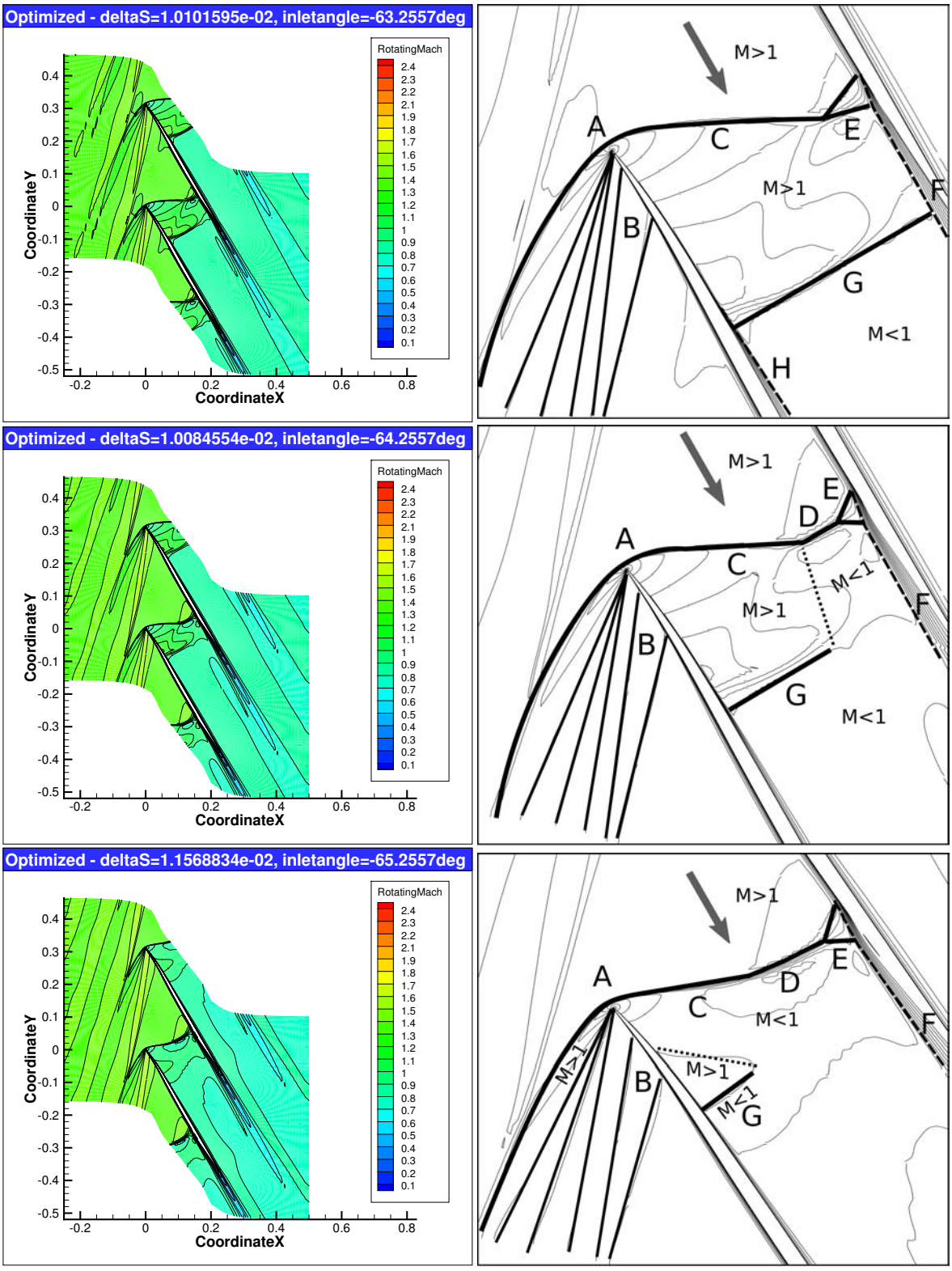

Figure 71: Mach areas and total pressure on best individual at different inlet flow angles

a) b)

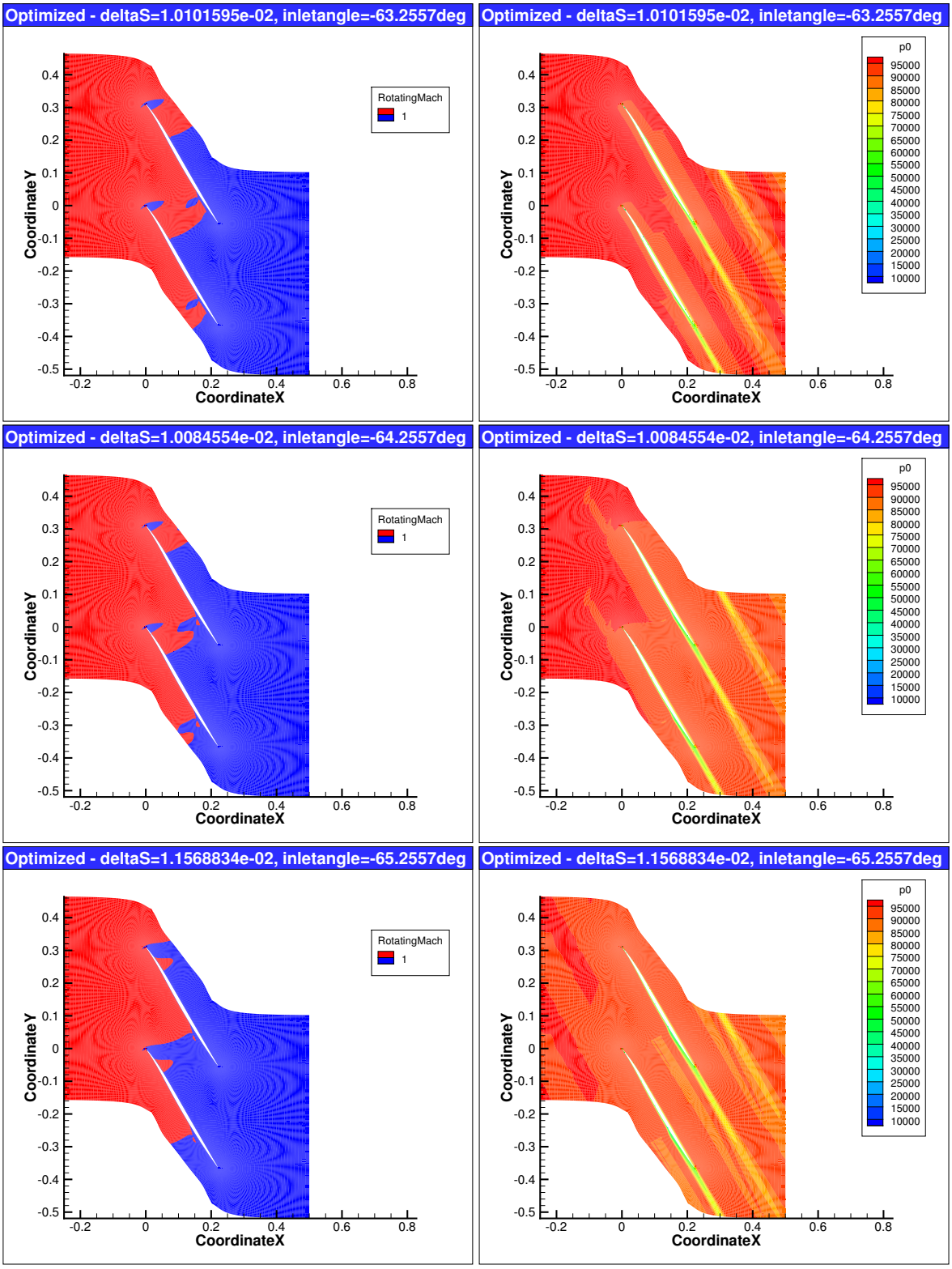

Figure 72: Streamlines and vorticity on best individual at different inlet flow angles

a) b)

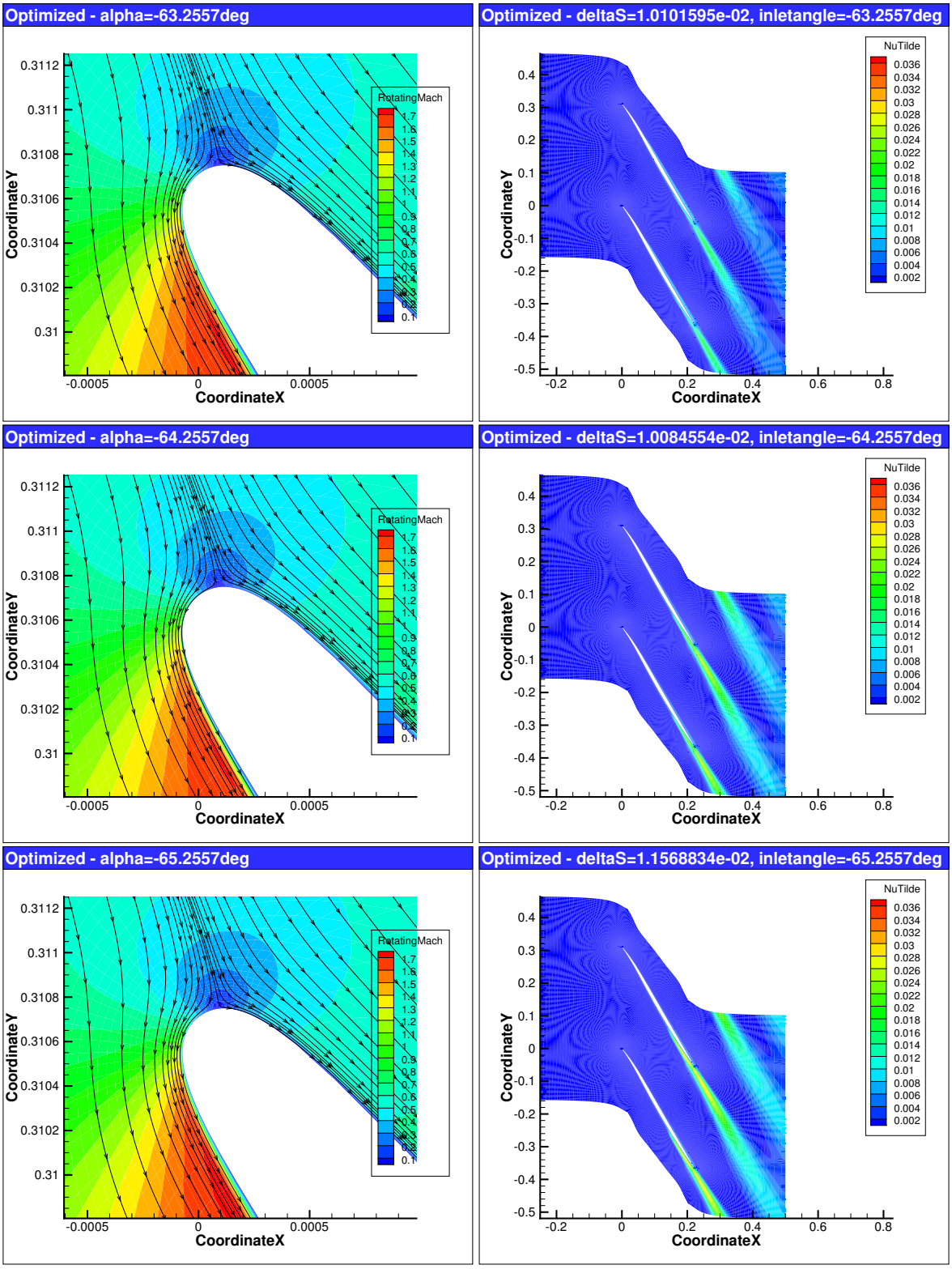

Figure 73: Isentropic Mach number and pressure loss coefficient on best individual at different inlet flow angles

a) b)

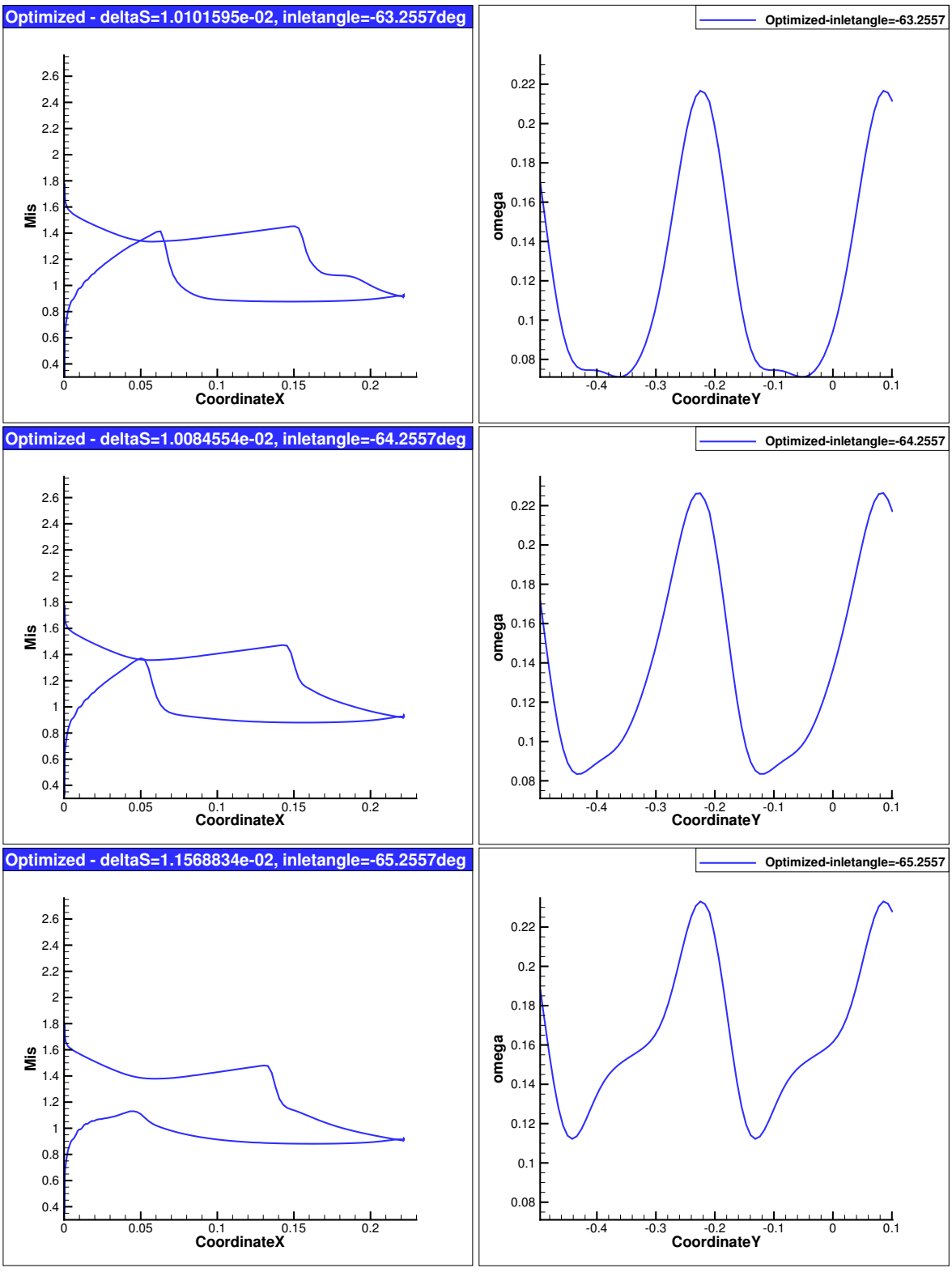

7 Conclusions

The whole work can be split in two parts, the first dealing with softwares and their setups, the second focused on numerical results and precompression blade.
Starting from the first feature, several conclusions can be made about the optimizer. First at all, the optimum search seems to follow the desired direction, reducing immediately the function objective (as can be seen in figure 57) and following the desired boundary condition. In the other hand, the optimizer, dealing with multi-objective optimization, proves to be able to avoid severals local minima (as shown in figure 69), select individuals with the best compromise between their function objectives and modify properly the blade geometry. This simply means that $CADO$ was set accurately, choosing the right parameters (i.e. mutation and crossover constant as well as the population size and iterations/generations number) and starting from feasible initial individuals. Moreover, the blade parametrization with constant thickness and variable camberline distribution seems to be sufficient to describe properly the blade airfoil without strange or unfeasible shapes. However, the given β range should be re-arranged since the best blade β_5 value reaches the imposed lower limit; this could prevent the camberline to assume a "more performant" shape. Finally, the flow turning constraint on only one performance parameters do not prevent the optimizer to improve performances for all inlet flow angles; indeed, the not-constrained flow turning are bound to the constrained one. Considering the flow field depicted in figure 51, the 2D model, with its 6 "subregions" and the related boundary conditions, well fits the flow behavior inside the cascade. As regards the mesh, the chosen setup follows the blade shape properly with low distortion of the field and a good discretization of the blade boundary layer. Probably, the grid points number can be reduced, manually decreasing size and number of cells near cascade inlet and outlet and maintaining unchanged the remaining elements; this can help to reduce the computational time and the size of the CFD outputs. About the latter, the chosen numerical model seems to follow the prediction based on experimental and theoretical data; in particular the CFD results match perfectly with the shock pattern experienced by the authors in [20],[10] and [8] as well as the loss parameter trend follows the theoretical models (see chapters 2.3 and 3). This achievement is due to the chosen CFD flow model (turbulent with the reference values reported in 5.4), the Spalart-Allmaras turbulence model, boundary conditions, discretization type and parameters and to the robust iterations. In particular, without the latter, the solution blew up after 1000 iteration causing the solver to stop. Hence, after 600 robust iteration, the further 5000 outer iterations always allows the solver to reach or approach the convergence criteria. In conclusion, the chosen softwares and their setup guarantee an automatic, self-sustaining loop and loop. The big drawbacks of this configuration is the high computational time (about one week for 460 individuals) and output size (more than $10Gb$ for a 8 population optimization); reducing the grid points, using adjoint solver, choosing DOE method for the initial database generation and not validating each design with the high fidelity tools can help to solve that problem.
In compressors design the main requirement is to reach the highest back pressure p_2 possible with a minimum increase in losses. For this reason, following the theoretical and experimental prediction reported in chapters 2.3 and 3, the following guidelines can help to develop a compressor cascade with low losses and high performance:

- flow detachments and the related streamtube contraction should be avoided;
- at the same time, turbulent transition inside the boundary layer can be promoting to avoid its separation;
- weak and multiple shock waves growth can be encourage to increase pressure gradient without flow blockage, undue velocity diffusion and high flow turning;
- velocity diffusion and boundary layer thickness should be reduced firstly on suction side, while on pressure side they can be tolerate;
- flow incidence should be negative in order to decrease flow speed along the blade suction side;
- far from nominal flow condition, safe operations are guaranteed maintaining constant the mass flow, i.e. avoiding flow blockage;
- when the flow is chocked, the back pressure can be increase without affecting the upstream flow. Moreover, in this condition, the inlet flow angle and inlet Mach number are not even more independent parameters.

All the above listed requirements can be satisfied simply reducing the pre-shock Mach number while delaying the supersonic-to-subsonic transition of the flow. A precompression blade, with its concave suction side near leading edge, develops a compression fan able to decrease the velocity at the cascade inlet; furthermore, sharp leading edge reduces the bow shock detachment (typical in over-expanded flow) decreasing its strength and causing a second shock inside the passage near trailing edge. In addition, at suction side, the interaction between the boundary layer and the left running branch of the bow shock generates the peculiar lambda-shape shock; that wave further reduces the flow velocity thanks to two close oblique shocks, as depicted in figure 59. This shock pattern allows to decrease shock and boundary layer losses, hence achieving a large loss reduction. In off-design condition, with a raising but always negative inlet flow angle, the shock pattern changes, maintaining its typical shape (two shocks with a lambda-shape wave on suction side) and avoiding the higher loss increase achieved with an ordinary blade. Note that, as depicted in figure 55, this positive influence increases as the blade camberline assumed a more curved shape at leading and trailing edge (i.e. respectively increasing and decreasing the camberline slope with respect to the baseline).
In summary, becomes important to emphasize that the numerical results completely follows the predicted and required flow behavior. This validates the softwares "chain" and setup, while, in second instance, suggests that precompression blades play an important role in loss reduction; indeed, its s-shaped camberline and thin leading edge allows to avoid or soften the principal loss sources maximizing the pressure ratio even in off-design conditions.

8 Future work

At the end of this work, several improvements can be suggested for further optimization campaigns. First at all, the $|\beta_5|$ range in blade parametrization should be decrease (see table 1) in order to allow the optimizer to generate a feasible more performant individual with a lower $|\beta_5|$. Remaining in the optimizer setup, in order to speed up the optimum search, an initial sampling of the database should be perform through the DOE method; furthermore, not validating each design with the high fidelity tools can help to reduce the computational time. In the other hand, the grid points number can be further reduced, manually increasing size and so decreasing the number of cells near cascade inlet and outlet and maintaining unchanged the remaining elements; thereby, computational cost and size of the CFD outputs will be reduced, ensuring a fair flow description near boundary layer detachments and shocks. Moreover, in CFD setup, an adjoint solution type can help to increase the reliability of results. At the end, since the best blade optimum angle was found (from figure 68, $\beta = -64.2557$), a CFD simulation at unique incidence condition could be done testing the best blade performances at different inlet Mach number.

References

[1] S. L. Dixon, C.A. Hall, *Fluid Mechanics and Termodynamics of Turbomachinery*, Seventh edition, Butterworth - Heinemann

[2] E. Benini, *Propulsione Aerea*, Cleup, Padova, 2006

[3] J. D. Denton, *Loss Mechanisms in Turbomachines*, ASME Journal of Turbomachinery, Vol. 115, October 1993, 621-656

[4] T. Verstraete, *Introduction to Optimization and Multidisciplinary Design*, Lecture Series 2014 - 04, The Von Karman Institute of Fluid Dynamics, Belgium

[5] T. Verstraete, *Multidisciplinary Optimization of Turbomachinery Component using Differential Evolution*, Lecture Series 2010 - 07, The Von Karman Institute of Fluid Dynamics, Belgium

[6] R. Storn, K. Price, *Differential Evolution - A Simple and Efficient Heuristic for Global Optimization over Continous Spaces*, Journal of Global Optimization, Vol. 11, 1997, 341-359

[7] M. M. Rai, *Single- and Multiple-Objective Optimization with Differential Evolution and Neuronal Networks*, Introduction to Optimization Methods and Multidisciplinary Design in Aeronautics and Turbomachinery, June 2-6, 2008, NASA Ames Research Center, Moffett Filed, USA,

[8] E. Benini, A. Toffolo, *Development of High - Performance Airfoils for Axial Flow Compressors Using Evolutionary Computation*, AIAA Journal of Propulsion and Power, Vol. 18 No. 3, May–June 2002

[9] J. D. Anderson Jr., *Foundamentals of Aerodynamics*, Fifth edition, McGraw-Hill Book Company, New York, 2011

[10] H. A. Schreiber, H. Starken, *An Investigation of a Strong Shock-Wave Turbulent Boundary Layer Interaction in a Supersonic Compressor Cascade*, ASME Journal of Turbomachinery, Vol. 114, July 1992, 494-503

[11] M. Piotrowiz, P. Flaszyni, P. Doerffer, *Investigation on Shock Wave Boundary Layer Interaction on Suction Side of Compressor Profile*, Journal of Physics: Conference Series 530, 2014

[12] S. G. Kempf, *Numerical Study of the Stability of Embedded Supersonic Compressors Stages*, Virginia Polytechnic Institute and State University, 2003

[13] W.M. Konig, D.K. Henneke, L. Fottner, *Improved Blade Profile Loss and Deviation Angle Models for Advanced Transonic Compressor Bladings: Part II - A Model for Supersonic Flow*, ASME Journal of Turbomachinery, Vol. 117, January 1996, 81-87

[14] E. W. Renauld, *Secondary Flow, Total Pressure Loss and the Effect of Circumferential Disctortion in Axial Turbine Cascades*, Massachusetts Institute of Technology, February 1991

[15] L. E. Brown, *Axial Flow Compressor and Turbine Loss Coefficients: a Comparison of Several Parameters*, ASME Journal of Engineering and Power, Vol. 94, July 1972, 193-201

[16] A. Cavallini, M. Sovrano, S. Mancin, L. Rossetto, *Elementi di Gasdinamica*, Edizioni Progetto Padova, 2012

[17] J. D. Anderson Jr, *Modern Compressible Flow: With Historical Perspective*, Second Edition, McGraw-Hill Book Company, New York, 1990

[18] G. Ben Gabi, *Shock Wave Reflection Phenomena*, Second Edition, Springer-Verlag, Berlin Heidelberg, 2007

[19] C. A. Hunter, *Experimental, Theoretical, and Computational Investigation of Separated Nozzle Flows*, AIAA Journal of Propulsion and Power, Vol. 20 No. 3, May-June 2004, 527-532

[20] D. L. Tweedt, H. A. Schreiber, H. Starker, *Experimental Investigation of the Performance of a Supersonic Compressor Cascade*, ASME Journal of Turbomachinery, Vol. 110 No. 4, October 1988, 456-466

[21] T. Verstraete, *CADO: a Computer Aided Design and Optimization Tool for Turbomachinery Applications*, 2^{nd} International Conference on Engineering Optimization, Lisbon, Portugal, September 6-9, 2010